Development of a silicon detector system for proton detection and triple coincidence measurements in electron scattering on 12C nuclei

Makek, Mihael

University of Zagreb
Faculty of Science
Physics Department

Mihael Makek

Development of a Silicon Detector System for Proton Detection and Triple Coincidence Measurements in Electron Scattering on ^{12}C Nuclei

Dissertation

Zagreb, 2009.

University of Zagreb
Faculty of Science
Physics Department

Mihael Makek

Development of a Silicon Detector System for Proton Detection and Triple Coincidence Measurements in Electron Scattering on ^{12}C Nuclei

Dissertation
submitted to the Physics Department,
Faculty of Science, University of Zagreb
for the academic degree of
Doctor of Natural Sciences (Physics)

Zagreb, 2009.

Contents

Chapter 1

Introduction and Theory

1.1 Motivation

Electron scattering on nuclei can be a great tool for studying hadron properties and nucleon-nucleon (NN) correlations in nuclear matter. Both can be investigated in triple-coincidence exclusive reactions, such as $A(e, e'p\pi^-)B$ for the former case of Δ-resonance in nuclear medium or $A(e, e'pp)B$ and $A(e, e'pn)B$ reactions for the investigation NN-correlations.

The continuous beam electron accelerator at MAMI [1, 2] and the magnetic spectrometers of A1 collaboration [3] are outstanding facilities for performing such measurements. The main obstacle for the triple-coincidence reactions though, is relative slow data collection due to the nature of these reactions and the small solid angles subtended by the magnetic spectrometers. Longer measurements could be performed in order to gain sufficient statistics, but this is very costly and staff-demanding.

We have chosen a different approach: to enlarge the total angular acceptance of the detectors. This has been achieved by development of a silicon detector system, which has an angular acceptance up to three times larger than the magnetic spectrometers. The Silicon Detector[1] has been successfully tested and used for detection of low energy protons in double and triple coincidence measurements.

The remainder of this chapter gives a theoretical introduction to the experiments performed with the Silicon Detector. The second chapter shortly describes the experimental facility. The Silicon Detector that was developed in the framework of this thesis is described separately in chapter three and appendix A. Data analysis and the experimental results are laid out in chapters four and five, respectively. Appendix B describes the algorithms developed for digital processing of Silicon Detector signals.

[1] The term *Silicon Detector* is used interchangeably with the *silicon detector system*.

1.2 Short-range correlations

The independent particle shell model (IPM) developed in 1950s, is one of the most successful models for describing nuclei. It assumes existence of a mean field generated by the mutual attraction of all nucleons inside a nucleus. In that model the nucleons move independently in well defined orbits (shells) created by the mean field. The IPM successfully describes nuclear structure if effective NN-interactions are used, but it fails to reproduce basic nuclear properties, such as binding energy, if more realistic models containing fundamental NN-interactions, are considered.

Indirect evidence for correlated behavior beyond the mean field description of the nucleus was found in experiments of proton knock-out on $A > 4$ closed-shell nuclei (e.g. [4–6]). They found that the spectroscopic strength for the proton removal has an average of 65% of the value predicted by the independent particle model and that the spectroscopic strength of the orbitals above the Fermi level[2] was non-zero. Several theoretical models [7–15] have shown that this could be a consequence of a strong short-range repulsive interaction of the nucleon pairs. According to these models, such interaction generates large nucleon momenta and promotes the correlated nucleons into the states above the Fermi level. Consequently, their momentum distributions acquire a tail extending to very high momenta.

Any fundamental approach to understanding a nucleus starts from the basic NN-interaction. Modern parametrizations of the NN-interaction (e.g. Argonne [16], Bonn [17], CD-Bonn [18], Nijmegen [19]) contain components depending on distance, spin and isospin of the nucleons. At short internucleonic distances the interaction is central and repulsive and it prevents the nucleus from collapsing. Nucleons in the ground state can form pairs with a large relative and small center-of-mass momentum due to these short-range components of the NN-interaction. Such short range correlated (SRC) pair interaction is necessary to reproduce NN-scattering data.

Beside the short-range correlations, the second type of NN-correlations are the tensor correlations (TC), which are due to the strong tensor component of the NN-interaction. They depend on spatial orientation and spin of the nucleons [7, 20] and are of intermediate range character. While the SRC are of particular relevance for pp-pairs, TC significantly contribute only in pn-pairs. There are also long-range correlations (LRC), which are mainly due to interactions of the nucleons on nuclear surface.

[2]Fermi level is the energy of the highest occupied nucleon state, according to nuclear shell model.

1.2.1 Study of SRC in NN-knockout reactions

While the proton knock-out reactions provided indirect evidence for the correlated behavior, two-nucleon knockout reactions offer a possibility to observe the SRC more directly. Two-nucleon knockout can be induced electromagnetically, either by a real or a virtual photon[3] [21–24]. If one of the paired nucleons is knocked-out (one-body process), the remaining nucleus will probably be left in a highly excited state with a relatively large momentum. Consequently the other nucleon from the pair will be emitted. Thus by detecting two nucleons in an exclusive reaction the information about the short-range component of the NN-force can be obtained.

There are competing (two-body) processes like isobar currents (IC) and meson exchange currents (MEC), that also lead to knockout of two nucleons. Final state interaction (FSI) also mask the initial correlations, as they contribute to the reaction cross-section. However, the contributions to the cross-section of these additional processes strongly depend on the selected reaction channel. Therefore, a study all possible channels (γ, pp), (γ, pn), $(e, e'pp)$ and $(e, e'pn)$ is important for disentangling them from SRC. Only by comparing the experimentally obtained cross sections with theoretical predictions that take into account all the competing processes (NN-correlations, MEC, IC and FSI), can one draw conclusions about particular contribution to the nucleon-nucleon interaction.

Electron scattering experiments, where virtual photons are produced, are advantageous over experiments with real photons for a direct study of NN-correlations. This is because the real photons are sensitive only to transverse components of the interaction, while the virtual photons are sensitive to the longitudinal component as well[4]. The longitudinal cross section of an electron scattering reaction is believed to be dominated by one-body currents, so it is more important for SRC investigation [20]. By kinematically maximizing the longitudinal polarization of the virtual photon (equation 1.6), the sensitivity of an experiment to SRC can be increased. On the other hand, photoreactions are better suited to explore two-body currents. This is essential if we want to distinguish two-body-current effects from NN-correlations [25].

Of the electroinduced NN-knockout reactions, the pn-knockout is expected to give an order of magnitude larger cross-sections due to the tensor force that is active between neutron-proton pairs, but not between proton-

[3]Real photons have a fixed relation between the momentum and the energy $p_\gamma = E_\gamma/c$, i.e. they lay on the mass shell having $m_\gamma = 0$. In the case of virtual photons, the momentum and energy transfer can be independently varied within the space-like region.

[4]A real photon has only transverse polarization, while the virtual photon is also longitudinally polarized.

proton pairs [11, 26]. SRC play only a minor role in the pn-interaction compared to TCs, but are more important in pp-interaction. On the other hand, the advantage of pp over pn-knockout is that the MEC are forbidden (to the first order) by isospin selection rules, because the virtual photon cannot couple to the neutral pion exchanged between two protons. Therefore, the contribution of the MEC processes to the pp-knockout cross-section is believed to be negligible.

NN-knockout mechanisms

In reactions of electron scattering off nuclear targets different mechanisms can lead to knockout of two nucleons [24]. While they can be distinguished theoretically, in an experiment they can all contribute to the measured cross-section masking the mechanism we are interested in. To investigate NN-correlations we want the virtual photon to interact via one-body hadron current. This is depicted in figure 1.1 (a) where the virtual photon is absorbed by one nucleon that is a member of a strongly correlated pair. Due to this correlation, both of the nucleons are subsequently knocked out of the nucleus.

Meson exchange currents transmit the strong force between nucleons. In that approach the mass of the exchanged meson varies with the internucleonic distance. At relatively long NN-separations (1-1.5 fm) the MEC include pion exchange, at intermediate distances (0.5-1 fm) the exchanged meson is a sigma meson and at shorter distances heavier mesons play a role. The isobar currents (IC) also include meson exchange, but in this case one of the nucleons is excited into a baryon resonance, most commonly $\Delta(1232)$ which subsequently decays into a pion and a nucleon. The contribution of the IC to the NN-interaction is rather small in the ground state, as the nucleons need energy to be excited into a resonance and the probability of a spontaneous Δ-excitation is small. However, the IC become more important as the nucleus acquires energy (e.g. by absorption of a photon) and Δ-excitation becomes more probable.

Figures 1.1 (b) and (c) show MEC processes, where the virtual photon is absorbed by a pion exchanged between two nucleons, or a pion is exchanged after the virtual photon had been absorbed on a nucleon. The MEC contribute only in pn-knockout, while they are suppressed by isospin selection rules in two-proton knockout reactions.

Figures 1.1 (d) and (e) represent isobar current terms involving Δ - resonance excitation or deexcitation. The contribution of the IC exists in both pn and pp knockout and it grows as the energy transfer gets closer to the Δ-resonance region. However, spin-isospin selection rules largely suppress Δ-deexcitation in $pp \rightarrow \Delta p \rightarrow pp$ channel [27, 28], if the protons are

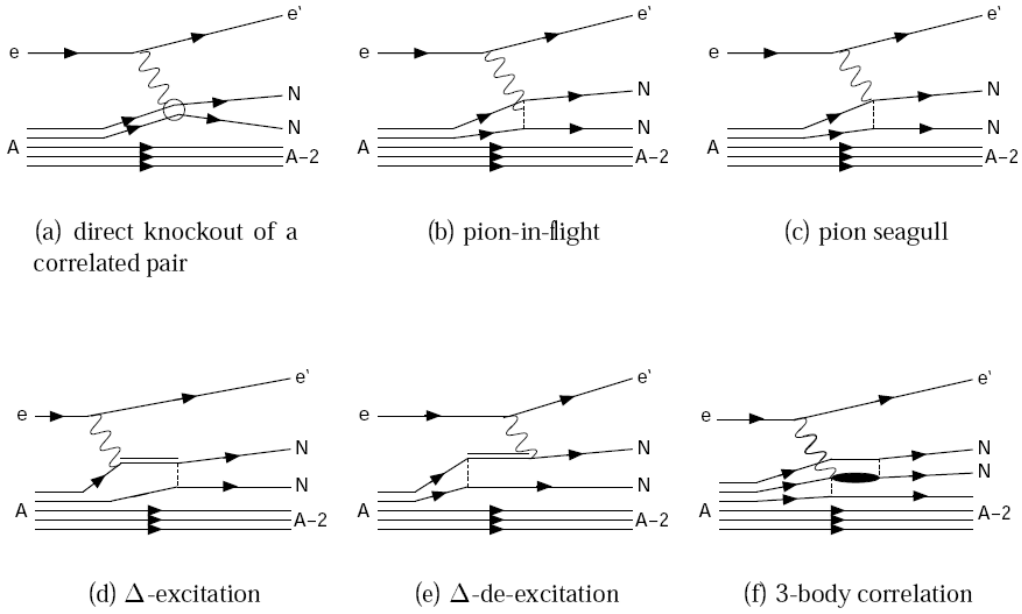

Figure 1.1: Possible mechanisms of knockout of two nucleons. Illustration from [29].

initially in ${}^1S_0$-state (see section 1.2.3).

Another possible mechanism is shown in the figure 1.1 (f) where the virtual photon couples to three interacting nucleons, but the relative strength of such a process is expected to be small [24].

Final-state interaction

The final state interactions (FSI) can also mask the initial correlation inside the nucleus. Some of the first theoretical treatments of FSI were taking into account only interaction between the ejected nucleons and the remaining A-2 nucleus. It has been shown that the interaction between the ejected nucleons themselves (NN-FSI) has also a large effect on a reaction cross-section [30]. The calculations show that this effect is more important in pp-emission, than in np-emission and it is generally larger in electroinduced than in photoinduced reactions. Even when two protons are emitted back-to-back, NN-FSI can increase the cross-section nearly by an order of magnitude [31, 32]. One example of such calculation for ${}^{16}O(e, e'pp)$ reaction, for the transition to the ${}^{14}C$ ground state (GS) in shown in figure 1.2.

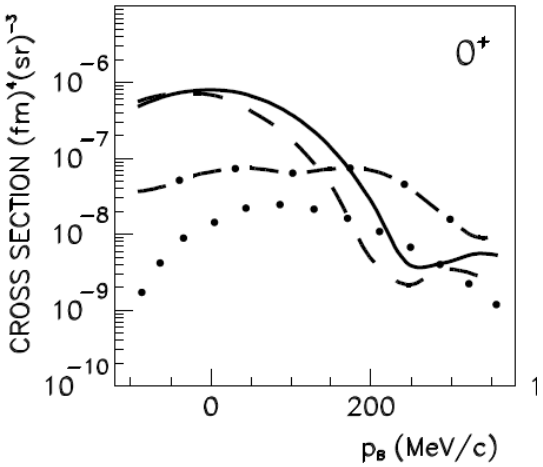

Figure 1.2: The differential cross-section of the $^{16}O(e,e'pp)^{14}C\,(GS)$ reaction in super-parallel kinematics with $\omega = 215$ MeV and $|\vec{q}| = 316$ MeV/c. p_B is the momentum of the recoiling nucleus. The dotted line represents calculation with IC and FSI contributions, the dash-dotted with IC and FSI-NN, the dashed with SRC and FSI and the solid line includes SRC and FSI-NN contributions. From [31].

1.2.2 (e,e'NN) reactions at MAMI

Kinematical definitions

In an electron scattering experiment at MAMI, the electrons with an energy E_0 interact with a fixed target of a mass M_A. Four-momenta of the incoming and the scattered electron are[5]:

$$e:\ p_e = (E_0, \vec{p}_e) \tag{1.1}$$
$$e':\ p_{e'} = (E_{e'}, \vec{p}_{e'}) \tag{1.2}$$

The virtual photon four-momentum is given by:

$$q = (\omega, \vec{q}) = (E_0 - E_{e'}, \vec{p}_e - \vec{p}_{e'}) \tag{1.3}$$

and the negative four-momentum-squared:

$$Q^2 = \vec{q}^{\,2} - \omega^2 = 4E_0E_{e'}\sin^2\frac{\theta_e}{2} \tag{1.4}$$

[5]Relativistic four-vector notation with "natural units" $c = \hbar = 1$ is used.

The transverse and the longitudinal polarization of the virtual are defined as:

$$\epsilon = \left(1 - \frac{2\vec{q}^2}{q^2}\tan^2\frac{\theta_e}{2}\right)^{-1} \tag{1.5}$$

$$\epsilon_L = -\frac{q^2}{\vec{q}^2}\epsilon \tag{1.6}$$

The equations (1.3)-(1.6) show that the energy transfer, momentum transfer and the polarization of the virtual photon depend purely on the angle θ_e and the energy $E_{e'}$ of the scattered electron. By positioning the electron spectrometer (see section 2.2) at certain angle and central momentum one can obtain virtual photons of desired properties. The momentum transfer determines the "spatial resolution" of the experiment, i.e. the higher the momentum transfer, smaller the structures that can be resolved. The energy transfer generally determines how much energy will be left to the particles in the final state. The polarization of the virtual photon gives access to the transverse or longitudinal components of nuclear response.

The differential cross-section of an exclusive (e,e'NN) reaction is described in a spherical coordinate system with the polar-axis pointing in the direction of the momentum transfer $\vec{q}$, as depicted in the figure 1.3. The scattering plane is defined by momenta of the incoming and the scattered electron, while the reaction planes are spanned by the momentum of each outgoing nucleon and the momentum transfer vector. The four-momenta of the outgoing nucleons in spherical coordinates are:

$$p_1 = (E_1, \vec{p}_1), \quad \vec{p}_1 = (|\vec{p}_1|, \gamma_1, \alpha_1) \tag{1.7}$$

$$p_2 = (E_1, \vec{p}_2), \quad \vec{p}_2 = (|\vec{p}_2|, \gamma_2, \alpha_2) \tag{1.8}$$

where γ are polar angles and α azimuthal angles defined relative to the scattering plane. The angle between the two reaction planes is defined as $\phi = \alpha_1 - \alpha_2 + \pi$, while γ_{12} is the angle between $\vec{p}_1$ and $\vec{p}_2$.

The target nucleus is initially at rest, so its four-momentum is:

$$p_A = (M_A, 0) \tag{1.9}$$

The undetected energy and momentum, commonly denoted as the "missing" particle with $(E_m, \vec{p}_m)$, are determined by energy and momentum conservation:

$$E_m = M_A + \omega - E_1 - E_2 \tag{1.10}$$

$$\vec{p}_m = \vec{q} - \vec{p}_1 - \vec{p}_2 \tag{1.11}$$

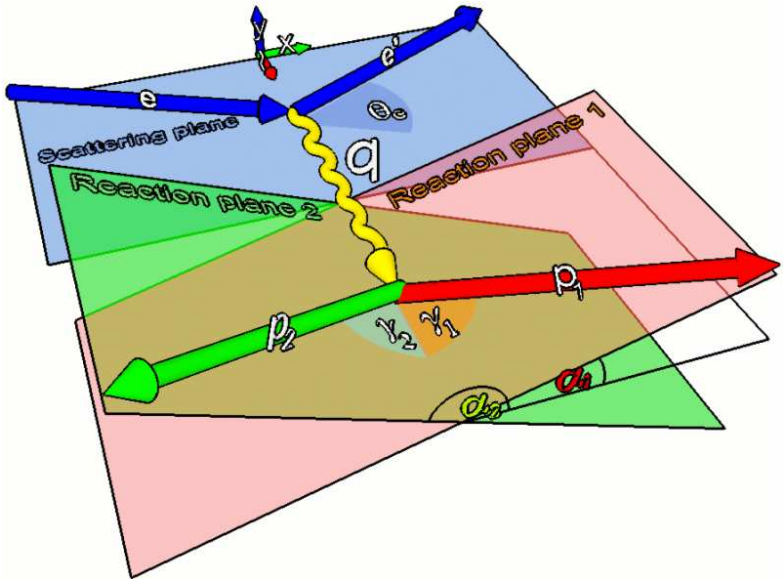

Figure 1.3: Schematic drawing of a (e,e'NN) reaction kinematics.

The missing momentum is then equal to the momentum of the A-2 nucleus, but the missing energy takes into account the energy of the A-2 nucleus, as well as the possible excitation energy. This is best observed by defining the missing mass:

$$m_m = \sqrt{E_m^2 - \vec{p}_m^2} \tag{1.12}$$

so the excitation energy E_x of the A-2 nucleus can be expressed as:

$$E_x = m_m - M_{A-2} \tag{1.13}$$

Differential cross-section

In one-photon-exchange (OPE) approximation and neglecting the influence of the nuclear Coulomb field on the incident and the outgoing electron, we can express the differential cross section as contraction of the leptonic tensor $L_{\mu\nu}$, which describes the scattered electron, with the hadronic tensor $W_{\mu\nu}$ which describes the interaction of the virtual photon with the nucleus [8,24]. We obtain a nine-fold differential cross-section[6]:

$$\frac{d^9\sigma}{d\vec{p}_{e'}d\vec{p}_1\vec{p}_2} = \alpha^2 \frac{1}{q^2\vec{p}_e\vec{p}_{e'}(\epsilon - 1)} L_{\mu\nu}W^{\mu\nu} \tag{1.14}$$

[6]The four particles in the final state have 16 degrees of freedom, four of which are fixed by conservation laws and three by the known mass of the three observed particles. This gives the nine-foldedness of the cross-section ($16 - 4 - 3 = 9$).

where α is the fine structure constant. The tensor contraction yields a linear combination of six independent structure functions $f_{\lambda\lambda'}$ [8]:

$$\begin{aligned} L_{\mu\nu}W^{\mu\nu} &= 2\epsilon_L f_{00} + f_{11} \\ &+ \sqrt{\epsilon_L(1+\epsilon)}(f_{01}\cos\alpha_1 + \overline{f}_{01}\sin\alpha_1) \\ &- \epsilon(f_{1-1}\cos 2\alpha_1 + \overline{f}_{1-1}\sin 2\alpha_1) \end{aligned} \tag{1.15}$$

with α_1 being the the angle between the scattering plane and the reaction plane of the first nucleon (see figure 1.3) and ϵ and ϵ_L are transverse and longitudinal polarization of the virtual photon respectively. The structure functions $f_{\lambda\lambda'}$ represent the nuclear response to the longitudinal ($\lambda = 0$) and transverse ($\lambda = \pm 1$) components of the electromagnetic interaction. They depend only on ω, $|\vec{q}|$, $|\vec{p}_1|$, $|\vec{p}_2|$ and on the angles γ_1, γ_2 and γ_{12} [8, 9], which are all determinable in an exclusive measurement.

The cross section for the transition to a definite final state of the outgoing nucleus is obtained by integrating the equation 1.14 over the energy of one of the outgoing nucleons [9,20]. (The electron mass is neglected in the following equations.) We obtain the eight-fold differential cross-section[7]:

$$\frac{d^8\sigma}{dE_{e'}d\Omega_{e'}dE_1d\Omega_1d\Omega_2} = \frac{\pi e^2}{2|\vec{q}|}\Gamma_V\Omega_f f_R L_{\mu\nu}W^{\mu\nu} \tag{1.16}$$

where $\Omega_f = |\vec{p}_1|E_1|\vec{p}_2|E_2$ is the phase-space factor, $\Gamma_V = \frac{e^2}{8\pi^3}\frac{E_{e'}}{E_0}\frac{|\vec{q}|}{q^2}\frac{1}{\epsilon-1}$ is the virtual photon flux and the f_R is the recoil factor given by:

$$f_R = 1 + \frac{E_2}{E_B}\left(1 - \frac{|\vec{q}|}{|\vec{p}_2|}\cos\gamma_2 + \frac{|\vec{p}_1|}{|\vec{p}_2|}\cos\gamma_{12}\right) \tag{1.17}$$

In this case E_2 is fixed due to conservation laws and E_B is the total energy of the recoiling nucleus.

1.2.3 ^{12}C(e,e'pp)^{10}Be in super-parallel kinematics

We have chosen to perform an exclusive $^{12}C(e,e'pp)^{10}Be$ measurement at MAMI in order to study the effect of the SRC on the reaction cross-section. Following the discussion throughout this chapter, the general properties of the chosen reaction are:

- Only SRC contribute to the cross-section, as TC are active only between pn-pairs.
- MEC are suppressed to the first order due to isospin selection rules.

[7]The integration over a finite energy range can be seen as fixing the mass of the A-2 nucleus, which removes one degree of freedom giving the eight-fold cross-section.

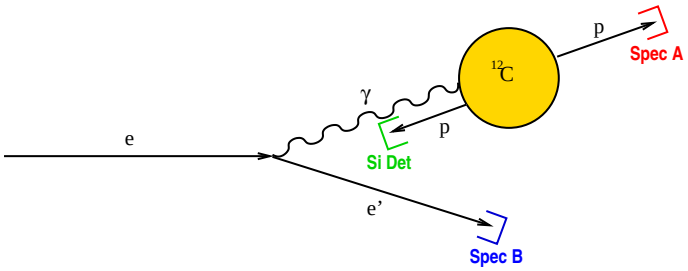

ω	163 MeV
q	198 MeV/c
θ_q	27.2°
ϵ_L	0.29
θ_{p1}	28°
θ_{p2}	153°

Figure 1.4: Schematic drawing of the super-parallel kinematics chosen for $^{12}C(e,e'pp)^{10}Be$ reaction.

Kinematics

The measurement was made in super-parallel kinematics, in which one proton was detected parallel and the other anti-parallel to the momentum transfer, as depicted in figure 1.4. According to the figure 1.3 this means that $\alpha = 0$, $\gamma_1 = 0$ and $\gamma_2 = \pi$, which results in vanishing of all the structure functions from equation 1.15, except the purely longitudinal part (f_{00}) and purely transverse part (f_{11}) [8, 26]. Hence there is a possibility to completely separate these structure function via Rosenbluth plot. Previous measurements of $^{12}C(e,e'pp)^{10}Be$ in close to 4π-geometry [33] show that proton-proton angular correlation is the strongest in super-parallel kinematics (figure 1.5), which additionally supports this particular choice of kinematics.

In super-parallel kinematics, the contribution of the isobar currents is strongly suppressed because the dominant M1 transition for $pp \to \Delta^+ p \to pp$ is forbidden if the protons are initially in the $^1S_0$ state[8] and therefore only higher order E1, M2, E2 multipoles contribute [27, 28]. The Δ-production is further suppressed by selecting the "dip" region of the energy transfer spectrum[9], because the probability of exciting a Δ resonance is small if the energy transfer ω is below the optimal Δ-production energies[10].

The particular choice of kinematics was largely supported by cross-section calculations shown in figure 1.6. They were made for $^{16}O(e,e'pp)^{14}C\,(GS)$ reaction in super-parallel kinematics, using simple correlations parametrization (SM-SRC) containing only SRC and a more sophisticated parametrization (SF-B) containing both SRC and LRC. Both calculations were made

[8] In order to be correlated the protons must be in the same orbit (shell). According to Pauli principle their spins should be antiparallel, which gives $\vec{S} = 0$. If they are ejected at an angle $\gamma = 180°$, this implies there was no orbital motion, i.e. $\vec{L} = 0$ (if the Fermi motion is neglected). Hence two anti-parallel protons must be in $^1S_0$ state.

[9] The region in the energy transfer spectrum between two broad peaks corresponding to quasielastic scattering and Δ excitation.

[10] $\omega < \sqrt{(\vec{q}+\vec{p_p})^2 + m_\Delta^2} - m_p$.

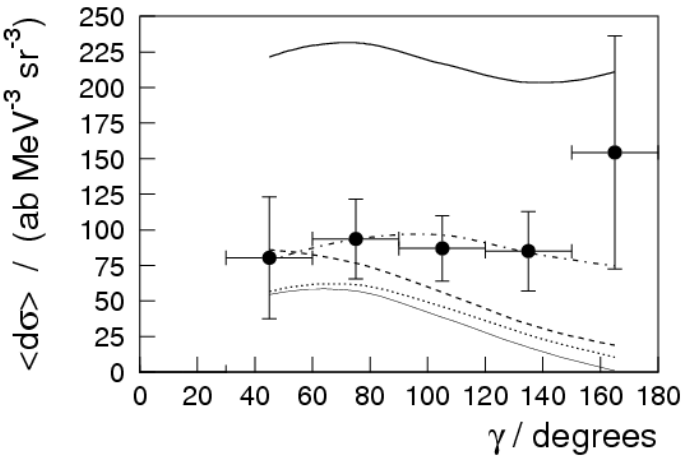

Figure 1.5: Proton-proton angular correlation function for missing energies $E_m < 70\ MeV$. γ is the angle between two protons, where one is emitted in the direction of the momentum transfer. The points are the measured values and the curves represent calculations using various SRC models. The thin full line at the bottom is the calculation of the Δ-contribution, without any SRC. From [33].

with and without two-nucleon final state interactions (NN-FSI), the details can be found in [32]. The calculations show that the NN-FSI are negligible for the chosen kinematics, as the lines obtained with and without NN-FSI overlap. A calculation was made for the $^{12}C(e,e'pp)^{10}Be\,(GS)$ reaction in the same kinematics [34], but only using the simple SM-SRC parametrization, with and without NN-FSI. In this case the lines overlap as well, which means that the NN-FSI are negligible for the reaction on ^{12}C as well. Based on the results for ^{16}O one can expect an enhancement of the cross-section when calculated with SF-B parametrization of correlations.

For all the reasons mentioned above, the measured cross-section is expected to be largely dominated by SRC effects in the chosen kinematics.

Target

The choice of target was governed by the following criteria:

- The target should have a well defined thickness to guarantee reliable luminosity determination.
- The experimental resolution should be good enough to separate the ground state of the remaining A-2 nucleus.

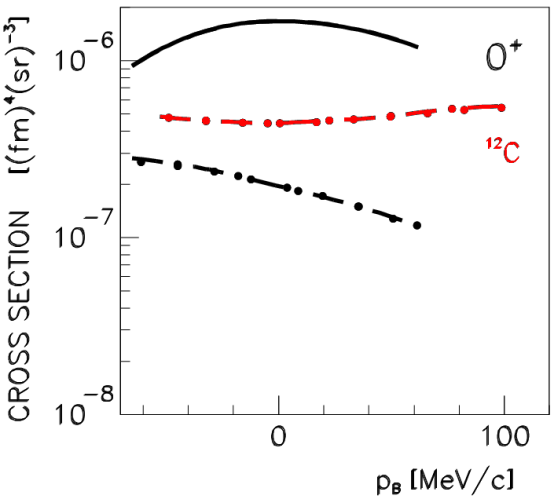

Figure 1.6: The cross-section calculation for super-parallel kinematics, $\omega =$ 160 MeV, $|\vec{q}| = 192$ MeV/c, $\theta_q = 27.5°$. The black lines represent the cross-section for $^{16}O(e,e'pp)^{14}C\,(GS)$ reaction. Dotted: calculation using the SM-SRC parametrization, dash-dotted: SM-SRC parametrization with NN-FSI, dashed: SF-B parametrization, full: SF-B parametrization with NN-FSI [32]. The dotted and dash-dotted lines, as well as dashed and full lines overlap. The red lines (the middle ones) represent the cross-section for $^{12}C(e,e'pp)^{10}Be\,(GS)$ reaction. Dotted: calculation using the SM-SRC parametrization, dash-dotted: SM-SRC parametrization with NN-FSI [34]. The dotted and dash-dotted lines overlap.

These criteria are easily satisfied by a graphite target. This is a standard target in A1-collaboration measurements at MAMI, thus the behavior of the detectors in the experiments of electron scattering on ^{12}C is well known. Being a solid-state target, its thickness can be well determined. The remaining ^{10}Be nucleus has the first excited state at 3.3 MeV, which can be separated from the ground state with the accessible experimental resolution.

1.2.4 Previous measurements on ^{12}C

Measurements of SRC effects in ^{12}C have been made at NIKHEF, MAMI and JLAB. This section tries to review these experiments in a historical order.

The NIKHEF measurements reported in [35] were performed in the Δ-resonance region at $(\omega, |\vec{q}|) = (310\text{ MeV}, 343\text{ MeV/c})$. Some evidence of the SRC in carbon was obtained, but with limited statistics. The first study of the exclusive (e,e'pp) reaction in the "dip" region at $(\omega, |\vec{q}|) =$

(212 MeV, 270 MeV/c) is reported in [36]. This experiment provided strong evidence of SRC effects, but suffered from low resolution (6 MeV FWHM) which had prevented separation of final states in the recoiling nucleus and thus the determined cross sections were integrated over a range of states.

Another study of the (e,e'pp) reaction on carbon in the "dip" region at $(\omega, |\vec{q}|) = (225 \text{ MeV}, 412 \text{ MeV/c})$ was performed at MAMI [33]. These measurements were made in close to 4π-geometry measuring the angular correlation function of two knocked-out protons (fig. 1.5). It was shown that the largest sensitivity to NN-correlations is to be expected in super-parallel kinematics. A pilot experiment in this kinematics was performed at MAMI, but with the ^{16}O nucleus [37, 38].

An experiment measuring the ratio of the $^{12}C(e, e'p)$ to $^{12}C(e, e'pp)$ events was done at JLAB [39, 40]. The measurements were made at high momentum transfer $(\omega, |\vec{q}|) = (865 \text{ MeV}, 1650 \text{ MeV/c})$. They report that 20% of nucleons in ^{12}C behave as correlated pairs, out of which 90% are np pairs and 5% are in form of pp and nn pairs.

1.3 Delta resonance in nuclear medium

In order to answer the question: "Do hadrons in a nuclear medium behave the same way the free hadrons do?", their properties have been investigated experimentally by quite a many observables, as well as in theoretical calculations. One way to research these properties is production of hadrons inside nuclei. Several experiments using hadron probes have reported hints of different hadron behavior in nuclear medium. Some of them were performed by Heidelberg-Saclay collaboration at CERN PS and they involved production of Σ-hypernuclei in $A(K^-, \pi^-)$ reactions. They reported observation of narrow Σ-hypernuclear states [41, 42]. This came as a surprise, because the strong interaction channels $\Sigma N \rightarrow \Lambda N$ should lead to prompt decay of these states, making their width ~ 100 MeV. These measurements were performed at relatively low momentum transfer $|\vec{q}| < 100$ MeV/c. Experiments at Brookhaven [43, 44] and KEK [45, 46] tried to repeat these observations at higher momentum transfers $|\vec{q}| \approx 300$ MeV/c, but with negative results. Another attempt was investigation of $^{12}C(\pi^+, p)^{11}C_{\Delta^+}$ reaction by Heidelberg-SIN/PSI collaboration [47], but the resolution and statistics were inadequate to give conclusive evidence on changes of hadron properties [48]. Recent experiments that explored in-medium effects on ω, K^0, ϕ mesons [49–51] obtained hints of the medium influence on their properties, while the experiment with ρ mesons [52] observed no significant evidence.

The existence of narrow bound Δ-states in nuclei, according to cur-

rent nuclear models, is even less probable than the existence of narrow Σ-hypernuclear states. The width of the free Δ due to $\Delta \rightarrow N\pi$ channel is already $\Gamma_{\mathrm{FWHM}} \approx 120$ MeV, which is large enough to exclude the existence of narrow states. In nuclear medium additional $\Delta N \rightarrow NN$ decay channels open and decrease the resonant state's lifetime and hence increase its width. Nevertheless, experiments of $e+{}^{12}C \rightarrow {}^{12}C_{\Delta^0} + e' \rightarrow {}^{11}C + e' + p + \pi^-$ reaction that were performed at MAMI, gave surprising evidence that narrow Δ^0-states may be observed [53].

1.3.1 ^{12}C(e,e'pπ^-)^{11}C reaction at MAMI

The ${}^{12}C(e, e'p\pi^-){}^{11}C$ reaction was investigated at MAMI within the A1-collaboration in 1996 and 1997 [53]. This was an exclusive, triple-coincident measurement, where the outgoing electron, proton and pion were detected by three large magnetic spectrometers [3]. The basic idea was to kinematically distinguish the following two situations: one where a "quasi-free" delta is formed on the struck nucleon and the other where a "bound" delta is produced. In the former case the Δ takes all the momentum transfer and consequently the decay proton and pion fly at very forward angles in the laboratory frame. In the latter case the Δ is formed on a bound nucleon and it remains bound for some time, as the whole nucleus takes the momentum transfer. Consequently this Δ is slower by a factor $\approx m_\Delta / m_{^{12}C}$ so the decay particles p and π will more probably come out at larger angles in laboratory system.

For the reaction in question, the missing energy and momentum are defined as:

$$E_m = M_{^{12}C} + \omega - E_p - E_{\pi^-} \tag{1.18}$$

$$\vec{p}_m = \vec{q} - \vec{p}_p - \vec{p}_{\pi^-} \tag{1.19}$$

and the missing mass is:

$$m_m = \sqrt{E_m^2 - \vec{p}_m^{\,2}} = E_x + M_{^{11}C} \tag{1.20}$$

where E_x is ${}^{11}C$ excitation energy. We also define $\hat{\omega}$ as:

$$\hat{\omega} = W - M_{^{12}C} \tag{1.21}$$

where W is the invariant mass of the reaction.

The measurement described in [53] used spectrometer B (5.6 msr) to detect the electron, while proton and pion were detected by spectrometers A (28 msr) and C (28 msr) respectively. The experimental setup had an

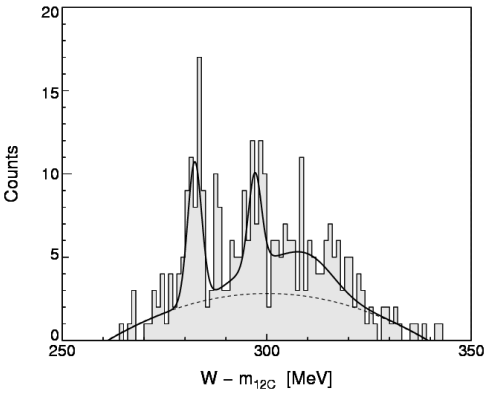

Figure 1.7: $\hat{\omega}$ spectrum for $|\vec{q}|$=370 MeV/c. The line represents a fit with quadratic background, according to the model from [53].

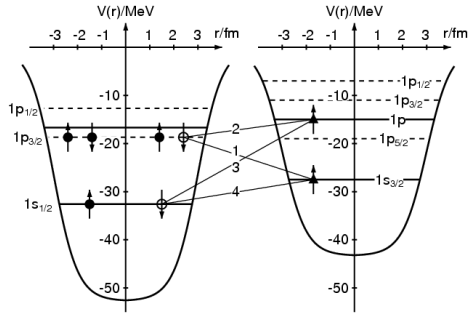

Figure 1.8: Energy eigenvalues in the Woods-Saxon potential for neutrons (left) and bound Δ^0 (right). From [53].

excellent missing mass resolution of $\Delta m_m = 0.63$ MeV/c^2 (FWHM) which enabled separation of the ground state in ^{11}C.

The true triple-coincident events should have the proton and the pion coming out back-to-back (in the center-of-mass system of the Δ^0). If any rescattering in the final state happens, this back-to-back correlation is destroyed due to small acceptance of the spectrometers, therefore a triple-coincidence condition minimizes final-state rescattering. Additionally, by selecting the events in ^{11}C ground state, any energy transfer caused by final state interaction is excluded, so FSI between the proton and the pion is minimal for the selected configuration. The $\hat{\omega}$ spectrum, with the described cuts on triple-coincidences and ^{11}C ground state is shown in the figure 1.7. Two narrow peaks seem to appear at $\hat{\omega} = 282.4$ MeV and at $\hat{\omega} = 296.2$ MeV.

1.3.2 A schematic model for narrow bound Δ

The spectrum shown in the figure 1.7 may be interpreted as appearance of narrow Δ^0 states. The narrowness can be understood if one thinks of the Δ^0 as bound in the nucleus. In that case it would have a sharp spatial and energy localization and hence narrow peaks would appear in the energy transfer spectrum. A schematic model that offers theoretical approach to explain these results had been developed. It is shortly presented in [53] and laid out in more detail in [54].

In the model, the Δ^0 is assumed to be bound in a central potential of the Woods-Saxon form, like the neutron from which it originates. The en-

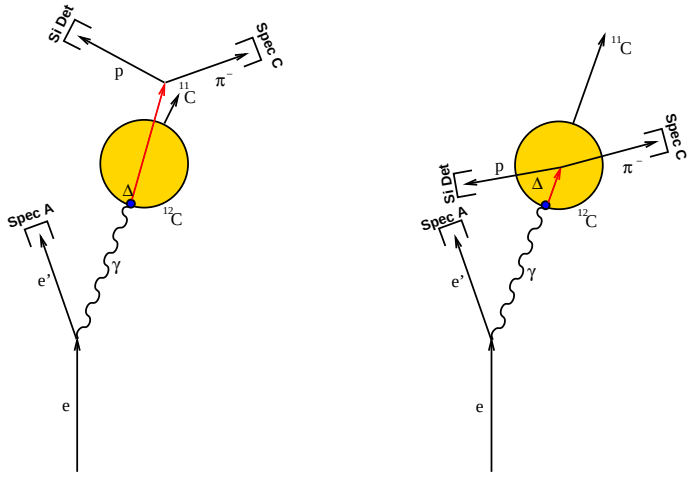

Figure 1.9: Schematic view of two reaction mechanisms. Quasi-free Δ knock-out (left) and bound Δ production (right).

ergy eigenvalues for the neutron and the delta are shown in figure 1.8. The calculated transition energies for transition 1 (ps) and 2 (ss) are $\hat{\omega} = 283.3$ MeV and at $\hat{\omega} = 295.8$ MeV respectively, which is in a surprisingly good agreement with the measured data.

1.3.3 Measurements with the Silicon Detector

Triple-coincidence measurements generally suffer from low statistics and one way to get around this problem is to increase the angular acceptance of the detector system. Based on this idea, as explained in [55], new measurements of the exclusive $^{12}C(e, e'p\pi^-)^{11}C$ reaction were performed in 2005 and 2006. In these measurements the Silicon Detector (88 msr) was used for proton detection whereas the electron and the pion were detected by magnetic spectrometers A (28 msr) and C (28 msr), respectively. The main motivation was to obtain more statistics supporting the evidence of the narrow Δ-states.

The choice of kinematics was governed by the ideas from [53]. In short, it was assumed that two possible mechanisms of Δ production, depicted in figure 1.9, could be kinematically distinguished. This assumption was supported by results of the Monte-Carlo simulation (figure 1.10), that suggested it was possible to position the detectors at such angles to suppress the particles from quasi-free delta decay and to favor the ones originating from bound delta decay.

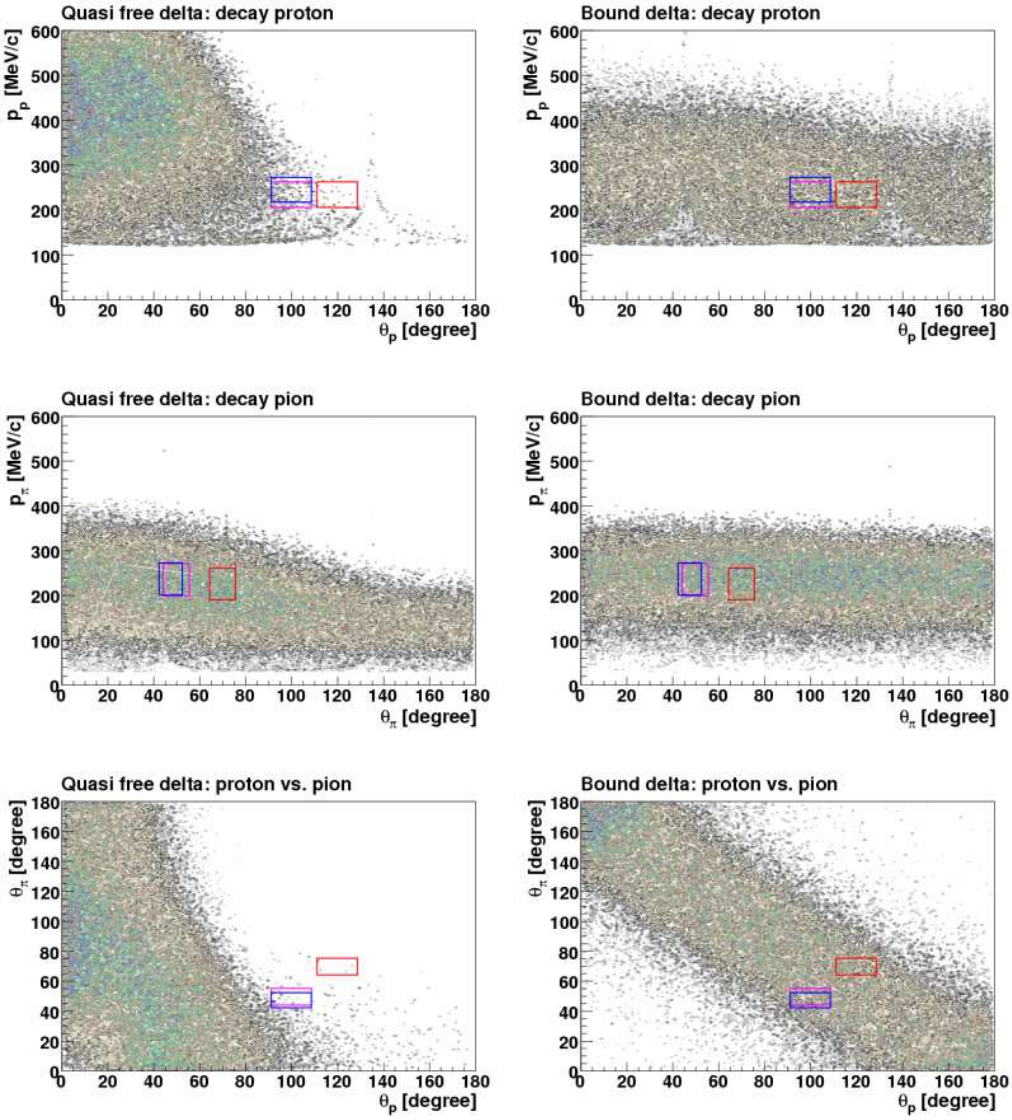

Figure 1.10: Simulation of the phase-space for the quasi-free reaction mechanism (left panels) and bound delta production (right panels). The "peak" structures visible in phase-space come from particle scattering off target-cell walls. The red, blue and magenta rectangles depict detector acceptances for kinematics chosen during 2005 and 2006 beam-time.

Chapter 2

Experimental Facility

An overview of the experimental setup with its main components is given in this chapter. The Silicon Detector is left out, as it is described separately in chapter 3.

2.1 MAMI accelerator

Mainzer Microtron (MAMI) [1, 2] is a continuous wave electron accelerator consisting of five stages: a linear accelerator, three race-track microtrons (RTM) and a harmonic double-sided microtron (HDSM). A schematic overview is shown in the figure 2.1. The RTMs consist of accelerating cavities placed between two magnets of high precision, which enable recirculation of the beam. The HDSM consists of two sets of cavities forming two antiparallel linear accelerators. The linacs are placed between four combined function magnets which ensure bending of the beam.

2.1.1 Beam properties

The electrons for the unpolarized beam are produced by a thermoionic source, or if the polarized beam is desired the electrons are produced by photoelectric effect using polarized laser light on a GaAs crystal. The electrons are first accelerated by a linear accelerator to 3.5 MeV and then sent to the first RTM stage where they recirculate until they are extracted with an energy of 14.9 MeV. The same is repeated in the RTM2 which they exit with an energy of 180 MeV. The fourth stage RTM3 accelerates the electrons up to 855 MeV in 15 MeV steps, at which the beam can be extracted. Finally, the fifth stage can accelerate the beam to the maximum energy of 1.5 GeV.

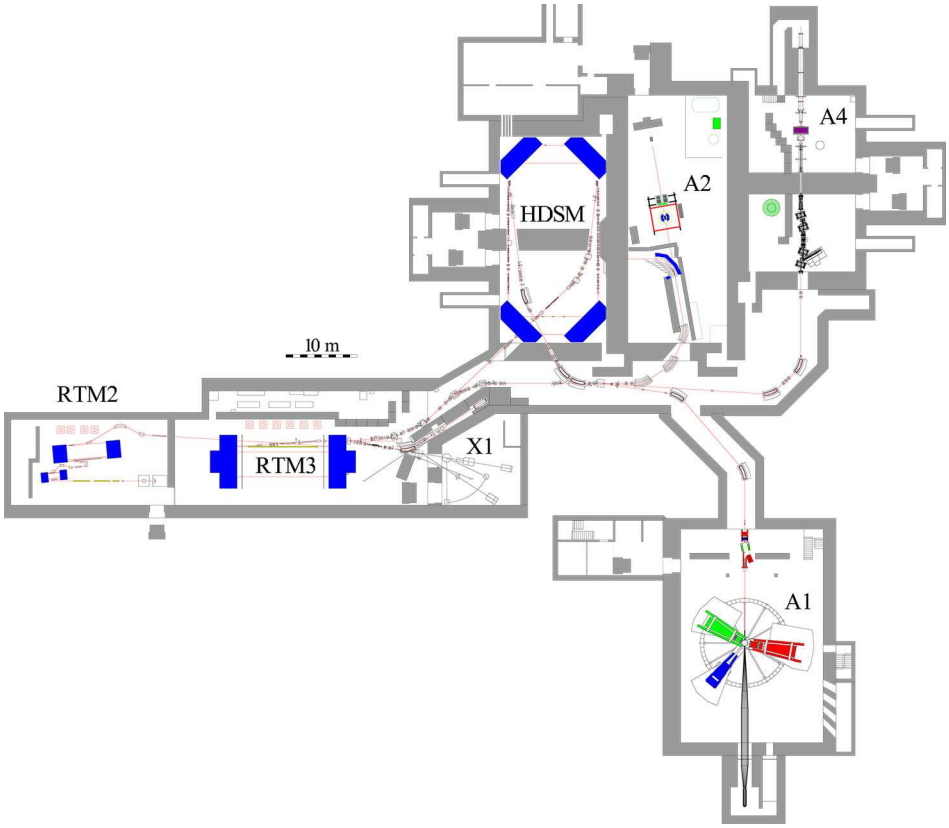

Figure 2.1: Overview of the MAMI facility showing accelerator stages and experimental halls. The A1-hall with the 3-spectrometer facility is in the lower right. From [1].

The accelerator can deliver unpolarized electron beams with the maximum current of 100 μA, or the polarized beams up to 80 μA, with 75% polarization. The beam root mean square (RMS) energy spread is 30 keV at 855 MeV and 110 keV at 1.5 GeV.

2.2 Magnetic spectrometers

The A1-collaboration at MAMI operates three high resolution magnetic spectrometers, which are labeled A, B and C. All three spectrometers can be rotated around the target and they can operate in single, double or triple coincidence mode. The A1 experimental hall together with the spectrometers is shown in the figure 2.2 and the detailed description of the facility is given in [3]. The following subsections summarize their optical properties and briefly describe the detector packages.

Figure 2.2: The A1-hall with the 3 magnetic spectrometers. From left to right the spectrometers are labeled as A (red), B (blue) and C (green). The electron beam is coming through the pipe from the left side.

Spectrometer	A	C
Configuration	QSDD	QSDD
Max. momentum [MeV/c]	735	551
Cent. momentum [MeV/c]	665	490
Momentum acceptance [%]	20	25
Solid angle [msr]	28	28
Horiz. angl. accept. [mrad]	±100	±100
Vert. angl. accept. [mrad]	±70	±70
Scatt. angle range [°]	18-160	18-160
Momentum res.	$\leq 10^{-4}$	$\leq 10^{-4}$
Angular res. at target [mrad]	≤3	≤3
Position res. at target [mm]	3-5	3-5

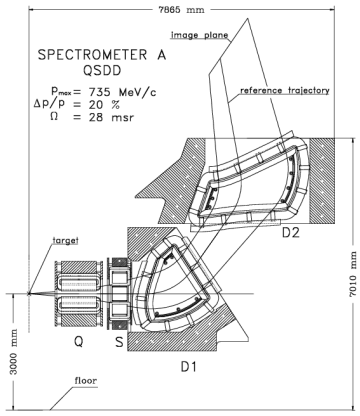

Spectrometer	B
Configuration	D
Max. momentum [MeV/c]	870
Cent. momentum [MeV/c]	810
Momentum acceptance [%]	15
Solid angle [msr]	5.6
Horiz. angl. accept. [mrad]	±20
Vert. angl. accept. [mrad]	±70
Scatt. angle range [°]	7-62
Momentum res.	$\leq 10^{-4}$
Angular res. at target [mrad]	≤3
Position res. at target [mm]	1

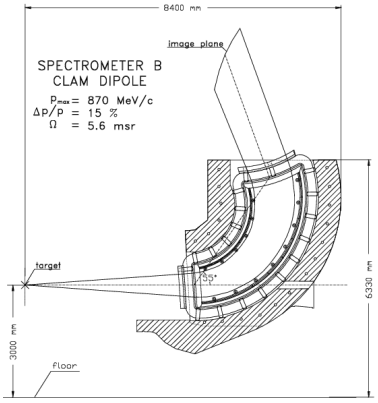

Table 2.1: Main parameters of the magnetic spectrometers. From [3].

2.2.1 Optical properties

Spectrometer A uses quadrupole-sextupole-dipole-dipole (QSDD) configuration of the magnets which enable measurement of high particle momenta and a relatively large acceptance (28 msr). Spectrometer B uses a single magnet (clam-shell dipole) which enables higher spatial resolution, but smaller acceptance (5.6 msr). It is relatively compact so it can be positioned at small scattering angles (down to 7°). Spectrometer C is 11/14 down-scaled version of spectrometer A. Their main properties are summarized in table 2.1.

The central magnetic field in the spectrometers, and thus the central momentum, are determined by means of Hall and NMR probes. While the Hall probes give a rough measure of the magnetic field, the NMR makes very precise measurements with an error smaller than the energy spread of the electron beam.

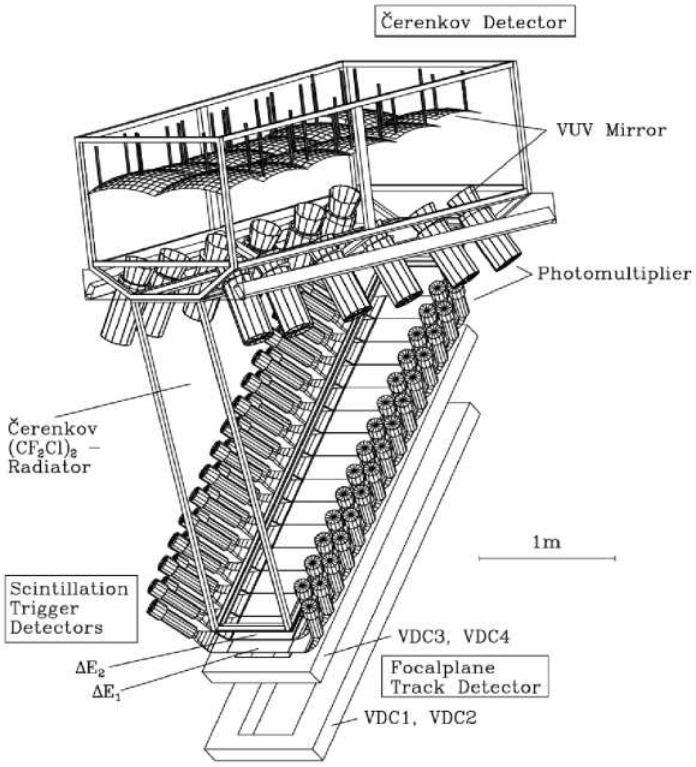

Figure 2.3: The drawing of spectrometer's detector package consisting of four VDCs, two layers of scintillators and a Čerenkov detector. From [3].

2.2.2 Detector package

All three spectrometers have similar detector packages consisting of four drift-chambers, scintillators and a Čerenkov detector. The drift-chambers are used for particle trajectory reconstruction and the scintillators for triggering and particle identification. As electrons (positrons) and pions cannot be distinguished by the scintillators, the Čerenkov detector is used to discriminate them. The detectors are schematically shown in the figure 2.3.

Vertical drift chambers

Two pairs of vertical drift chambers (VDC) are placed in the focal plane, which is inclined 45° with respect to the reference particle trajectory. One chamber in each pair has wires in the non-dispersive direction, labeled as y_{fp} and the other has wires rotated 40° with respect to y_{fp}. The former is used to measure the track in the dispersive direction, while the latter measures the projection of the track in the non-dispersive direction.

The VDCs consist of equally spaced signal and potential wires between cathode foils, placed in a gas mixture of argon and isobuthan. The wires are grounded while the foils are set at negative potential of 5600-6500 V. When a particle traverses the chamber it produces ionization and the electrons drift towards the wires with a known velocity. Typically a particle induces signals in at least three and up to seven wires. The trigger is given by plastic scintillators placed behind the VDCs. The wires stop the time measurement started by the scintillators and the time information of each wire is translated into distance giving particle track. By using two pairs of chambers (instead of only one) the spatial resolution is increased by an order of magnitude and it is $\leq 200\ \mu m$ in the dispersive and $\leq 400\ \mu m$ in the non-dispersive direction. The focal plane coordinates measured by the VDCs are translated to the target coordinates by means of the magnetic field map.

Scintillators

Two segmented planes of plastic scintillators are placed above the drift chambers. The detectors in the first plane (dE-plane) are 3 mm thick and those in the second plane (ToF-plane) are 1 cm thick. The segmentation (15 segments in spectrometers A and C, 14 segments in spectrometer B) enhances the time resolution and gives a rough position of the particle track.

The role of the scintillators is to provide the trigger for the time measurement in the VDCs, to provide time information for coincidence timing and to measure the energy deposition. Typically the second (thicker) layer gives the fast timing signal, but the first layer can also be used for low energy protons or deuterons. The protons can be separated from minimum ionizing particles by their energy deposition in the two layers. The pions cannot be separated from electrons and positrons, therefore the Čerenkov detector has to be used.

Čerenkov detector

The Čerenkov detector contains gas $(CF_2Cl)_2$ in which electrons or positrons with energy > 10 MeV create Čerenkov light. The Čerenkov photons are transmitted through the gas, reflected by special mirrors and then collected by photomultipliers. The energy threshold lies at 2.7 GeV for pions, but pions with such an energy are never produced by the 1.5 GeV beam. Consequently, only electrons or positrons can produce a signal in the Čerenkov detector and this fact is used to separate them from other particles.

2.3 Target

The target is located inside the vacuum scattering chamber, which lays between the spectrometers on their rotation axis. Various solid state materials can be mounted on the target ladder. Its vertical position is remotely controlled and the desired material can be selected during the beam-time. Three solid state materials were used in experiments described in the thesis:

- Graphite - ^{12}C , 43.86 mg/cm^2
- Polyethylene - CH_2, 28.20 mg/cm^2
- Beam monitor - Al_2O_3

The target can be rotated around the spectrometer axis when necessary.

2.4 Trigger and data acquisition

Each of the three spectrometers has independent electronics located on spectrometer's platforms. The electronics is responsible for signal amplification and analog-to-digital conversion, as well as for trigger generation. The purpose of the trigger electronics is to select "good events" for further processing. The basic trigger condition is imposed on the scintillators: at least one segment in one of the layers must be hit in such way that the photomultipliers on both ends produce signals larger than set thresholds. This condition can be extended by demanding coincidence of both scintillator layers (dE and ToF) or by selecting only one of them. The trigger condition can also be put in coincidence or anti-coincidence with the information from the Čerenkov detector. A programmable lookup unit (PLU) enables selection between these conditions during a beam-time [3, 56].

When the PLU of one of the spectrometers detects a good event, the information is sent to a universal logic module (ULM) [57]. This module receives information from all three spectrometers, with a possibility to change the width and the position of the coincidence signals. Based on the information received from the spectrometers there are seven types of events: singles A, singles B, singles C, doubles AB, doubles AC, doubles BC and triples ABC. It is possible to scale each of these event types via prescalers if the suppression of any of them is needed. Finally, when the ULM accepts an event the gate signals are distributed to start analog-to-digital conversion (e.g. signal amplitudes, drift times, etc.) and also the interrupt signal is given to front-end computers to read out all the data busses. During the signal conversion and read-out the electronics cannot accept further events and a "busy" signal is

issued by the so-called micro busy module. This "busy" time is measured by scalers and the information can be later used for dead time calculation.

As the spectrometers are read-out asynchronously additional information is needed for later synchronization of multi-arm events. This is achieved by using the "event-builder" module. This module generates a unique event number which is inserted into the data stream of each detector and enables merging of single-arm information. Software for data acquisition is further described in C.1.

The trigger logic described in this section was originally designed for the spectrometers. In the experiments performed in the framework of this thesis, the Silicon Detector was simply inserted into the trigger logic and data stream instead of the spectrometer B or the spectrometer C. The trigger generation for the Silicon Detector is described in more detail in 3.6.

Chapter 3

Silicon Detector

The motivation for building a system of silicon detectors comes from idea of using a simple, cost-effective, large acceptance detector in experiments that suffer from low statistics. This detector is intended for operation in high particle flux environment, where it is important to maintain the desired energy resolution. This chapter describes the Silicon Detector that was built and put in operation within the A1-collaboration at MAMI and represents the main part of this thesis.

3.1 Theoretical introduction

3.1.1 Semiconductors in general

The band structure

All crystalline materials exhibit energy-band structure in the outer shell atomic levels. This structure comes from interplay of Pauli principle and close periodic arrangement of the atoms in the crystal. Such arrangement causes overlap of the outermost-shell electron wave functions, but the Pauli principle forbids having two atoms with same quantum numbers. Consequently the levels split (the degeneracy is removed)[1]. The splitting is so small that these discrete levels form bands, the conduction band and the valence band. The gap between these bands is what makes the difference between different materials. It is around 6 eV in insulators, around 1 eV in semiconductors and non-existent in metals where the two bands overlap. In general, the electrons in the valence band are tied to lattice atoms, but the

[1] The splitting occurs $N_{cryst}/2$ times, where N_{cryst} is the number of atoms in the crystal and the factor 2 comes from two possible electron spin orientations.

ones in the conduction band are free to move around crystal. If an external electric field is applied these electrons will form a current.

Charge carriers

The energy gap between the valence and the conduction band in semiconductors is around 1 eV. At room temperature some electrons will have enough thermal energy to jump to the conduction band leaving their original position in the valence band vacant. This vacancy or hole is easily filled by neighboring electrons. When the same process is repeated with the neighboring atoms the hole seems to move through the crystal as if it were a positive charge carrier. Hence, when an external electric field is applied to the semiconductor, the current arises from two sources: the electrons moving in the conduction band and the holes moving in the valence band.

Due to the applied electric field and the interaction with the crystal lattice, the charge carriers will drift through the crystal. The drift velocities are related to the applied field by the following relations [58]:

$$\vec{v}_e = \mu_e \vec{E} \tag{3.1}$$

$$\vec{v}_h = \mu_h \vec{E} \tag{3.2}$$

where μ_e and μ_h are electron and hole mobilities, respectively. They are functions of temperature and the applied electric field, as shown in the figure 3.1. For silicon at 300 K, μ_e and μ_h are constant if $|\vec{E}\,|<10^3$ V/cm. For $10^3<|\vec{E}\,|<10^4$ V/cm the mobilities are proportional to $|\vec{E}\,|^{-1/2}$ and if the electric field is $|\vec{E}\,|>10^4$ V/cm they vary as $\sim |\vec{E}\,|^{-1}$ [58]. Consequently the drift velocity saturates at very high electric fields because electrons and holes transfer a proportional fraction of their kinetic energy to the crystal lattice during the collision with the lattice atoms.

Doped semiconductors

The intrinsic (pure) semiconductors have the same number of negative (electrons) and positive (holes) charge carriers. By introducing impurities in the crystal lattice, the number of charge carriers of one type can be dramatically increased. Silicon and germanium have four electrons in the outer shell, which form four covalent bonds with neighboring atoms. If one introduces an impurity with 5 valent electrons, a donor, it will leave an excess electron and a n-type semiconductor will be formed. By doping with a tri-valent impurity, an acceptor, an extra hole will be produced and a p-type semiconductor will be formed.

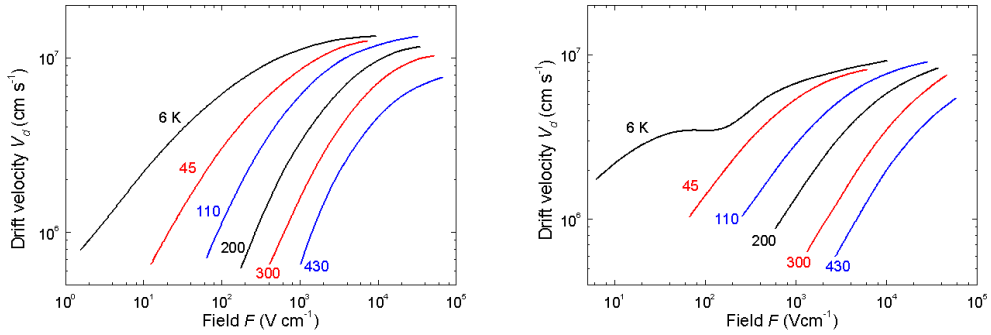

Figure 3.1: Electron (left) and hole (right) drift velocities vs. electric field in silicon at different temperatures [59].

The impurities introduce additional levels in the energy gap between the valence and the conduction band. By choosing the right dopand one would like to produce these levels near the conduction band in the case of a donor level or near the valence band in the case of an acceptor level. Most commonly used dopand for producing n-type[2] materials is phosphorus which introduces a donor level just 0.044 eV below the conduction band. This way, the electron is easily excited to the conduction band where it contributes to material's conductivity. In contrast to the above mentioned impurities, often called shallow impurities, there are impurities that introduce levels deep inside the forbidden band. These can act as trapping or recombination centres, reducing the number of free charge carriers.

In an n-type semiconductor the electrons are called the majority carriers while the holes are called the minority carriers[3]. The majority carriers form the main contribution to the current. The dopand concentration is usually of the order of 10^{13} atoms/cm^3 which is low compared to silicon density of $\sim 10^{22}$ atoms/cm^3. For any semiconductor the following relation holds [58]:

$$np = n_i^2 = AT^3 e^{-\frac{E_g}{kT}} \tag{3.3}$$

where n and p are electron and hole concentrations respectively, n_i is intrinsic concentration, A is a temperature independent constant and E_g is the energy gap. Since the material must be neutral, sum of the charge concentrations is:

$$N_D + p = N_A + n \tag{3.4}$$

[2]The silicon detectors described in the thesis are made of n-type material.

[3]And vice-versa for a p-type semiconductor.

N_D being the concentration of donors and N_A the concentration of acceptors. It follows that in an n-type material, where there are no acceptors, the electron concentration is $n \simeq N_D$ and in a p-type material, where there are no donors, the carrier concentration is $p \simeq N_A$. The intrinsic concentration for silicon at 300 K is $\sim 1.5 \times 10^{10}$ cm^{-3}.

In practice, a material is never 100% pure, it always contains a certain amount of impurities that can act like donors or acceptors. Thus the type of the semiconductor is determined by the net dopand concentration:

$$N_{eff} = N_D - N_A \tag{3.5}$$

pn junction

When an n-type and a p-type semiconductor are brought together, a region with special properties called a pn-junction is formed around the area of contact (see figure 3.2). The initial difference in electron and hole concentrations in two different material types causes diffusion of majority carriers: the electrons diffuse from n into p and the holes the other way round. During this process the electrons and the holes recombine leaving the area depleted from free charge carriers. The charge of the donor and the acceptor ions, called the space charge, forms in this area an electric field that eventually stops the diffusion and brings the junction into a steady state with a fixed width of the depleted region. It can be shown [58] that the extent of the depletion zone in n and p type is given by:

$$x_n = \sqrt{\frac{2\epsilon V_0}{eN_D(1 + N_D/N_A)}} \tag{3.6}$$

$$x_p = \sqrt{\frac{2\epsilon V_0}{eN_A(1 + N_A/N_D)}} \tag{3.7}$$

where ϵ is the dielectric constant and V_0 the contact potential. The total width of the depleted zone is given by the sum $d = x_n + x_p$. It follows from equations 3.6 and 3.7 that the depleted area is farther extended into the less doped material. For example, a p^+n diode[4] consists of a thin heavily doped p-layer on an n-type bulk[5]. In that case $N_A \gg N_D$, so the depletion width is:

$$d \simeq x_n \simeq \sqrt{\frac{2\epsilon V_0}{eN_D}} \tag{3.8}$$

[4]This example occurs throughout the thesis, as it is the structure of the MSX detectors, see A.1.2.

[5]The '+' sign denotes a heavily doped material.

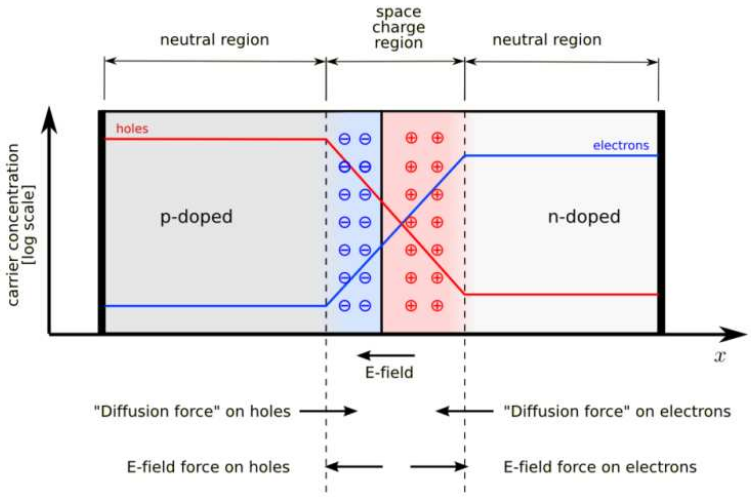

Figure 3.2: Formation of a pn-junction. In this case no external voltage is applied.

and it extends almost exclusively into the n-type material. For low electric fields (E<1000 V/cm) the mobility is (almost) constant. Thus by substituting $1/\rho_n \simeq eN_D\mu_e$ we get a simple relation [58] for the width of the depleted region:

$$d \simeq \sqrt{2\epsilon\rho_n\mu_e V_0} \simeq 0.53\sqrt{\rho_n V_0}\ [\mu m] \tag{3.9}$$

Semiconductors as charged-particle detectors

Semiconductor junctions can be used as particle detectors. If the traversing particles are charged, they excite atomic electrons producing e-h pairs their number depending on the deposited energy. If this happens in the depleted area, the charges are swept by the electric field and drift towards the contact electrodes. The drifting carriers induce currents in the contact electrodes which can be measured. When no external potential is applied the depleted layer is relatively thin. In order to increase this layer and in this way the sensitive volume of the detector, reverse bias voltage V_B has to be applied[6]. By assuming $V_B \gg V_0$ we can substitute V_0 by V_B in equation 3.8. More generally, N_D can be substituted by $|N_{eff}|$. The width of the depletion zone

[6]This means applying a negative voltage on the p-side and a positive voltage on the n-side of the detector.

in reversely polarized diode is then:

$$d \simeq \sqrt{\frac{2\epsilon V_B}{e|N_{eff}|}} \tag{3.10}$$

The depletion region is free of majority carriers which are swept by the electric field of the space charge and the external potential. Nevertheless, there are the minority charge carriers that move along the potential. They contribute to the leakage current, which grows with increasing bias voltage and constitutes a noise component of the detector.

3.1.2 Properties of silicon

Energy resolution and efficiency

An advantage of silicon detectors is that they can be operated at room temperature. The energy gap between the valence and conduction band in silicon at this temperature is 1.1 eV and the average energy to create an e-h pair is $w = 3.62\ eV$. The difference between these values is lost in collisions with the crystal lattice. The average energy to create an e-h pair w is independent of radiation type and energy. If a particle deposits energy ΔE in a detector, the total charge created will be $Q = ue\frac{\Delta E}{w}$, assuming collection efficiency u. As charges are built up on both sides of the reverse biased diode, it exhibits some properties of a charged capacitor. In planar geometry the capacitance is given by:

$$C = \epsilon\frac{A}{d} \tag{3.11}$$

where A is the area and d the width of the depleted zone and ϵ the dielectric constant, for silicon $\epsilon_{Si} \simeq 12\epsilon_0$ [58,60]. The voltage observed on the electrodes is:

$$V = \frac{Q}{C} = ue\frac{\Delta E}{w}\frac{d}{\epsilon_{Si}A} \tag{3.12}$$

It rises linearly with energy deposition, since constants in the above expression are independent of energy.

The intrinsic energy resolution of a silicon detector depends on the number of e-h pairs created (N). If particles pass through the detector, this number varies statistically according to Poisson distribution with standard deviation given by $\sigma = \sqrt{N} = \sqrt{\Delta E/w}$. Two energies are defined resolvable if their separation is larger than FWHM of the peaks. The intrinsic resolution is given by [58]:

$$R = 2.35\frac{\sqrt{N}}{N} = 2.35\sqrt{\frac{w}{\Delta E}} \tag{3.13}$$

If the particle is completely stopped in the detector, its total energy is transferred, in which case the number of e-h pairs created does not vary according to Poisson statistics. This introduces additional phenomenological factor to the standard deviation $\sigma = \sqrt{FN}$, called *Fano factor*, where $F < 1$. In this case the detector resolution is [58]:

$$R = 2.35\sqrt{F\frac{w}{E}} \tag{3.14}$$

Note that the total particle energy E enters the above equation, whereas ΔE is used in the relation 3.13.

Detection efficiency of silicon detectors for charged particles is close to 100% [58]. The lowest detectable energy is usually set by the noise in the detector and the electronics.

Noise

When the reverse voltage is applied to a pn-junction, it causes a flow of a small fluctuating current, which represents the background for the physical signal. This current is called *leakage current*, as it "leaks" through the reversely polarized junction, which is ideally nonconducting. The leakage current has three major contributions:

- leakage through detector surfaces, dependent on the detector mount, humidity, contaminants, etc. This is usually the largest contribution[7].
- e-h pairs thermally generated with help of traps and recombination centers in depletion region ($\sim \mu A/cm^2$).
- movement of minority carriers along the potential, usually the smallest contribution ($\sim nA/cm^2$).

Beside the influence on the energy resolution, the leakage current has a practical influence on detector's operation. The bias voltage is supplied through a resistor on the preamplifier, so the leakage current produces a voltage drop of $R\ I_{leak}$. The larger the current, the larger the voltage drop of the actual voltage applied to the junction, which must be properly compensated.

Semiconductor detectors are inevitably used with preamplifiers (and possibly other electronic devices), so care should be taken not only to minimize the noise from the detector, but also from the electronics. The preamplifiers are usually of charge sensitive type, because they are insensitive to changes

[7] In most cases the surface current is collected by the so-called *guard ring*. In the case of the p^+n-detector, the guard ring is formed by placing a p^+ layer around the active region. This prevents the leakage of the surface current over the detector edge.

in detector's capacitance, which varies with the reverse voltage. The preamplifier noise is usually quantified by equivalent noise charge:

$$ENC = \frac{eV_{RMS}}{w}C \tag{3.15}$$

where V_{RMS} is the average noise output voltage level and C is total input capacitance. The capacitance comes from the detector, but also from connection cables. Therefore, the detector and the preamplifier should be as close as possible to reduce the cable length and in this way the capacitance. According to the equation 3.11 the capacitance decreases by increasing the width of the depletion zone. By substituting equation 3.8 into 3.11 we obtain:

$$\frac{C}{A} \simeq \sqrt{\epsilon\frac{eN}{2V}} \tag{3.16}$$

Consequently the capacitance and the noise will decrease with higher bias voltage up to the point when the detector is fully depleted. By increasing the voltage beyond this value, the noise starts to grow again due to the growing leakage current.

Pulse formation

The electrical pulse on the electrodes arises from induction caused by movement of the charge carriers inside the detector. The time needed for collection of a single e-h pair depends on the location where it was created and the electric field in the depletion region. The shape and the rise time of the total pulse are determined by movement of all the charges created by the traversing particle. Therefore, the pulses will vary in risetime and shape depending on particle's energy and trajectory.

Let us consider a simple situation of a parallel plate p^+n detector, with a thin p^+-layer on a n-type bulk. The electric field at distance x from the ohmic side[8] is given by [61]:

$$E(x) = \frac{eN_D}{\epsilon}x + E_0 \tag{3.17}$$

When the detector is fully depleted we have $E(0) = 0$ and consequently $E_0 = 0$. E_0 can be described as the residual field contributing to overdepletion of the detector. Suppose an e-h pair is created at $x = x_0$, the hole will start to

[8]Ohmic side is the side where the ohmic contact between the semiconductor and the electrode is realized. In the case of the p^+n detector, this is the n-side. The side of the detector, where the pn-junction is formed, is called the junction side (in this case p-side).

drift toward the junction ($x = d$), and the electron toward the ohmic contact ($x = 0$). From 3.1 and 3.2 we obtain the following equations of motion:

$$\frac{dx_h}{dt} = \mu_h \left(\frac{qN_D}{\epsilon} x + E_0 \right) \tag{3.18}$$

$$\frac{dx_e}{dt} = -\mu_e \left(\frac{qN_D}{\epsilon} x + E_0 \right) \tag{3.19}$$

For the case of interest the mobilities can be considered independent of electric field. The integration with the initial condition x(t=0) = x_0 results in:

$$x_h(t) = -\frac{\epsilon}{qN_D} E_0 + \left(x_0 + \frac{\epsilon}{qN_D} E_0 \right) e^{\mu_h \frac{qN_D}{\epsilon} t} \tag{3.20}$$

$$x_e(t) = -\frac{\epsilon}{qN_D} E_0 + \left(x_0 + \frac{\epsilon}{qN_D} E_0 \right) e^{-\mu_h \frac{qN_D}{\epsilon} t} \tag{3.21}$$

Charge collection time for holes and electrons is defined as the time for the hole to reach the junction ($x = d$) or for the electron to reach the ohmic contact ($x = 0$), respectively:

$$t_h = \frac{\epsilon}{\mu_h q N_D} ln \frac{d + \frac{\epsilon}{qN_D} E_0}{x + \frac{\epsilon}{qN_D} E_0} \tag{3.22}$$

$$t_e = \frac{\epsilon}{\mu_e q N_D} ln \frac{x + \frac{\epsilon}{qN_D} E_0}{\frac{\epsilon}{qN_D} E_0} \tag{3.23}$$

Clearly, the charge collection times depend on the initial position of the pair, but also on the residual field E_0[9]. A charge q moving a distance dx will induce charge dQ on the electrode:

$$dQ = \frac{q dx}{d} \tag{3.24}$$

In other words, the observed current will be:

$$\frac{dQ}{dt} = \frac{q}{d} \frac{dx}{dt} \tag{3.25}$$

By inserting the equations 3.20 and 3.21 we get the current induced by a single electron or hole, respectively:

$$i_h(t) = \frac{q}{d} \mu_h \left(E_0 + \frac{qN_D}{\epsilon} x_0 \right) e^{\mu_h \frac{qN_D}{\epsilon} t} \tag{3.26}$$

$$i_e(t) = \frac{q}{d} \mu_h \left(E_0 + \frac{qN_D}{\epsilon} x_0 \right) e^{-\mu_e \frac{qN_D}{\epsilon} t} \tag{3.27}$$

[9]This shows the importance of overdepleting the detector for achieving faster signals.

The induced charge is obtained upon integration:

$$Q_h(t) = \frac{\epsilon}{dN_D}\left(E_0 + \frac{qN_D}{\epsilon}x_0\right)\left(e^{\mu_h \frac{qN_D}{\epsilon}t} - 1\right) \tag{3.28}$$

$$Q_e(t) = \frac{\epsilon}{dN_D}\left(E_0 + \frac{qN_D}{\epsilon}x_0\right)\left(1 - e^{-\mu_e \frac{qN_D}{\epsilon}t}\right) \tag{3.29}$$

By integrating again in the time windows $0 \leq t \leq t_h$ and $0 \leq t \leq t_e$ for the hole and the electron respectively, we obtain the total charge induced by each carrier:

$$Q_h = q\frac{d - x_0}{d} \tag{3.30}$$

$$Q_e = q\frac{x_0}{d} \tag{3.31}$$

This confirms that the total charge induced on one electrode is always:

$$Q_{tot} = Q_h + Q_e = q \tag{3.32}$$

The above consideration gives pulse shape induced by one e-h pair, under the assumption of mobilities independent of electric field. The real pulse has a more complicated form, as it contains contributions from all e-h pairs created along the particle track.

It is interesting to estimate charge collection times for the MSX detectors, that are a part of the Silicon Detector. The calculations are made for charges created near the junction, in the center or near the ohmic contact of the detector, assuming $d = 0.1\ cm$ and $N_D = 2.4 \times 10^{11}\ cm^{-3}$. The results are shown in the figure 3.3. The total charge induced on an electrode is always $Q = e$, but there is a time dependence on the initial position of the e-h pair, mainly due to different mobilities of electrons and holes. When the e-h pair is created near the junction side ($x = d$), the induction is mainly due to the electron movement and the charge collection time is relatively fast. On the other hand when the pair is created near the ohmic contact ($x = 0$), the induction is mainly due to the hole movement and the charge collection time is relatively slow. In the figure 3.3 one can also see the influence of detector overdepletion on the charge collection time. For a fully depleted detector, the charge collection time varies between $80\ ns - 300\ ns$, in the case of 33 % overdepletion ($E_0 = 0.33E_{FD}$) it varies between $30\ ns - 100\ ns$, and in the case of 66 % overdepletion ($E_0 = 0.66E_{FD}$) it varies between $20\ ns - 70\ ns$.

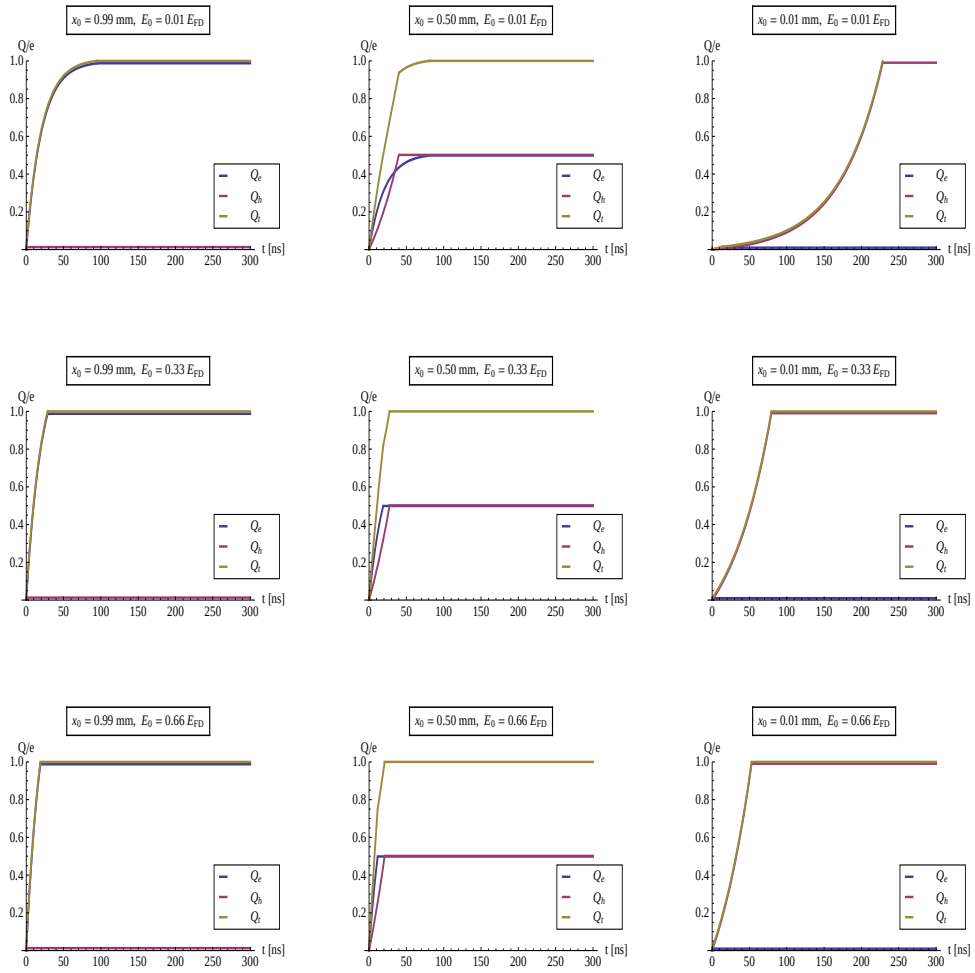

Figure 3.3: Charge induced by a single electron, hole, or both. Each row shows three cases: *left:* the e-h pair is created very close to the junction, *middle:* e-h pair is created in the middle of the depletion zone, *right:* e-h pair is created very close to the ohmic contact. The upper row corresponds to fully depleted detector, the middle one to 33% overdepletion, and the lower row to 66% overdepletion.

3.1.3 Radiation damage

Non-ionizing energy loss hypothesis

Irradiation of silicon causes detector damage which depends on the type and the energy of the incoming particles. It has been experimentally confirmed for protons, neutrons and pions that only the non-ionizing energy loss (NIEL) of incoming particles contributes to the detector damage [62, 63]. According to the NIEL hypothesis, the damage caused by different particles depends on the fluence Φ and it can be scaled to the damage caused by 1 MeV neutrons [64]. Thus the damage is usually expressed in terms of equivalent fluence of 1 MeV neutrons:

$$\Phi_{eq} = \kappa_A \Phi_A \tag{3.33}$$

for particles of type A, where hardness factor κ depends on the particle type and energy.

Defect classification

The defects caused by incoming particles are classified as bulk and surface defects. The surface defects can be controlled by proper design and manufacturing process, e.g. by introducing guard ring structure around the active area. The bulk defects include displacements of one or more of the lattice atoms. If only one atom is displaced from its position in the lattice a point defect is formed. The displaced atom leaves a vacancy in its original position and comes to rest in an interstitial position. Most of the vacancies and interstitials recombine, but some diffuse creating stable defects. If the recoiling atom has sufficient energy it can displace further lattice atoms creating a cluster defect. The bulk defects have the following consequences on bulk properties:

1. Introduction of new energy levels deep in the band gap. These are the main sources of the bulk generation current through capture and emission processes and contribute greatly to the leakage current [64]. Since the generation current is proportional to mid-gap defect concentration which is proportional to the total fluence of particles, the leakage current increases as [64, 65]:

$$\frac{\Delta I}{V} = \alpha \Phi_{eq} \tag{3.34}$$

where Φ_{eq} equivalent fluence of 1 MeV neutrons and α is the current-related damage constant. This constant is independent of the specific silicon material or type of irradiating particles, which is shown experimentally (figure 3.4). However, α depends on the temperature and

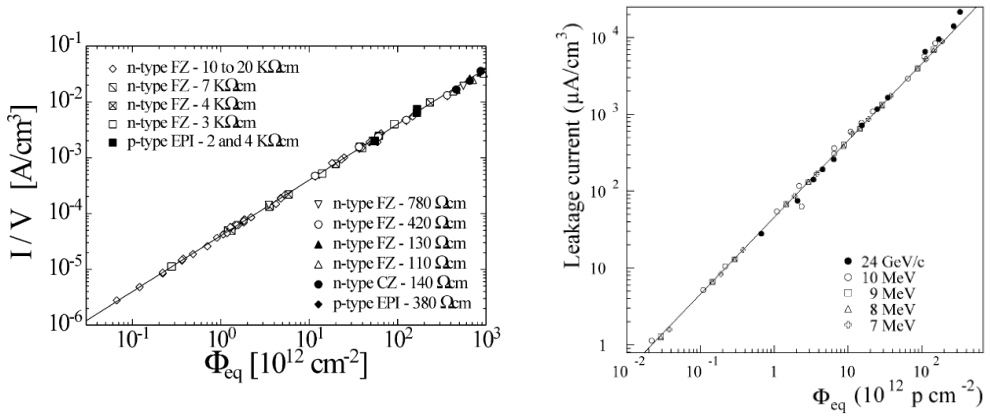

Figure 3.4: Leakage current as a function of 1 MeV neutron equivalent fluence. Left: for various silicon materials and processing technologies, from [66, 67]. Right: for irradiation with protons of different energies, from [68].

annealing time, so conventionally it is normalized to is value at 20° (see equation 3.42).

2. The defects can act as donors or acceptors, changing the effective dopand concentration N_{eff}. They introduce deep level acceptor-like states or remove initial shallow levels through cluster defect creation. In both cases the full depletion voltage V_{FD} is affected, which is clear if we write the equation 3.10 in the following way:

$$V_{FD} = \frac{e}{2\epsilon} w^2 |N_{eff}| \tag{3.35}$$

where w is the width of the detector. This is demonstrated in fig 3.5: in an initially n-type detector V_{FD} is decreasing with fluence, which could be interpreted as donor removal. On top of this process, acceptor like states are generated leading to type-inversion. By further increasing the fluence the N_{eff} grows and so does the full depletion voltage, until the point it gets so high to threaten with detector breakdown. A practical consequence of the type inversion is that the junction and the ohmic contacts switch sides[10] [60].

3. The introduction of energy levels deep in the gap increases carrier capture probability, decreasing their lifetime. This effect is described by

[10] E.g. in a p^+n detector the n-type bulk will change to p-type. The metal of the ohmic contact will then act as the donor, so the junction (the rectifying contact) will be formed on the other side of the detector. Nevertheless the detector will be able to operate at the same voltage polarity, because the p^+n order is preserved.

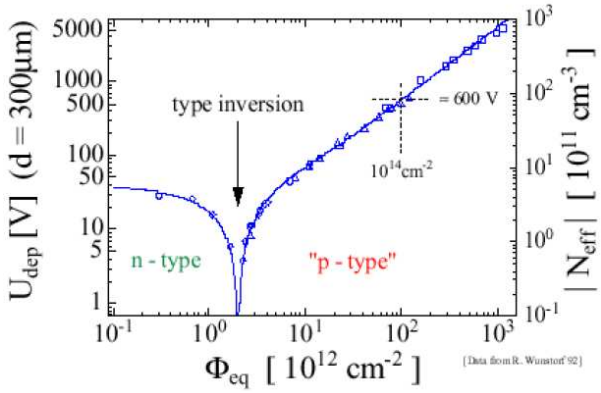

Figure 3.5: The effective doping concentration in standard silicon as a function of 1 MeV neutron fluence. From [69].

introducing the trapping time constant:

$$N = N_0 e^{-\frac{t}{\tau_{tr}}} \tag{3.36}$$

where according to [65], the inverse of the trapping time is proportional to the fluence:

$$\frac{1}{\tau_{tr}} = \frac{1}{\tau_{tr}^0} + \frac{\Phi}{K} \tag{3.37}$$

with the proportionality factor 1/K. If the captured carriers are released within the electronics' shaping time, the charge collection is not affected. However, if detrapping time is large compared to charge collection time or electronic shaping time, the charge collection is incomplete. The charge collection efficiency can be improved by increasing the bias voltage, which decreases the capture probability and by keeping the shaping time large enough to collect as many charges as possible.

The detectors described in this work are oriented to detecting low energy protons. Some experimental and theoretical values of κ for low energy protons, as well as the current-related damage constant α, are given in the table 3.1. It should be noted that these values were extracted under the condition of non-implantation, meaning the protons used for the test purposes traversed the detector without absorption. On the other hand the detectors used in the framework of this thesis were exposed to both traversing and stopping particles, therefore the comparison has to be taken with caution.

Particle	α (10^{-17} A/cm)	κ_α	$\kappa_\alpha/\kappa_{\text{theo}}$
1 MeV neutrons	4.56	1.0	1.0
7 MeV protons	17.2	3.8±0.1	0.514
8 MeV protons	13.2	2.9±0.1	0.492
9 MeV protons	13.3	2.9±0.1	0.569
10 MeV protons	9.9	2.2±0.1	0.489
24 GeV/c protons	2.54	0.56±0.01	0.903

Table 3.1: Hardness factors κ and current-related damage constant α extracted from the leakage current increase with the proton fluence, for traversing protons. From [68].

Time evolution of defects

The radiation changes the effective doping concentration according to [66]:

$$\Delta N_{eff}(\Phi_{eq}, t(T_a)) = N_{eff,0} - N_{eff}(\Phi_{eq}, t(T_a)) \tag{3.38}$$

where Φ_{eq} is the equivalent 1 MeV neutron fluence, $t(T_a)$ is the annealing time at temperature T_a and $N_{eff,0}$ is the initial value before irradiation. The experiments [64,66] show that the radiation induced defects can be classified according to their behavior in time as:

1. defects stable in time (N_C),
2. electrically active defects changing into non-active ones in the beneficial annealing process (N_a),
3. electrically non-active defects changing into active ones in the reverse annealing process (N_Y).

so the effective doping concentration can be written as:

$$\Delta N_{eff}(\Phi_{eq}, t(T_a)) = N_C(\Phi_{eq}) + N_a(\Phi_{eq}, t(T_a)) + N_Y(\Phi_{eq}, t(T_a)) \tag{3.39}$$

The time dependence of the effective doping concentration is shown in the figure 3.6.

The change of the leakage current can be described by the damage constant α defined by equation 3.34. This constant generally depends on the annealing time t and the temperature T_a:

$$\alpha(T_a, t) = \frac{\Delta I}{V \Phi_{eq}} \tag{3.40}$$

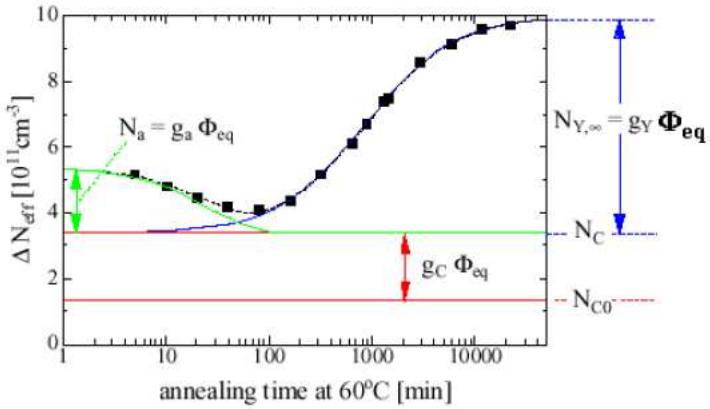

Figure 3.6: Annealing behavior of the radiation induced change in ΔN_{eff} after irradiation with 1.4×10^{13} cm^{-2} of 1 MeV neutrons. From [70].

According to [65, 67] it can be parametrized as:

$$\alpha(T_a, t) = \alpha_0 + \alpha_1 e^{-t/\tau_1(T_a)} - \alpha_2 ln(t/\tau_2(T_a)) \tag{3.41}$$

where the first term is related to the constant damage and the second and the third terms to the beneficial and the reverse annealing, respectively. When considering radiation-induced change in the leakage current it is necessary to do the comparison of the values at the same temperature. Therefore, the data are usually given for the room temperature $T_R = 20\ ^\circ C$, which can be scaled to any temperature T_a by means of the relation [71]:

$$\frac{I(T_R)}{I(T_a)} = \frac{\alpha(T_R)}{\alpha(T_a)} = \left(\frac{T_R}{T_a}\right)^2 exp\left(-\frac{E_g}{2k_B}\left[\frac{1}{T_R} - \frac{1}{T_a}\right]\right) \tag{3.42}$$

3.2 Layout

The Silicon Detector (SD) is a detector telescope consisting of seven layers of silicon diodes, one layer of plastic scintillator and an aluminum absorber (figures 3.7 and 3.8). The first of the seven silicon layers is a double-sided strip detector (BB2) used for measurement of horizontal and vertical angles. It has twenty-four vertical and horizontal strips and the total thickness of the detector is 0.3 mm. The next five layers are single area diodes (MSX) of 1 mm thickness each, used for energy deposition measurement. The last layer of silicon is a 0.3 mm thick detector used as a veto. A 3 mm thick plastic scintillator for timing purposes is placed in front of the first silicon layer

d [cm]	8	9	10	11
$\Delta\Omega$ [msr]	88	70	57	47

Table 3.2: Solid angle covered by the Silicon Detector for various distances from the target.

behind 1 mm aluminum absorber used for low-energy background reduction. The energy acceptance of the detector can be shifted up or down by increasing or decreasing the thickness of the aluminum absorber[11]. In the described configuration, the proton kinetic energy range is $25.2 - 40.6$ MeV.

The telescope subtends a solid angle up to 88 msr, depending on the distance from the target, which can be adjusted in 8 cm - 11 cm interval (table 3.2). The Detector is enclosed in an aluminum housing and attached to a motor (fig. 3.9). It enables the rotation of the detector around the target in the range of $65° - 153°$ (detector's central angle) on both sides of the beam. The detector and the supporting construction are placed inside the vacuum scattering chamber. A more detailed description of Detector's components, accompanying electronics and the supporting construction is given in the appendix A.

The detector layers are connected to charge-sensitive preamplifiers, placed outside the scattering chamber. The signals of the MSX detectors are digitized and recorded for each event in the form of oscillograms, using a 100 MHz flash ADC. An algorithm for oscillogram processing based on trapezoid-shaping [72–74] has been developed in the framework of this thesis. This algorithm adjusts the signal shaping time according to the rise-time of the preamplifier signals, which is important because the rise-times depend on the energies of impinging particles and they change additionally with radiation-induced detector damage. The method of signal digitization is described with examples in appendix B.1 and the details of the processing algorithm are given in appendix B.2.2. An important advantage of the digital signal processing, as opposed to classical analog signal shaping, is its great flexibility. The adjustments of the signal shaping time are important for finding the optimal balance between the required energy resolution and counting rates, especially at high particle fluxes the Silicon Detector is operated at. Drawbacks of this approach are a larger recorded data quantity which reaches 1 Gb/h, compared to 0.25 Gb/h with classical electronics and a more time consuming data analysis due to the time needed for algorithm optimization.

[11] The thickness of the aluminum absorber, on the other hand, influences the energy resolution and signal-to-background ratio. See section 3.3.1.

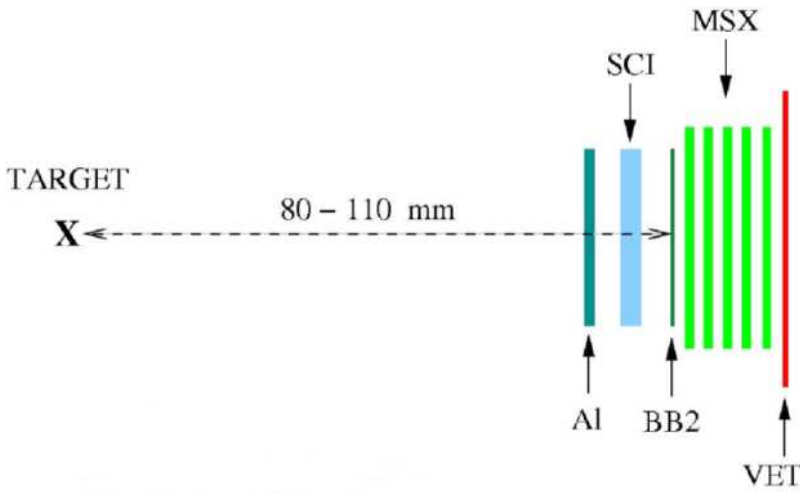

Figure 3.7: A schematic drawing of the Silicon Detector. The layers from left to right are: aluminum absorber (Al), plastic scintillator (SCI), double-sided strip detector (BB2), five single area detectors (MSX) and a veto detector.

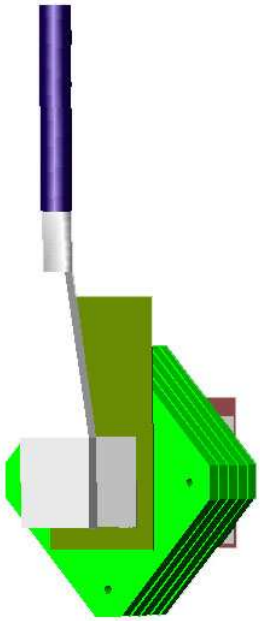

Figure 3.8: A sketch of the Silicon Detector. (Front view.)

Figure 3.9: The detector housing and the supporting construction with the rotation motor.

3.3 Specifications

The principal goal of the Silicon Detector is to detect low energy protons instead of one of the magnetic spectrometers in the measurements of the reactions with inherently low statistics. This is accomplished by detector's large angular acceptance, which is up to 3 times greater than the largest spectrometer acceptance. Of course, the detector has to fulfill minimal requirements concerning the angular and energy resolution and should retain these properties at high counting rates required by the experiments. Furthermore, the detector should maintain satisfactory properties after irradiation with high particle fluences.

3.3.1 Energy resolution

The energy resolution ΔE of silicon detectors is usually defined as the full-width-at-half-maximum (FWHM) of the most intensive line from ^{241}Am α-source (see table 3.4). Sometimes it is convenient to express the resolution as the standard deviation σ of the (Gaussian) α-peak. These two definitions are used equivalently and they are related by $\sigma = \Delta E/2.35$.

The following factors influence the precision of particle's energy reconstruction with the Silicon Detector:

1. intrinsic detector resolution
2. detector noise
3. electronic noise
4. energy straggling
5. vertex resolution
6. signal pile-up

where the first four are inherent and the last two are experiment-dependent factors. The next paragraphs examine the contribution of these factors to Silicon Detector's energy resolution.

Intrinsic detector resolution

The intrinsic energy resolution of a silicon detector is limited by the minimal energy w needed to create an e-h pair. This energy is $w = 3.6$ eV for silicon at room temperature [60]. The detectors considered in this work are 1 mm thick and the ^{241}Am α-particles are completely absorbed, therefore the intrinsic resolution can be obtained from relation 3.14. By inserting the energy of the α-particle $E_\alpha = 5.48$ MeV and Fano factor $F = 0.12$ from [58], we find that the intrinsic detector resolution is $\sigma_{intr} = 1.5$ keV.

Detector and electronic noise

The sources of detector noise are discussed in 3.1.2. Let us denote its standard deviation as σ_{leak}, because the main contribution comes from the leakage current. Also, let σ_{Electr} be the standard deviation of the electronic noise. These sources of noise, as well as the intrinsic resolution are independent, therefore they can be square-summed:

$$\sigma_{noise} = \sqrt{\sigma_{leak}^2 + \sigma_{Electr}^2} \tag{3.43}$$

Energy straggling

Energy straggling is caused by statistical variations in energy loss of particles passing through matter. In the case of thick absorbers, where the number of interactions is large, the distribution of these variations approaches a Gaussian [58] with the standard deviation given by Bohr's formula:

$$\sigma_0^2 = 4\pi N_A r_e^2 (m_e c^2)^2 \rho \frac{Z}{A} x = 0.1569 \rho \frac{Z}{A} x \ [MeV]^2 \tag{3.44}$$

where ρ is material density in g/cm^3, Z and A are proton and nucleon numbers, respectively and x is material thickness in centimeters. For relativistic particles the following correction can also be applied:

$$\sigma^2 = \frac{1 - 0.5\beta^2}{1 - \beta^2} \sigma_0^2 \tag{3.45}$$

The straggling in MSX detector's entrance window[12] is calculated according to the above equations, σ_W=4.5 keV which can practically be neglected. A much larger contribution comes from the straggling in the layers of the telescope that are not used for energy measurement. They are: the aluminum absorber ($\sigma_{strag,Al}$), the scintillator[13] ($\sigma_{strag,Scint}$) and the strip detector ($\sigma_{strag,BB2}$).

Let us denote the total straggling contribution as σ_{strag}:

$$\sigma_{strag}^2(E) = \sigma_{strag,Al}^2(E) + \sigma_{strag,Scint}^2(E) + \sigma_{strag,BB2}^2(E) \tag{3.46}$$

it has a slight energy dependence due to relativistic factor from equation 3.45. An estimate of the energy straggling in the front layers (including the target) is given in table 3.3. It is calculated with equations 3.44 and 3.45 assuming the mean proton kinetic energy of 33 MeV.

[12] Window thickness is of order 1 μm, see 3.4.3.

[13] For the scintillator we take the effective thickness: scintillator + reflective foil + light insulation $\simeq$ 3.25 cm.

Layer	Thickness	σ
^{12}C Target	0.13 mm	42 keV
Aluminum	1.00 mm	145 keV
Scintillator	3.25 mm	161 keV
Strip-detector	0.30 mm	75 keV
Total	4.68 mm	233 keV

Table 3.3: The energy straggling in the front layers for protons with an initial kinetic energy of 33 MeV.

Vertex resolution

The vertex resolution of any of the detectors used in experiments mentioned in this work (spectrometers or the Silicon Detector) is $\geq$ 1 mm, which is much more than the thickness of the target. Hence, the precise position of the vertex within the target material is unknown. The proton energy loss in the target cannot be reconstructed exactly, therefore it is estimated assuming the vertex in the middle of the target. This brings an additional uncertainty in proton's energy. For ^{12}C target of 43.86 mg/cm^2 this uncertainty σ_{ver} is between 0.13 - 0.21 MeV depending on proton's energy in the energy range of the Silicon Detector (25-41 MeV) and the target angle to the detector[14].

Signal pile-up

Under typical experimental conditions the high flux of the incoming particles causes signal pile-up. This is not the pile-up in the classical sense of having the rising edge of the second signal upon the tail of the preceding signal, because that case can be handled well by means of the trapezoid shaping technique (see appendix B). The pile-up here is reflected in signal base line fluctuations, caused by quasi-continuous low-energy background. These fluctuations primarily depend on particle flux, but also on signal processing conditions such as the shaping time. The base line fluctuations introduce additional uncertainty $\sigma_{BL,i}$ in proton energy. They are smaller for each successive layer (i), because the counting rates decrease due to absorption in preceding layers. Nevertheless, these contributions can be as large as $\sigma_{BL,i} = 0.5\ MeV$, which means they are by far the biggest source of energy measurement error.

[14]The uncertainty in the target energy loss is obtainted by subtracting the energy loss of protons coming out from the target middle and the target edge. For possible combinations of target angles and proton energies the range of 0.13 - 0.21 MeV is obtained.

MSX detector	σ_{MSX}	σ_{intr}	σ_W	σ_{noise}
new	11.9 keV	1.5 keV	4.5 keV	10.9 keV
irradiated	51.1 keV	1.5 keV	4.5 keV	50.1 keV

Table 3.4: The energy resolution of a new and an irradiated MSX detector.

Single layer resolution

The energy resolution of a single silicon layer σ_{MSX} was measured in laboratory using the ^{241}Am α-source. It contains the following three contributions:

$$\sigma^2_{MSX} = \sigma^2_{intr} + \sigma^2_{noise} + \sigma^2_W \tag{3.47}$$

The measurement is described in the section 3.4.4 and the results are summarized in the table 3.4. σ_{noise} is deduced from the measured value of σ_{MSX} and the calculated values of σ_{intr} and σ_W. This is obviously the largest contribution to the energy smearing, while the straggling contribution and the intrinsic resolution have smaller influence. This is especially the case for irradiated detectors, where the growth of the leakage current leads to further noise increase.

Telescope resolution

To obtain the energy resolution of the whole telescope we have to take into account all the factors that influence the precision of energy measurement. The total energy spread for protons, measured by the Silicon Detector is given by:

$$\sigma^2_E = \sigma^2_{strag}(E) + \sigma^2_{ver}(E) + \sum_{i=1}^{n(E)} (\sigma^2_{MSX,i} + \sigma^2_{BL,i}) \tag{3.48}$$

where $n(E)$ is the number of the MSX layers traversed by the particle with an initial energy E. Let us make some simplifying assumptions: the first is that all the MSX layers have the same energy resolution. The second is that the target energy loss does not change in the energy range covered by a single MSX layer and the third is that the straggling contribution does not change with the energy (the non-relativistic case). The results are shown in the figure 3.10 for unirradiated and irradiated detectors[15]. These results are obtained according to relation 3.48, where the values of σ_{strag}, σ_{ver} and $\sigma_{MSX,i}$ are obtained in the preceding discussion. The base-line energy spread for each layer $\sigma_{BL,i}$ was taken from typical experimental data[16].

[15]Irradiated with $\Phi_{eq} \simeq 10^{11}\ cm^{-2}$.

[16]In this case, it was obtained from the reaction $^{12}C(e,e'p)^{11}B$, where the proton was detected by the Silicon Detector. The counting rate in the first layer was $\sim$ 500 kHz.

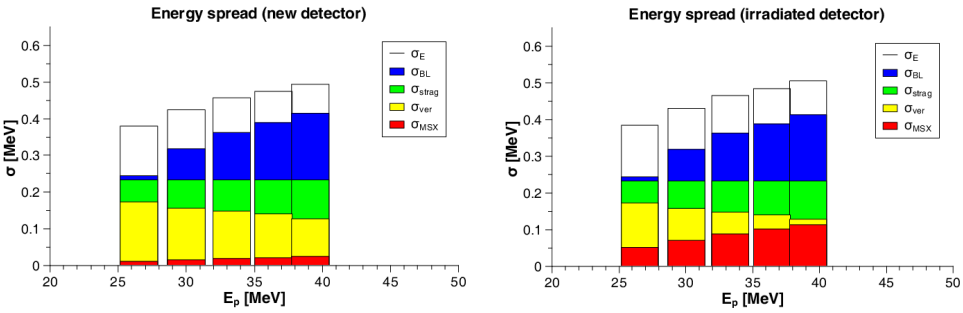

Figure 3.10: Energy resolution for protons in the Silicon Detector. The energy range is divided into five regions covered by the successive MSX layers. Note that the contributions are summed quadratically.

The figure 3.10 confirms that the largest contribution to the energy spread comes from base-line fluctuations due to high particle fluxes. It also shows that detector damage has a negligible influence on final energy resolution, which justifies the first simplifying assumption. Calculations also show that the second and the third assumptions do not change the result significantly, so realistic detector resolution should not deviate from this estimate by more than few per cent. The RMS detector resolution in this case is $\sigma_E \simeq 0.47$ MeV, which is equivalent to $\Delta E \simeq 1.10$ MeV (FWHM).

Theoretically, the best proton energy resolution can be achieved for $\sigma_{BL,i} = 0$, which is the case when counting rates become very small (< 100 Hz). Then, the mean energy spread is $\sigma_E \simeq 0.4$ MeV, which is equivalent to resolution $\Delta E \simeq 0.94$ MeV (FWHM).

3.3.2 Angular resolution

Angular resolution of the Silicon Detector is defined by two factors: the segmentation of the strip detector (BB2) and multiple scattering of particles in the layers preceding the strip detector.

Strip width

The horizontal and the vertical scattering angles (see figure 3.24) are:

$$\theta_{SD} = arctan\frac{k}{d} \tag{3.49}$$

$$\phi_{SD} = arctan\frac{l}{d} \tag{3.50}$$

where d is the distance from the target which can vary between 80 mm and 110 mm. The horizontal and the vertical distance of the strips[17] from the detector axis are denoted as k and l, respectively and they can both assume values from -12 mm to +12 mm. The uncertainties in determination of these distances are: $\Delta k = 1.0$ mm, $\Delta l = 1.0$ mm and $\Delta d = 0.5$ mm. The first two are simply the widths of the strips (1 mm) and the last one is the positional uncertainty limited by the precision of the mechanical components. Thus the angular resolutions of the horizontal and vertical strips are:

$$\Delta\theta_{strip} = \sqrt{\left(\frac{\partial\theta}{\partial k}\Delta k\right)^2 + \left(\frac{\partial\theta}{\partial d}\Delta d\right)^2} \tag{3.51}$$

$$\Delta\phi_{strip} = \sqrt{\left(\frac{\partial\phi}{\partial l}\Delta l\right)^2 + \left(\frac{\partial\phi}{\partial d}\Delta d\right)^2} \tag{3.52}$$

which becomes:

$$\Delta\theta_{strip} = \sqrt{\left(\frac{\Delta k}{d\left(1+\frac{k^2}{d^2}\right)}\right)^2 + \frac{k^2}{d^2}\left(\frac{\Delta d}{d\left(1+\frac{k^2}{d^2}\right)}\right)^2} \tag{3.53}$$

$$\Delta\phi_{strip} = \sqrt{\left(\frac{\Delta l}{d\left(1+\frac{l^2}{d^2}\right)}\right)^2 + \frac{l^2}{d^2}\left(\frac{\Delta d}{d\left(1+\frac{l^2}{d^2}\right)}\right)^2} \tag{3.54}$$

To evaluate the errors we put $d = 89\ mm$ which was the distance of the detector from the target during the beam-time in 2008. The equations 3.53 and 3.54 become:

$$\Delta\theta_{strip} \simeq \frac{\Delta k}{d\left(1+\frac{k^2}{d^2}\right)} \simeq 0.64^\circ \tag{3.55}$$

$$\Delta\phi_{strip} \simeq \frac{\Delta l}{d\left(1+\frac{l^2}{d^2}\right)} \simeq 0.64^\circ \tag{3.56}$$

Multiple scattering

The precision of the determination of particle's scattering angles is also influenced by multiple scattering in the target and the layers preceding the detector. The angular spread due to the multiple scattering was first theoretically described by Molière and later his model was modified by Bethe [75].

[17] More precisely, k and l are horizontal and vertical distances of the strip middle from detector's central axis.

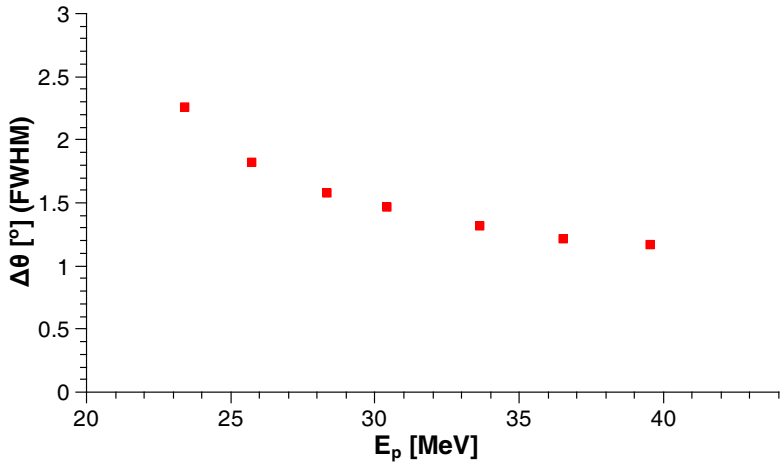

Figure 3.11: Measured angular resolution for protons in the Silicon Detector. The points represent the width of the Gaussian distribution measured at different proton energies.

For small scattering angles ($< 2°$) these models predict a Gaussian shaped distribution, with the width depending on particle's energy.

The total angular resolutions for protons measured by the Silicon Detector are given by:

$$\Delta\theta_p = \sqrt{\Delta\theta^2_{strip} + \Delta\theta^2_{scat}(E)} \tag{3.57}$$

$$\Delta\phi_p = \sqrt{\Delta\phi^2_{strip} + \Delta\phi^2_{scat}(E)} \tag{3.58}$$

These angular resolutions were measured in the reaction of elastic electron scattering off hydrogen $H(e, e'p)$, where the proton angles are uniquely defined by the electron angles and momentum (see section 3.5.2). By taking a narrow cut on the electron angle[18] $\Delta\theta_e = 0.2°$, we kinematically limit the range of proton angles to $\simeq 0.2°$. Therefore any measured angle spread greater than that value is the measure of the angular resolution. The results shown in the figure 3.11 suggest that angular resolution $\Delta\theta_p$ varies from 1.2° to 2.3° (FWHM) depending on the proton energy. The same is obtained for $\Delta\phi_p$.

[18] measured by a magnetic spectrometer with angular resolution $< 0.2°$.

Nuclide	E_α [MeV]	Intensity	$\bar{E}_\alpha$ [MeV]	$\bar{d}_{Si}$ [μm]
^{237}Np	4.788	47.6 %		
	4.771	23.2 %	4.78	22.4
	4.767	9.3 %		
^{239}Pu	5.157	70.8 %		
	5.144	17.1 %	5.15	24.9
	5.106	11.9 %		
^{241}Am	5.486	84.5 %		
	5.443	13.0 %	5.48	27.3
	5.388	1.6 %		
^{244}Cm	5.805	76.4 %		
	5.763	23.6 %	5.80	29.7

Table 3.5: Mean energies $\bar{E}_\alpha$ of the α-particles from Np/Am/Cm and Pt/Am/Cm mixed sources [77] and their mean range in silicon $\bar{d}_{Si}$ [78].

3.4 Tests

MSX detectors were tested in series of laboratory measurements. The standard electronics to perform these measurements included MSI-8 preamplifier/shaper (see appendix A.2.2), MHV-4 voltage supply (see appendix A.2.4), a multichannel analyzer [76] and a digital oscilloscope. If not specified otherwise, it is supposed throughout this section that the standard electronics were used. The temperature was monitored by means of a thermometer. Two mixed alpha sources were used in the test measurements: Np/Am/Cm and Pt/Am/Cm, with energies given in table 3.4.

In order to determine the influence of the high-particle-flux environment on detectors' performance, they were tested before and after the irradiation.

3.4.1 Signal properties

Leakage current

The dependence of the leakage current on the bias voltage was measured and read out with the MHV-4 unit. The detector bias voltage was corrected for the voltage drop on the preamplifier bias resistor (R = 5 MΩ) according to:

$$U_{bias} = U_{HV} - I_{leak}R \tag{3.59}$$

The leakage currents were normalized to 20 °C according to relation 3.42. The detectors were tested before irradiation ($\Phi_{eq} = 0$) and after irradiation with $\Phi_{eq} \simeq 10^{10}\ cm^{-2}$ and $\Phi_{eq} \simeq 10^{11}\ cm^{-2}$. The obtained I-V plots are shown in the figure 3.12. The increase of the leakage current with particle

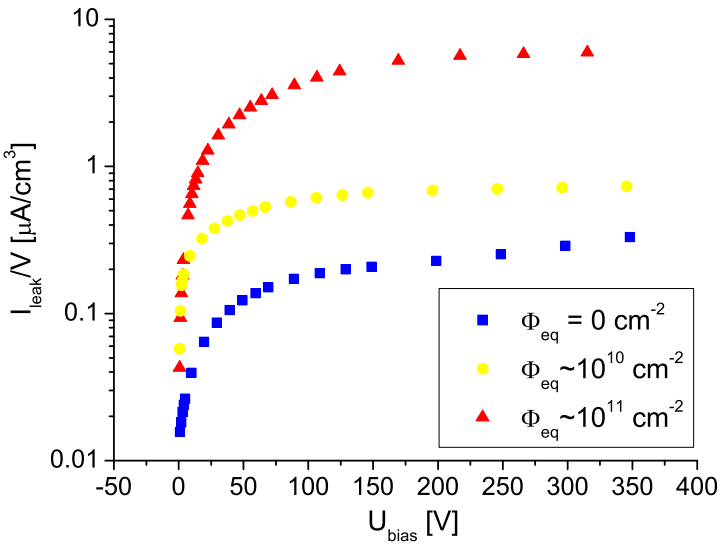

Figure 3.12: Leakage current versus bias voltage of an unirradiated MSX detector and two irradiated detectors. The currents are normalized to 20 °C.

fluence is obvious. This is expected from relation 3.34 and it is in agreement with the results from [66–68] shown in the figure 3.4.

To test the influence of the guard ring connection on the leakage current, the measurements were repeated with a floating, grounded and biased guard ring of the detector, for both irradiated and unirradiated detectors. No significant difference in the leakage current was observed.

Signal rise time

The rise time t_R of the preamplifier signal was measured on a digital oscilloscope for different bias voltages. The measurement was made in vacuum (10^{-2} mbar), with Np/Am/Cm α-source. The range of the particles in silicon is 23 - 30 μm, compared to the total thickness of the detector which is 1000 μm.

The results are displayed in the figure 3.13. They show that the signals of the particles detected close to the junction (front) have a shorter rise time than the ones detected near the ohmic (back) side of the detector, measured at the same bias voltage. This is in a good agreement with the theory of the pulse shape discussed in section 3.1.2. The signals near the junction contact are mainly induced by electron movement in the electric field which

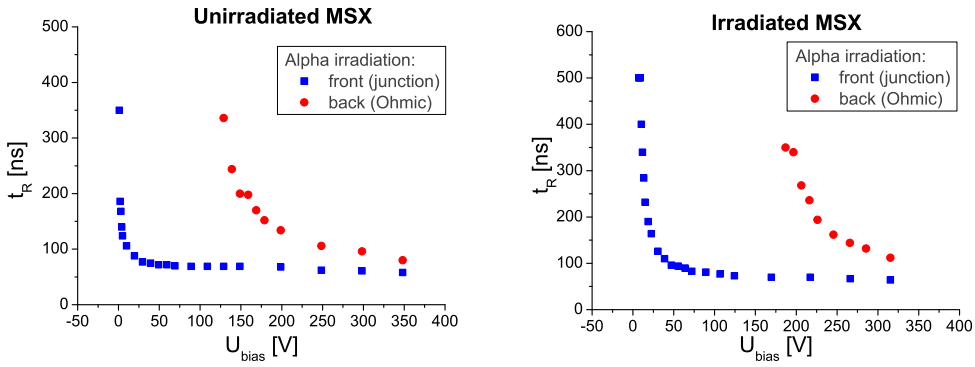

Figure 3.13: Rise time of the preamplifier signal for an unirradiated (left) and an irradiated detector (right).

was demonstrated in the figure 3.3. On the other hand, the signals produced near the ohmic contact are mainly induced by movements of holes. For relatively weak electric fields ($E < 10^3\ V/cm$) the electron mobility in silicon is 1350 cm^2/Vs compared to holes' 480 cm^2/Vs, so the front-side signals are expectedly faster (i.e. they have a shorter rise-time). The rise times of the signals are longer in the case of radiation-damaged detectors, measured at the same bias voltage. This can be expected according to the discussion in the section 3.1.3. The radiation damage reduces the charge collection efficiency, the charge collection is slower and the signals have longer rise times.

The results in the figure 3.13 also show the importance of overdepleting the detector for faster charge collection. For bias voltage of 1.33 V_{FD} the signal rise times are $\sim 2/3$ and for 1.66 V_{FD} the rise times are $\sim 1/2$ of their values at full depletion.

3.4.2 Energy response

The energy response of the MSX detectors was measured with the standard electronics: the preamplifier signals were Gaussian shaped by a shaping amplifier with 1 μs shaping time. The signal height was measured by a multichannel analyzer [76].

Bias voltage

Figure 3.14 shows dependence of the energy response on the bias voltage, for alpha particles detected on the front (junction) side and the back (ohmic)

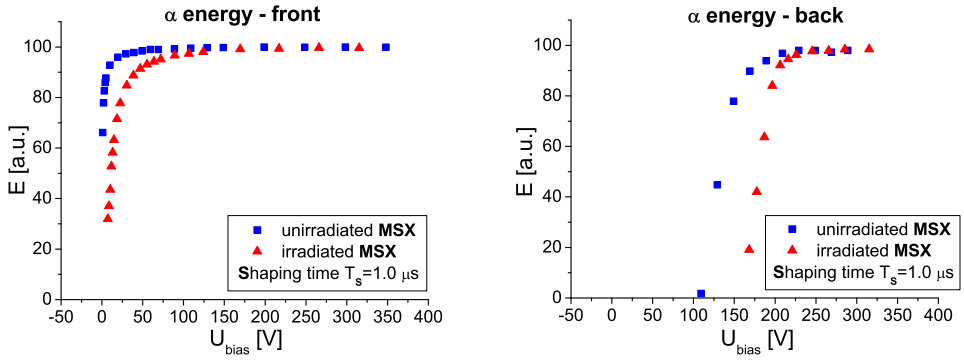

Figure 3.14: Energy response of a new and an irradiated MSX detector. Left: α-particles incoming on the front (junction) side of the detector. Right: α-particles incoming on the back (ohmic) side of the detector.

side of the detector[19]. In the case of the front irradiation the signal reaches its full height at very low voltages. In the case of the back side irradiation the signals reach the full height at much higher voltages. This is expected from the discussion in 3.1.1, because the depletion zone spreads from the junction towards the ohmic contact by increasing the bias voltage. The detector is fully depleted when the depletion zone reaches the back contact, i.e. when the back side signal reaches its full height. The measured voltage of full depletion is $U_{FD} \simeq 180\ V$.

The measurement of the energy response of the unirradiated MSX detector can be used to estimate the initial effective doping concentration $N_{eff,0}$. By inserting the value of the full depletion voltage U_{FD}=180 V into equation 3.8 we obtain $N_{eff} = 2.4\,10^{11}\ cm^{-3}$. According to equation 3.9, the resistivity of the silicon material is $\rho \simeq 20000\ \Omega$cm. This value of the doping concentration was used to calculate the charge collection functions plotted in the figure 3.3.

The results also show that the energy response of the irradiated detector is lower for the same applied voltage, which can be explained by a decreased charge collection efficiency. This is additionally confirmed by looking at the signal rise times of the irradiated detector which are longer than in the case of a new MSX.

[19]For the front side irradiation the alpha source was in vacuum ($E_\alpha = 5.48\ MeV$, range in silicon $d_\alpha = 26\ \mu m$). For the back side the alpha source was in air ($E_\alpha = 2.88\ MeV$, range in silicon $d_\alpha = 10\ \mu m$).

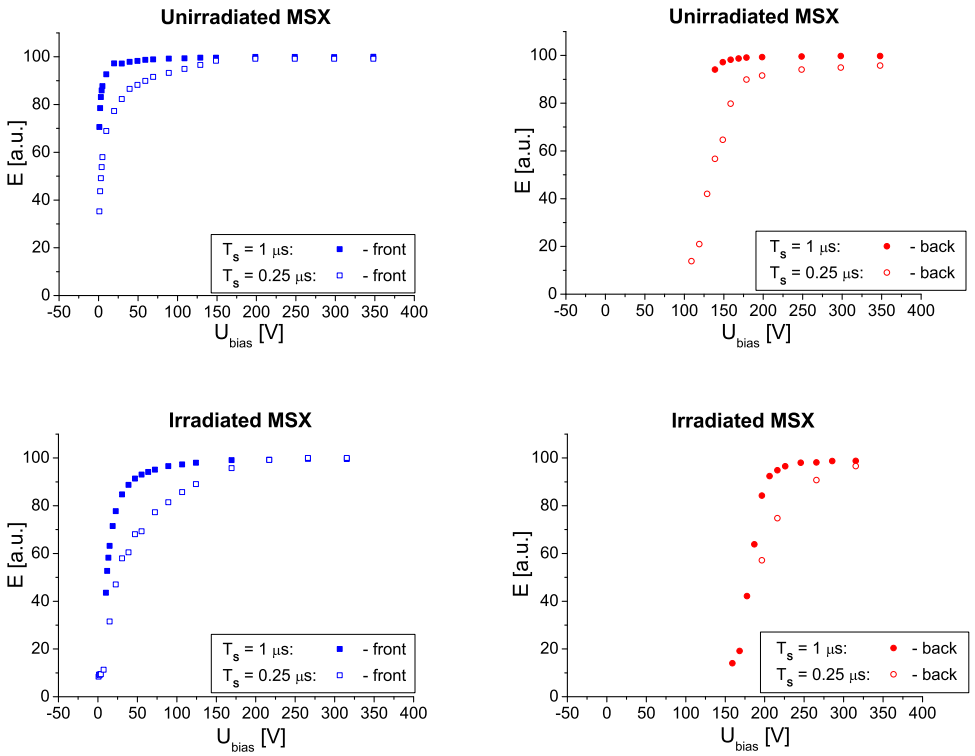

Figure 3.15: Influence of the MSI-8 module shaping time on the energy response. Upper panels: unirradiated MSX detector. Lower panels: irradiated MSX detector. The results are obtained for α-particles incoming on the front side (left) and the back side (right).

Shaping time

The influence of the amplifier shaping time on energy response was tested with the MSI-8 module (see appendix A.2.2). The results are shown in the figure 3.15. Shorter shaping times result in lower energy response due to incomplete charge collection, which is even more obvious for irradiated detectors where the signals are slower (longer rise times).

3.4.3 Window thickness

Though the detectors are fully depleted they inevitably have an insensitive layer at their front and the back surfaces. These layers (windows) are usually made of evaporated metal and their purpose is to ensure the proper contact between the semiconductor material and the bias supply. The thickness of

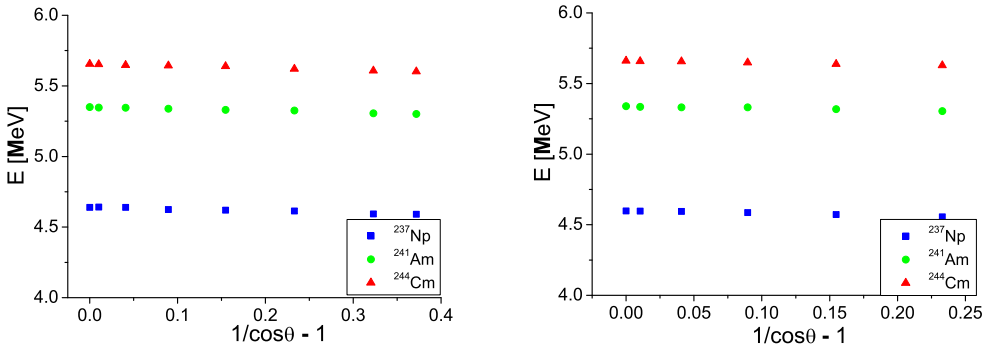

Figure 3.16: Energy vs. angle, obtained with the Np/Am/Cm α-source. Left: entrance window (front). Right: exit window (back).

the entrance (front) and exit (back) windows was determined by varying the angle of the incoming α particles, as suggested in [60].

First, let us make two simplifying assumptions:

- The thickness of the entrance and the exit windows t is expressed as silicon-equivalent thickness, i.e. a thickness of silicon that causes the same energy loss as the actual material.
- The specific energy loss of dE_0/dx can be taken constant for the layers of the thicknesses considered ($\simeq 1\ \mu m$).

For a particle entering the detector perpendicularly with an energy E_0, the energy loss in the window is:

$$\Delta E_0 = \frac{dE_0}{dx} t \tag{3.60}$$

where t is the thickness of the window. If the particle enters the detector at an angle θ to the normal, the energy loss in the window becomes:

$$\Delta E(\theta) = \frac{\Delta E_0}{cos\theta} \tag{3.61}$$

The difference of the deposited energy for these two cases is:

$$E' = (E_0 - \Delta E_0) - (E_0 - \Delta E(\theta)) \tag{3.62}$$

Combining the equations 3.60 to 3.62, we obtain:

$$E' = \Delta E_0 \left(\frac{1}{cos\theta} - 1 \right) \tag{3.63}$$

Source	E_0 $[MeV]$	t_{front} $[\mu m]$	t_{back} $[\mu m]$
^{237}Np	4.78	0.94 ± 0.07	1.21 ± 0.08
^{241}Am	5.48	0.93 ± 0.06	1.03 ± 0.12
^{244}Cm	5.80	1.10 ± 0.06	1.05 ± 0.04
	mean thickness	0.99 ± 0.04	1.08 ± 0.03

Table 3.6: The thickness of the entrance (front) and exit windows (back) of MSX detectors, obtained for different α energies.

By measuring E' as a function of θ the energy loss ΔE_0 in the window can be determined. The results of the measurement are shown in the figure 3.16.

To determine the window thickness an iterative procedure has to be adopted, because the absolute energy calibration of the detector is not precisely known (due to the unknown thickness of the entrance window). The procedure is as follows:

1. Initially $\Delta E_0 = 0$ is assumed. A linear fit made to the data points according to equation 3.63 gives the ΔE_0 as the slope. The thickness is calculated from equation 3.60 assuming $\frac{dE_0}{dx}(E_0)$.
2. - The calculation of energy loss is corrected by: $\frac{dE_0}{dx}(E_0) \longrightarrow \frac{dE_0}{dx}(E_0 - \frac{\Delta E_0}{2})$
   - The measured energies are corrected by: $E \longrightarrow E - \Delta E_0$

   The fit is repeated and the new value of ΔE_0 is obtained.
3. Step 2 is repeated if necessary.

The obtained thicknesses are close to 1 μm. The results are summarized in the table 3.6.

3.4.4 Energy resolution

To measure the resolution the spectrum of the mixed α-source Np/Am/Cm was recorded with a new and a radiation-damaged detector. Instead of using the shaping amplifiers, the preamplifier signals were digitized with the CAEN N1728 flash ADC [79] with 2.5 μs shaping time for the new detector and 3.6 μs shaping time for the irradiated detector. The spectra are shown in the figure 3.17. The measured resolutions[20] are ΔE = 28 keV for the new and ΔE = 120 keV for the irradiated detector. The resolution deterioration due to the radiation damage is obvious.

[20]Defined as FWHM of the most intensive ^{241}Am α-line.

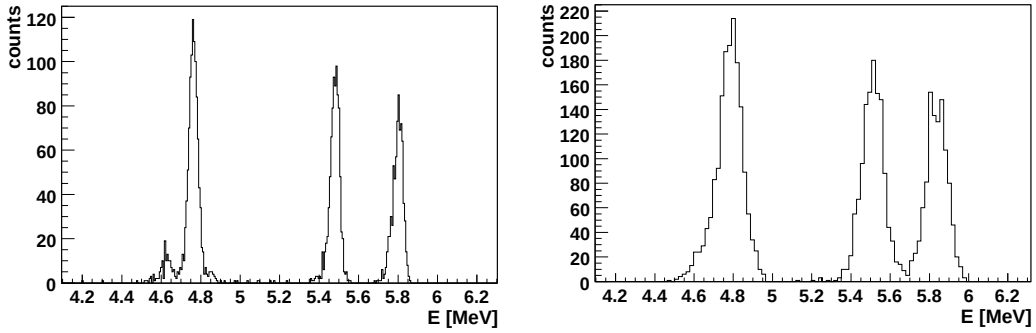

Figure 3.17: The spectrum of the Np/Am/Cm source measured with a new detector (left) and an irradiated detector (right).

Depletion

In order to test the depletion and the linearity of the energy response of the MSX detectors, an additional test with α-particles in air was performed. The α-particles interact with air atoms and lose energy. Therefore, by increasing the distance of the source from the detector d_{air}, we obtained α-particles of lower energies impinging on the detector. The lower their energy, the shorter the range in silicon d_{Si}, which enables testing detector energy response just a few microns from the detector surface (see table 3.7). In this way one can determine if the detector is depleted throughout its full volume.

The energies of the α-particles were measured at the front and the back side of the detectors. This is plotted against the energies of α-particles after traversing the particular pathlength in air d_{air}, calculated with Bethe-Bloch formula. The measured energies were additionally corrected for the loss in the entrance/exit window of 1 μm. The results are shown in figure 3.18. The good agreement of the measured and calculated energies shows the detectors can be fully depleted on the front and the back side. Should they not be fully depleted, significant deviations from the linearity of the energy response would be noted.

d_{air} [cm]	E' [MeV]	d_{Si} [μm]
1.0	4.56	20.9
1.5	4.06	17.8
2.0	3.50	14.5
2.5	2.88	11.3
3.0	2.15	7.9
3.5	1.24	4.3

Table 3.7: Energies of ^{241}Am α-particles E', after traversing the air distance d_{air} and their range in silicon d_{Si}. The initial α-energy is 5.48 MeV.

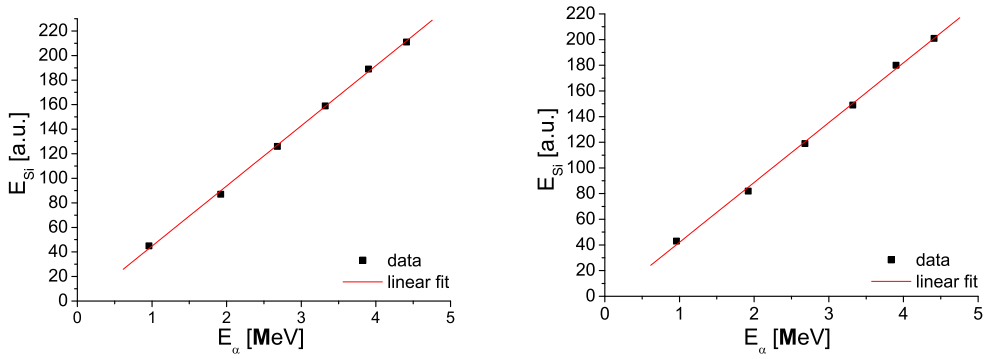

Figure 3.18: Measured vs. calculated α-energies for front (left) and back (right) irradiation. The line is a linear fit.

3.4.5 Radiation damage

The irradiation of a detector produces damage which leads to the increase of the leakage current. This is predicted by theory and expressed in equation 3.34. Such behavior is also observed for the MSX detectors during radiation exposure (figure 3.19). Linear increase of the leakage current was noticed, depending on the detector count rate.

Radiation hardness factor κ, defined by relation 3.33, depends on the type and the energy of the incoming particles. In order to estimate κ the particle flux Φ and equivalent 1 MeV neutron flux Φ_{eq} must be known. The former can be estimated from the experimental data, e.g. trigger counter. The latter is determined from the increase of the leakage current according to relation:

$$\frac{\Delta I}{V} = \alpha_{(1\,MeV\,n)}\Phi_{eq} \tag{3.64}$$

where $\alpha_{(1\,MeV\,n)} = 4.56\,10^{-11}$ μA/cm [68].

The estimated hardness factors for MSX detectors, given in the table 3.8, show that $\kappa \simeq 3$. They are effective hardness factors, meaning that the damage caused by all the incoming radiation (protons, deuterons, neutrons, pions, etc.) is about 3 times larger than the damage that would be caused by the same number of 1 MeV neutrons. The mean energy deposition in each layer is 5 MeV and about 20 % of the particles per layer are stopped (implanted).

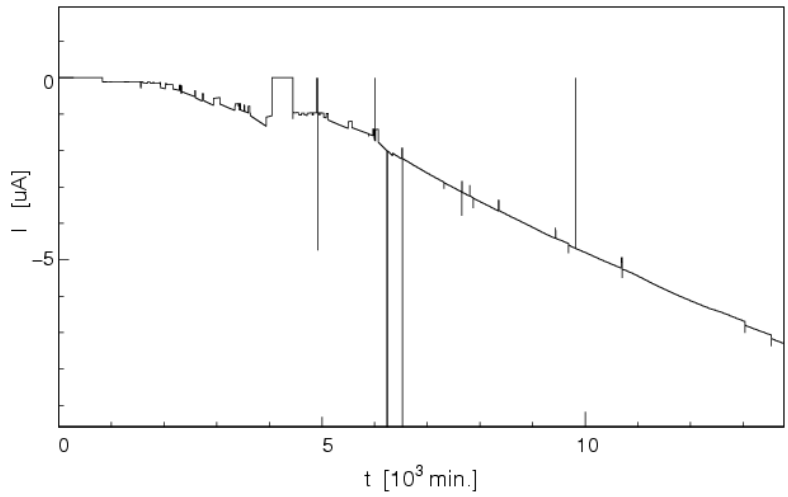

Figure 3.19: Increase of the detector leakage current during beam-time. Variations of the slope are due to changes of the counting rate. Vertical spikes are readout errors.

Detector	Hardness factor κ
MSX1	3.0 ± 1.5
MSX2	3.1 ± 1.6
MSX3	3.1 ± 1.6
MSX4	3.5 ± 1.7
MSX5	2.9 ± 1.4

Table 3.8: Radiation hardness factors for MSX detectors.

3.5 Calibration

3.5.1 Energy

The energy calibration of the Silicon Detector is done for each detector layer or strip separately. The detector properties are slowly changing during the beam-time due to radiation damage and the calibration needs to be readjusted. As demonstrated in the figure 3.19, the radiation damage causes the increase of the leakage current. Higher leakage current increases the voltage drop on the preamplifier bias resistor according to equation 3.59. Consequently, the effective detector bias voltage is decreased influencing the signal rise time and energy response as shown in figures 3.13 and 3.14. The voltage drop can be compensated by increasing the nominal bias voltage. Anyhow, the energy scale is changing during the beam-time and one has to make sure to take relatively short time windows in which the calibration remains

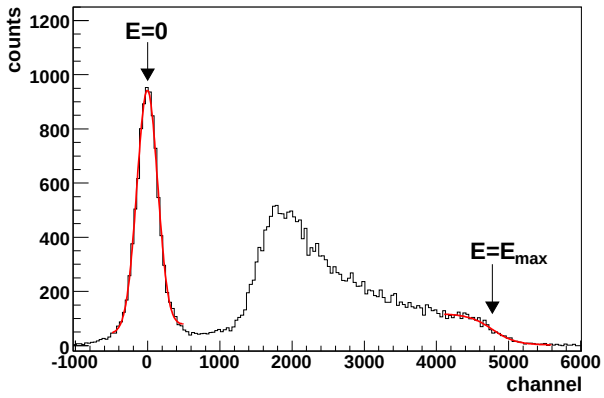

Figure 3.20: Energy calibration of a detector layer. The histogram shows a raw energy spectrum of the MSX2 detector. The arrows denote the position of the points taken for the energy calibration.

constant.

We have chosen to make the energy calibration for every data run, which usually takes one hour. To avoid interruptions in the data taking process, the calibration is made offline with the data itself. The energy response of the detectors is linear, therefore the energy calibration can be done by taking only two points. This is demonstrated in the figure 3.20, which shows a typical raw-energy spectrum obtained from an ADC. This spectrum contains a Gaussian-shaped peak around zero, which we call the base-line peak because it corresponds to events where no particle has entered the detector and only signal base-line fluctuations are recorded. The mean of this Gaussian should be at to E=0 and that is the first calibration point. On the high-energy side of the spectrum is a shoulder, that corresponds to the maximum deposited energy. It is determined by the thickness of the material and particle type, as shown in table 3.9. The second calibration point is determined by making a Fermi-Dirac-like fit[21] to this high-energy shoulder. The half-height of the fitted function should correspond to the maximum deposited energy.

3.5.2 Central angle

The horizontal (θ) and the vertical (ϕ) scattering angles of the particle are measured with the double-sided strip detector described in A.1.1. The angles can be determined from the geometry: distance of the detector from the target and the position of the strip with respect to the detector central axis

[21] The fitted function is $f(x) = \frac{c_1}{e^{c_2 x - c_3} + 1} + c_4$, the half-height corresponds to $\frac{c_3}{c_2}$.

Layer	Thickness	E_{max}
BB2	300 μm	6.10 MeV
MSX	1003 μm	12.26 MeV
VETO	300 μm	6.10 MeV

Table 3.9: Maximum energy deposition of protons in silicon layers. Values obtained from the simulation.

(see 3.24). The angle of the detector central axis to the beam is referred to as the central angle of the detector.

The central angle is calibrated in the reaction of elastic electron scattering on protons $H(e, e'p)$. The scattered electron was detected by one of the magnetic spectrometers and the proton by the Silicon Detector, as depicted in the figure 3.21. This reaction is overdetermined, meaning the proton four-momentum is completely determined by electron four-momentum and energy and momentum conservation. Thus the proton scattering angles are given by relations 3.65 and 3.66.

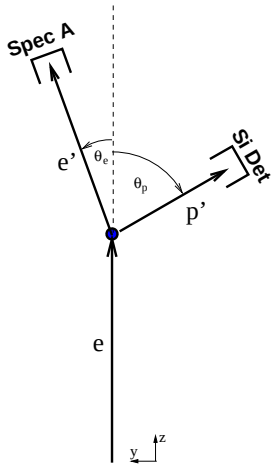

Figure 3.21: $H(e, e'p)$ reaction.

Conservation of momentum in the laboratory system is:

$$0 = p'_e sin\theta_e cos\phi_e - p'_p sin\theta_p cos\phi_p \quad (\hat{x})$$
$$0 = p'_e sin\theta_e sin\phi_e - p'_p sin\theta_p sin\phi_p \quad (\hat{y})$$
$$p_e = p'_e cos\phi_e + p'_p cos\phi_p \quad (\hat{z})$$

for the scattered proton it follows:

$$\theta_p = acos\left(\frac{p_e - p'_e cos\theta_e}{p'_p}\right) \qquad (3.65)$$

$$\phi_p = asin\left(\frac{p'_e sin\theta_e sin\phi_e}{p'_p sin\theta_p}\right) \qquad (3.66)$$

The elastic scattering on protons provides a precise calibration, but only in the relatively narrow forward region $\theta_p = 65° - 90°$. The lower limit of 65° is set by Silicon Detector, while the 90°-limit is set by momentum conservation, as the outgoing protons fly forward. However, the detector covers the angular range up to 153° with respect to the beam, therefore calibration in the backward region ($\theta_p > 90°$) is needed. This is done by measuring the position of the detector housing with respect to the beam by means of a theodolite. The complete results of calibration of the central angle

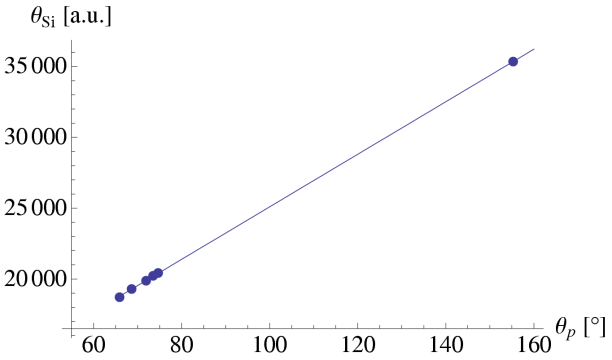

Figure 3.22: Calibration of the Silicon Detector central angle. Five calibration points are taken for forward angles ($\theta_p < 90°$) and one for backward angle ($\theta_p > 90°$). The line is a linear fit to the values read out by the potentiometer.

are shown in figure 3.22. Once the central angle is calibrated, the angular position can be read out at any moment via potentiometer.

3.6 Trigger

This section describes how the Silicon Detector generates the trigger. The first triggering condition is determined by the scintillator: if the signal is greater than the threshold set on the discriminator, the event is accepted. For the Silicon Detector working in the single-arm mode, this is also the only condition. In this case the particles which deposit less energy than the threshold, meaning very slow or very fast particles, are cut off. The selected threshold is set low enough not to affect detector's energy acceptance.

In double and triple coincidence experiments, the Silicon Detector is working in pre-coincidence with spectrometer A (see figure 3.23). In this case, the second triggering condition is that the event must be seen by the scintillators of the spectrometer A and Silicon Detector's scintillator. This condition is used to suppress the event rates to the limits acceptable by the data acquisition system, but it does not affect the final results of the analysis, because double or triple coincidence cuts are imposed later anyway.

Figure 3.23 shows the electronics scheme and the trigger logic for the Silicon Detector. The the signal flow can be described by the following:

- A particle produces a signal in the scintillator.
- If the signal is greater than the threshold, the discriminator produces a logic 1.

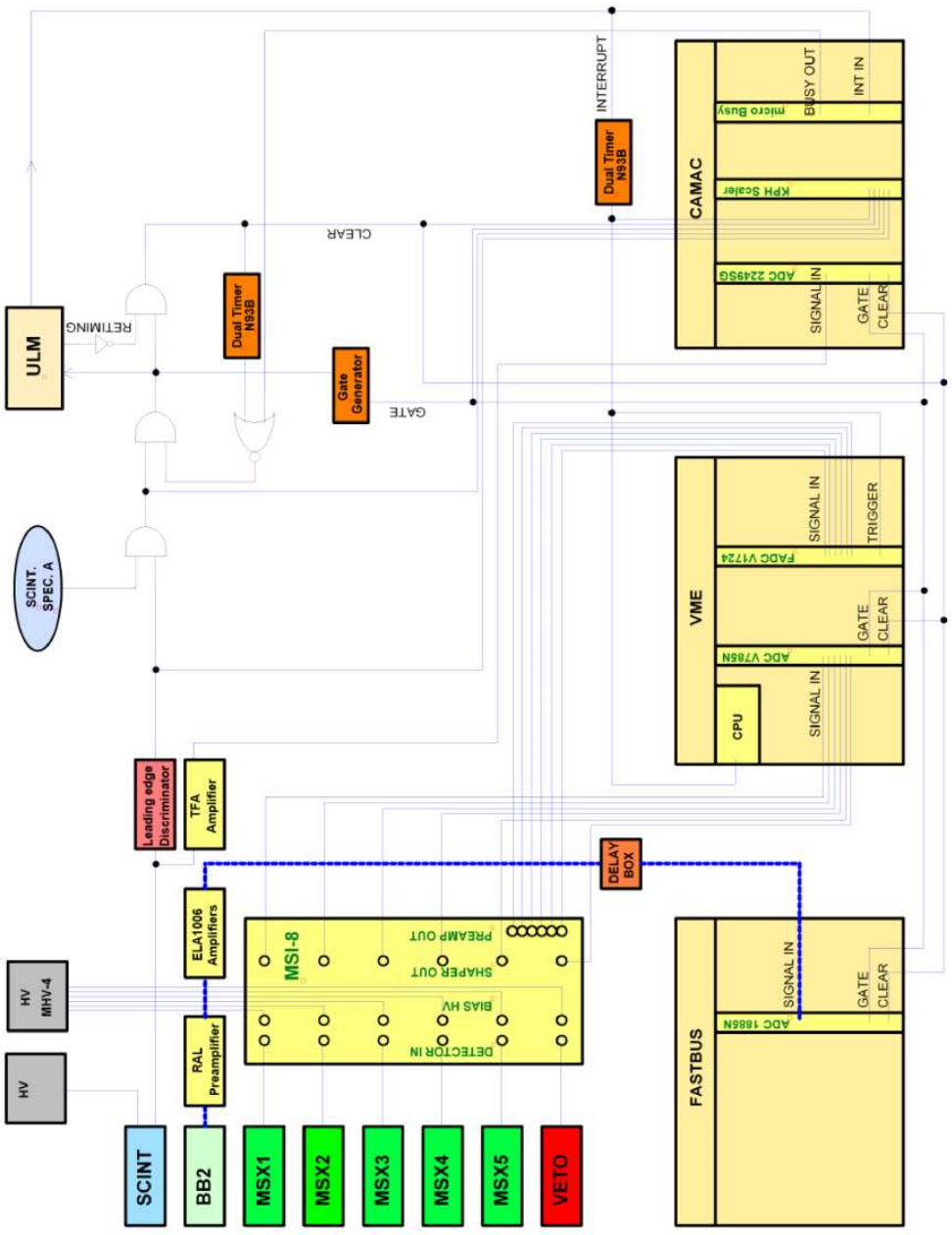

Figure 3.23: Silicon Detector electronics and trigger logic.

- This signal forms coincidence AND_1 with spectrometer A's scintillator signals.
- The coincidence output is inserted into AND_2 with BUSY signal from the μ-busy logic. If the electronics is available for acquisition the BUSY signal is 0 and a logic 1 is produced, in other case the BUSY signal blocks further acquisition.
- AND_2 is used:
  1. to form the GATE signal and start the ADC conversion,
  2. to send the event information to Universal Logic Module (ULM).
- The ULM can be programmed to accept or reject the event based on the information from all the detectors in the measurement:
  1. event accepted - the logic RETIMING and INTERRUPT signals are set to 1,
  2. event rejected - the logic RETIMING and INTERRUPT signals are set to 0.
- If the event is accepted by ULM, the INTERRUPT waits for ADCs to finish the conversion after which they are read out.
- If the event is rejected by ULM, AND_3 output produces a logic 1 and a CLEAR signal is issued. This stops ADC conversion and clears their registers without read-out.

3.7 Event reconstruction

3.7.1 Angle

The double-sided strip detector (BB2) with 24 vertical and 24 horizontal strips is used for measurements of particle scattering angles. According to Silicon Detector's geometry, in >99% of the events the particle passes through only one horizontal and one vertical strip[22]. When the trigger is given, all strips are read out. To determine which strip has actually been hit, the algorithm looks for the strip with the highest energy deposition. There should be only one strip that has got significantly higher energy than the others which only contribute with pedestals and noise. This is shown in figure 3.25. Cross talk between the strips is negligible.

The position of the strip detector (BB2) with respect to the beam and the target is shown in figure 3.24. The particle scattering angles are determined

[22]In <1% of events, the particle can be on the border of two strips, leaving signals in both. This is also confirmed by simulation.

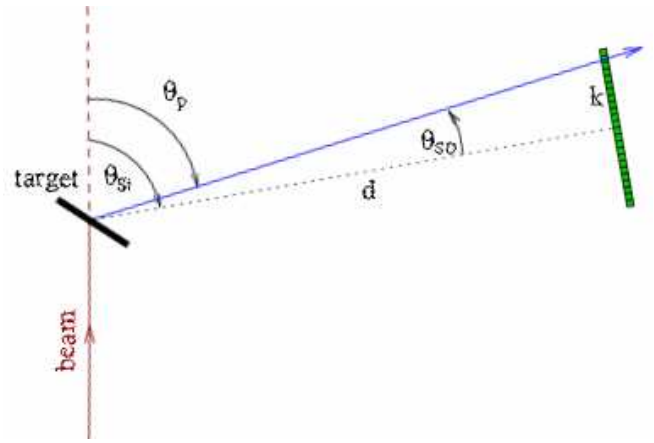

Figure 3.24: Position of the double-sided strip detector (BB2) with respect to the target and the beam. Detector's central angle is denoted by θ_{Si}, particle horizontal scattering angle relative to detector's central axis is θ_{SD} and k is the position of the strip in detector's coordinates.

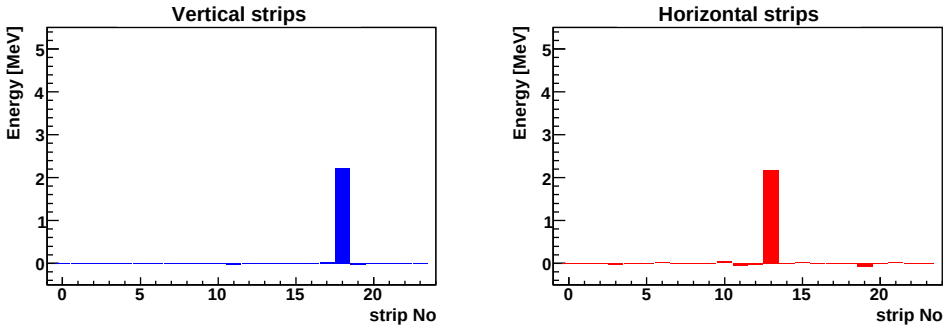

Figure 3.25: Energy deposition in vertical strips (left) and horizontal strips (right) for one event. Strips that are hit measure significantly larger energy.

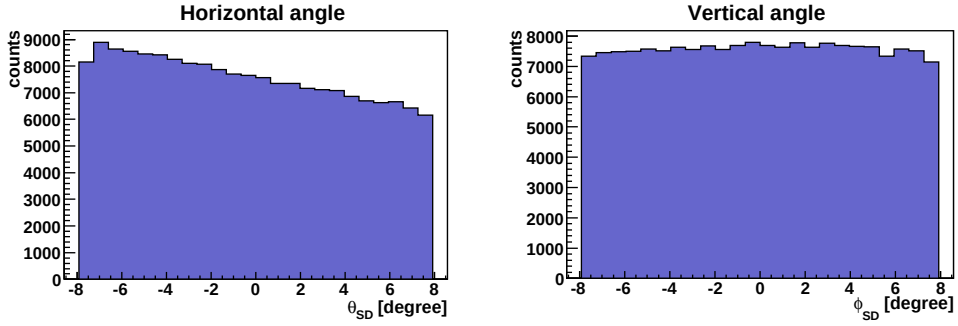

Figure 3.26: Horizontal angle θ_{SD} and vertical angle ϕ_{SD} of detected protons, with respect to Silicon Detector's central axis.

according to:

$$\theta_{SD} = \arctan\left(\frac{k}{d}\right) \tag{3.67}$$

$$\phi_{SD} = \arctan\left(\frac{l}{d}\right) \tag{3.68}$$

where d is the distance from the target, k the horizontal and l the vertical position of the strip with respect to the central axis. The reconstructed angles in Detector's coordinates (θ_{SD}, ϕ_{SD}) are shown in the figure 3.26 for the case of protons detected in quasi-elastic knock-out[23].

3.7.2 Energy

Energy deposition is measured in five MSX layers following the strip detector, while the sixth layer is used as veto. The layers are calibrated according to procedure described in 3.5.1. Figure 3.27 shows an example of the measured energy deposition during one event.

Typical energy spectra of the detector layers collected during multiple runs are shown in the figure 3.28. The peaks at zero energy are the so-called base-line peaks. They are obtained when the trigger gate is opened and no particle has entered the detector in which case only the base-line fluctuations contribute to the signal. The width of this peak gives a good measure of the resolution of the layer in question. The shapes of the energy spectra shown in the figure 3.28 can be better understood by looking at two-dimensional plots in the figure 3.29. They show energy deposition in two successive layers, where the front one is displayed in the vertical axis and the back one in the horizontal axis. The energy deposition exhibits a typical $\Delta E - E$ behavior: the particles that have traversed the front layer and are absorbed by the back layer are placed in the upper line of the plot. The larger their total energy the more energy they deposit in the back an the less in the front layer. On the other hand the particles that go through both layers are placed in the lower line of the plot, and their overall energy deposition decreases with larger initial energy. The base-line peaks can be distinguished as the ones lying at zero energy. The data in the figures 3.29 does not show only protons, but also deuterons and hints for tritons, which exhibit the same energy pattern, but with higher energy deposition due to their larger mass.

[23]The example data used in this chapter is from 4h runs in the $^{12}C(e,e'p)^{11}B$ reaction, with Silicon Detector for proton and spectrometer A for electron detection. $E_{beam} = 480\ MeV$, $I_{beam} = 10\ \mu A$, $\theta_{Si} = 105°$, target thickness $d_{^{12}C} = 43.86\ mg/cm^2$, target angle $\theta_t = 45°$.

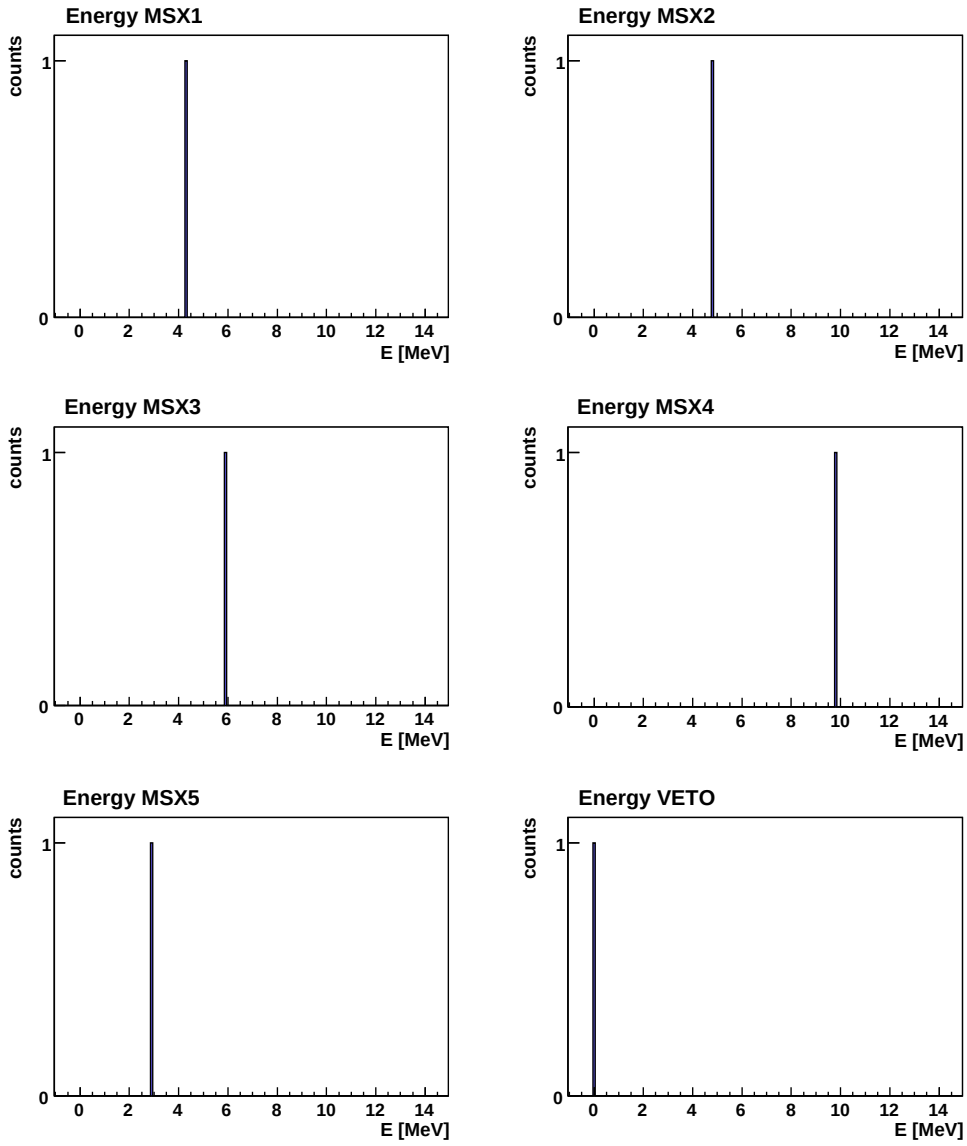

Figure 3.27: An example of energy deposition of a single particle in all the detector layers. The particle has traversed the first four layers and it stopped in the fifth, leaving zero energy in the veto detector.

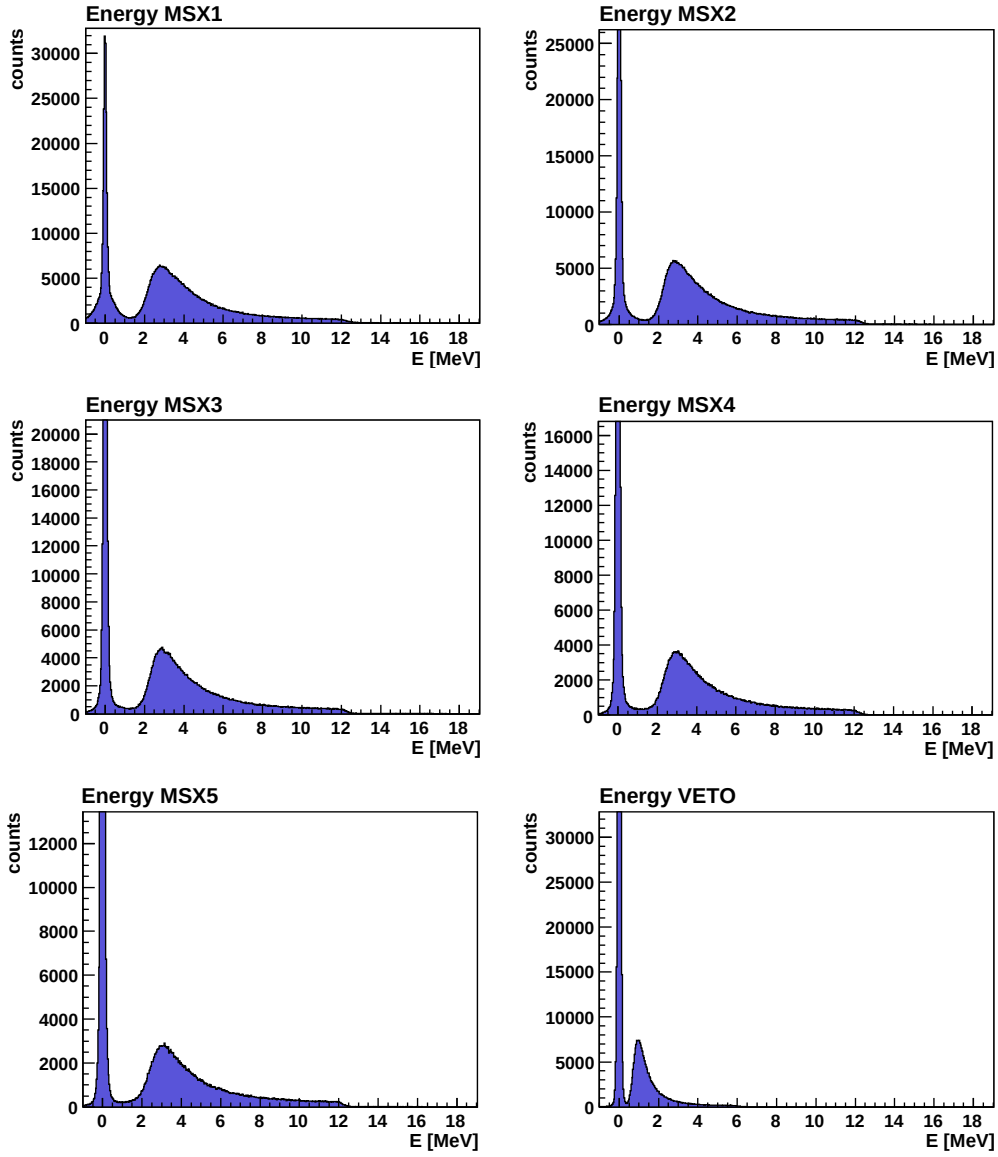

Figure 3.28: Energy spectra of the Silicon Detector layers.

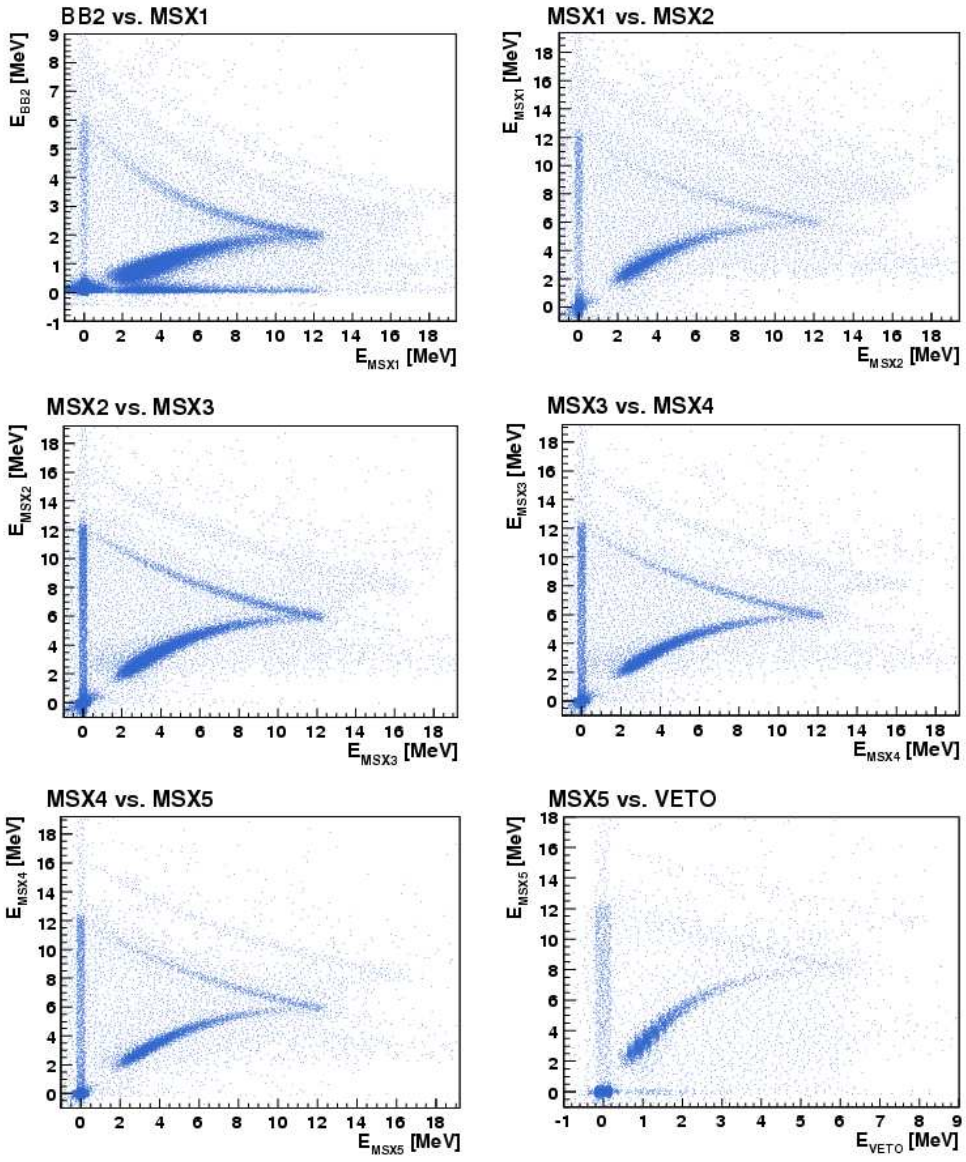

Figure 3.29: Two dimensional plots for successive layers of the Silicon Detector.

The energy spectra shown in this section are obtained by digitally processing the raw data with the variable shaping time algorithm, with shaping-time in the range of $T_S = 0.4 - 1.0\ \mu s$. For more details see B.2.2.

The total energy deposited in MSX layers E_{Si} is obtained by summing the energies of the layers with energy deposition greater than 0, or better say greater the base-line peak:

$$E_{Si} = \sum_{i}^{n} E_{MSXi} \tag{3.69}$$

where n is the number of the layer that brings the particle to complete stop. In the example in the figure 3.27, $n = 5$ because the particle is stopped in the fifth layer.

3.7.3 Particle identification

Particles with different mass and charge have different specific energy losses dE/dx, which is demonstrated by Bethe-Bloch formula. In the Silicon Detector the particles are identified by making cuts on two dimensional plot of the total energy deposition in MSX layers E_{Si}, versus energy deposition in the strip detector E_{BB2}. This is shown in the figure 3.30, where protons, deuterons and tritons can be distinguished. Typically, the Silicon Detector is used for proton detection, in which case a "banana-shaped" cut is made around the proton region.

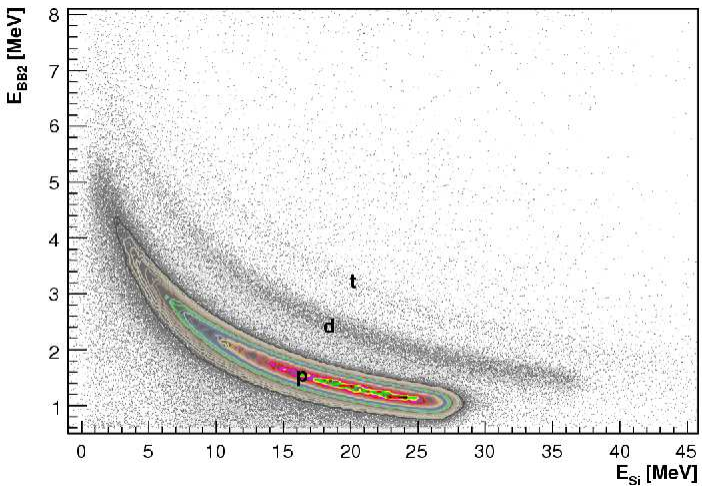

Figure 3.30: $E_{BB2} - E_{Si}$ plot used for particle identification.

3.7.4 Event selection

The conditions (cuts) for the acceptance of an event can be summarized as:

1. Cuts on detector acceptance:
   (a) $E_{BB2} > 0$, to ensure the particle has traversed the strip detector and its angles can be reconstructed.
   (b) $E_{VETO} = 0$, to reject those particles that are not fully absorbed by the detector layers. This condition can be modified by additionally selecting the particles that are stopped in the veto layer. In that case the energy acceptance is slightly larger.
2. Cut on protons, by selecting the proper region in $E_{BB2} - E_{Si}$ plot.

After applying these cuts, we obtain energy spectra and 2-dimensional energy deposition plots shown in the figures 3.31 and 3.32 respectively. These come from the same data as the spectra in the figures 3.28 and 3.29.

3.7.5 Four-momentum

Having identified the particle type and measured the energy deposited in the silicon layers, we want to obtain the initial energy of the particle. To do this we reconstruct energy loss in the front layers that are not used for energy measurement[24]. This is done on event-by-event basis by the analysis software `Cola++` [80], which calculates the energy losses using Bethe-Bloch formula (see e.g. [58]). The summed energy of five MSX layers E_{Si} (fig. 3.33) is used to reconstruct the energy loss in the strip detector (fig. 3.34), the scintillator (fig. 3.35) and the aluminum absorber (fig. 3.36). The target energy loss (fig. 3.37) is calculated using Bethe-Bloch formula for the given material and thickness, assuming the particles travel from the vertex in the middle of the target material to the edge, depending on their scattering angle and the angle of the target with respect to the beam. The energy loss in the MSX's entrance/exit windows (see section 3.4.3) is taken into account as well. All the reconstructed energies are added on event-by-event basis to the measured energy deposition E_{Si} to obtain the initial proton kinetic energy shown in the figure 3.38.

To obtain the initial four momentum of the proton in the laboratory

[24] Although the energy loss is measured in the strip detector and the scintillator, the overall energy resolution is better if the reconstructed instead of the measured energies are taken.

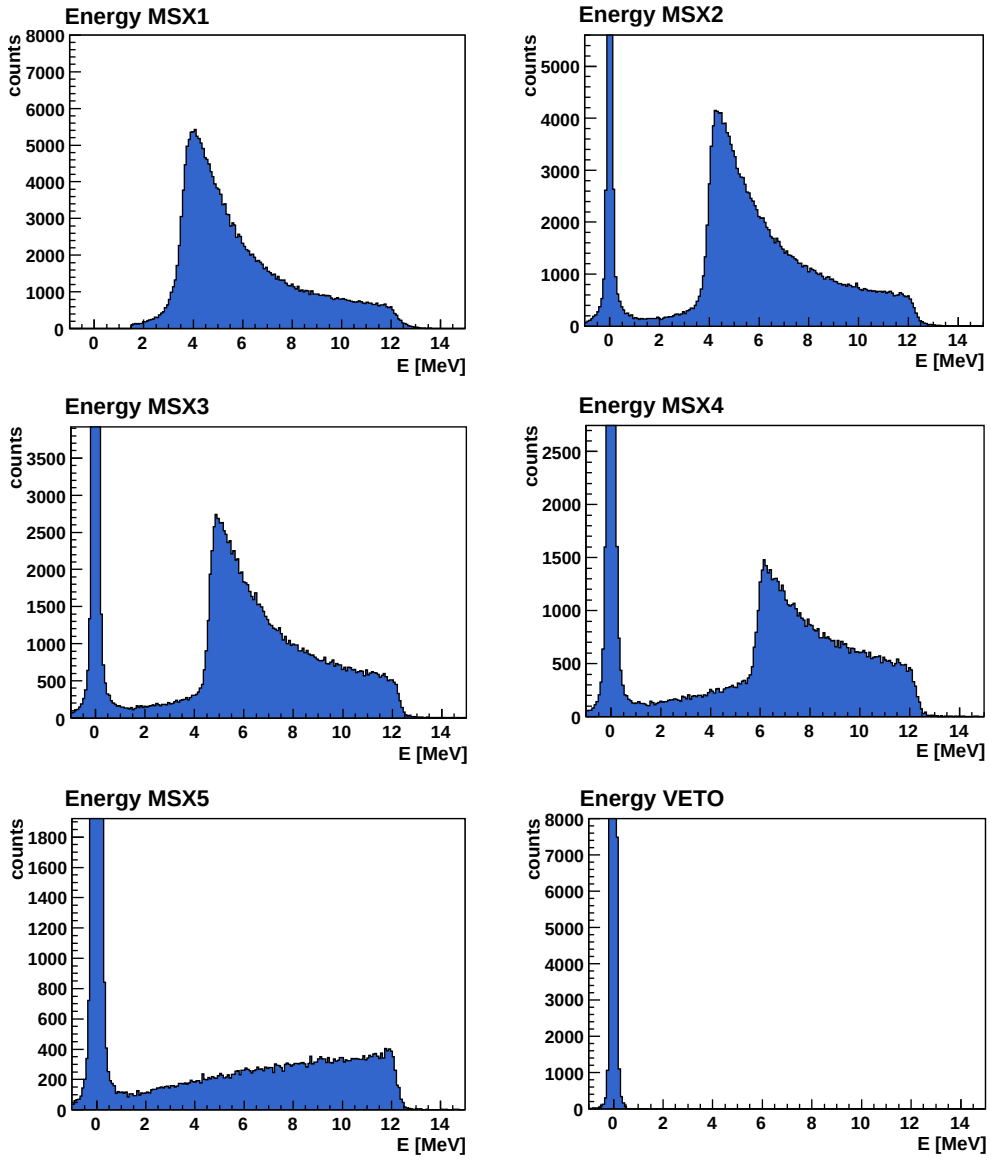

Figure 3.31: Energy spectra of the detector layers after applying the cut on detector acceptance and protons. The top of the base-line peak appears cut off, because the vertical scale is optimized for observing the physical part of the spectrum. (Note the different scales than in the figure 3.28.)

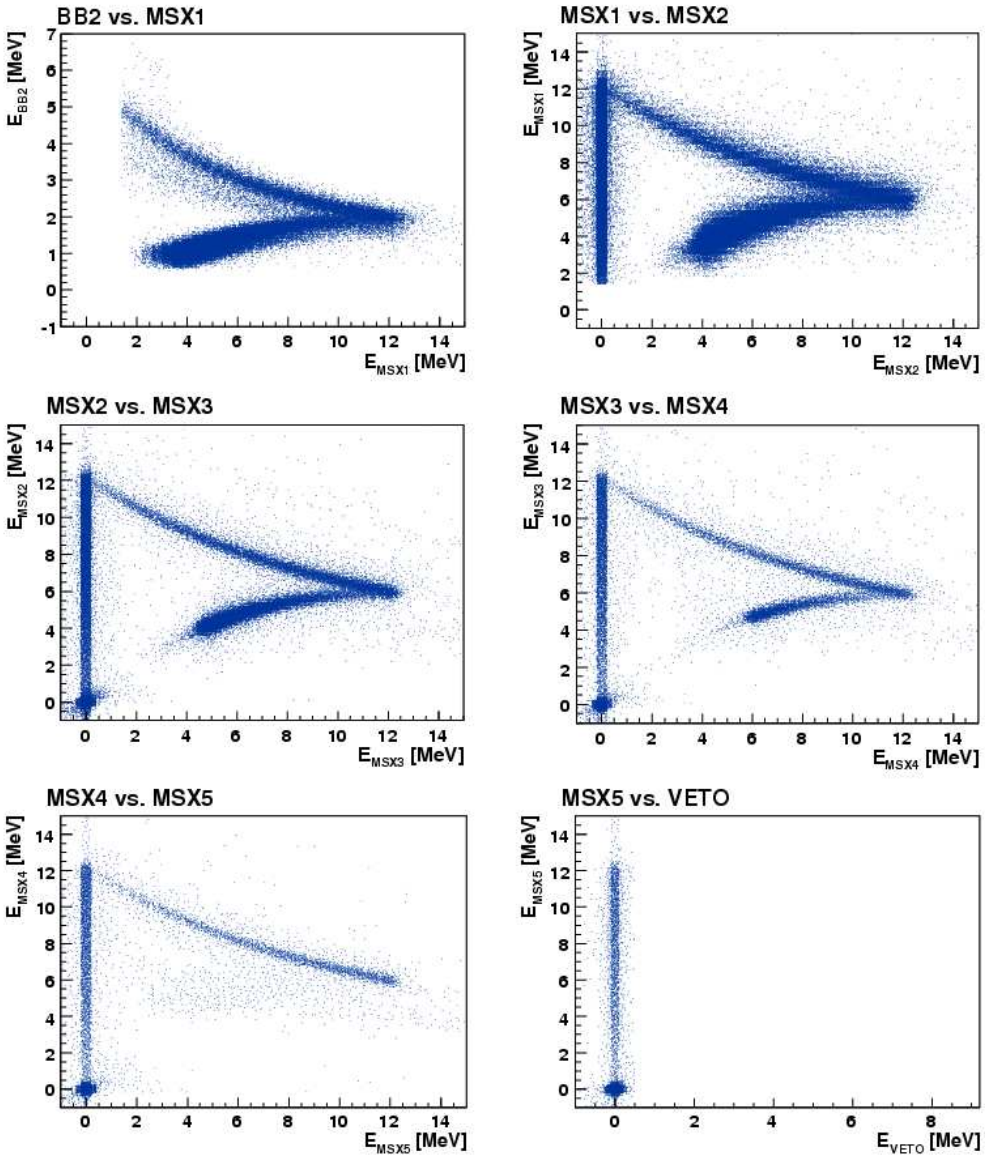

Figure 3.32: Two dimensional energy deposition plots for successive layers of the Silicon Detector after applying the cuts on detector acceptance and protons. (Note the different scales than in the figure 3.29.)

frame[25], its momentum is translated from Detector's coordinates to laboratory system coordinates. Technically, the momentum vector is first defined in detector coordinates according to:

$$p'_x = \frac{|\vec{p}|\tan\theta_{SD}}{\sqrt{1+\tan^2\theta_{SD}+\tan^2\phi_{SD}}} \tag{3.70}$$

$$p'_y = \frac{|\vec{p}|\tan\phi_{SD}}{\sqrt{1+\tan^2\theta_{SD}+\tan^2\phi_{SD}}} \tag{3.71}$$

$$p'_z = \frac{|\vec{p}|}{\sqrt{1+\tan^2\theta_{SD}+\tan^2\phi_{SD}}} \tag{3.72}$$

$$\tag{3.73}$$

and then it is rotated by θ_{Si} in the xz-plane, so its components in the laboratory frame are:

$$p_x = p'_x\cos\theta_{Si} + p'_z\sin\theta_{Si} \tag{3.74}$$

$$p_y = p'_y \tag{3.75}$$

$$p_z = -p'_x\sin\theta_{Si} + p'_z\cos\theta_{Si} \tag{3.76}$$

$$\tag{3.77}$$

The initial proton momentum and the scattering angles[26] in the laboratory frame are shown in the figure 3.39.

3.7.6 Vertex

The solid-state targets used in experiments with the Silicon Detector are thinner than 1 mm. On the other hand the vertex resolution of the detectors is 1 mm or higher, which makes the determination of the precise position of the vertex inside the target impossible.

However, the position of the beam spot in xy-plane is monitored via special luminescenting target Al_2O_3 and a digital camera. In this way the beam can be positioned in the center of the target, which sets the position of the vertex in the xy-plane. An example is shown in the figure 3.40. It is impossible to determine the position of the vertex along the beam ($\hat{z}$-direction) therefore it is supposed to be in the middle of the target.

[25]The laboratory coordinate system is defined by $\hat{z}$-axis pointing in the beam direction, $\hat{y}$-axis pointing up and $\hat{x}$-axis pointing left. The polar angles (θ, ϕ) are then defined relative to the $\hat{z}$-axis.

[26]In the laboratory frame the scattering angles (θ_p, ϕ_p) are polar angles defined relative to $\hat{z}$-axis.

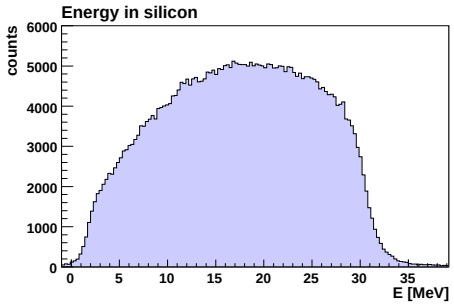

Figure 3.33: Total energy deposited in MSX layers.

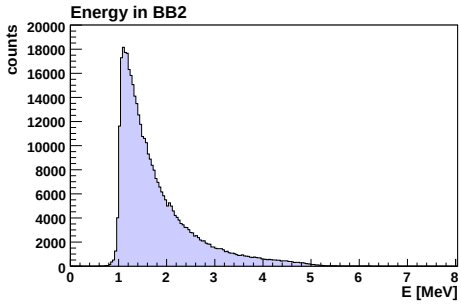

Figure 3.34: Reconstructed energy loss in BB2 detector.

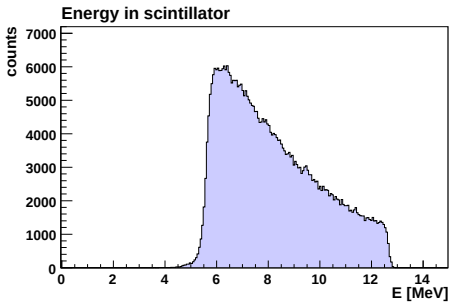

Figure 3.35: Reconstructed energy loss in the scintillator.

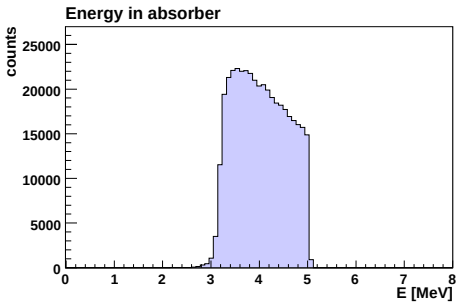

Figure 3.36: Reconstructed energy loss in the aluminum absorber.

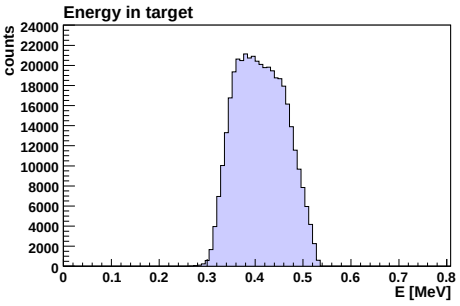

Figure 3.37: Reconstructed energy loss in the target.

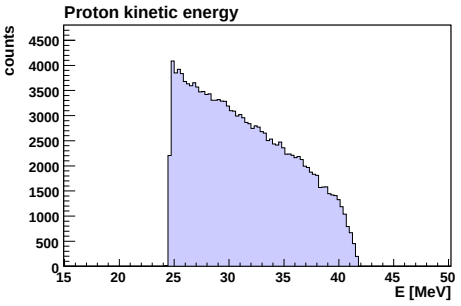

Figure 3.38: Reconstructed initial kinetic energy of the protons.

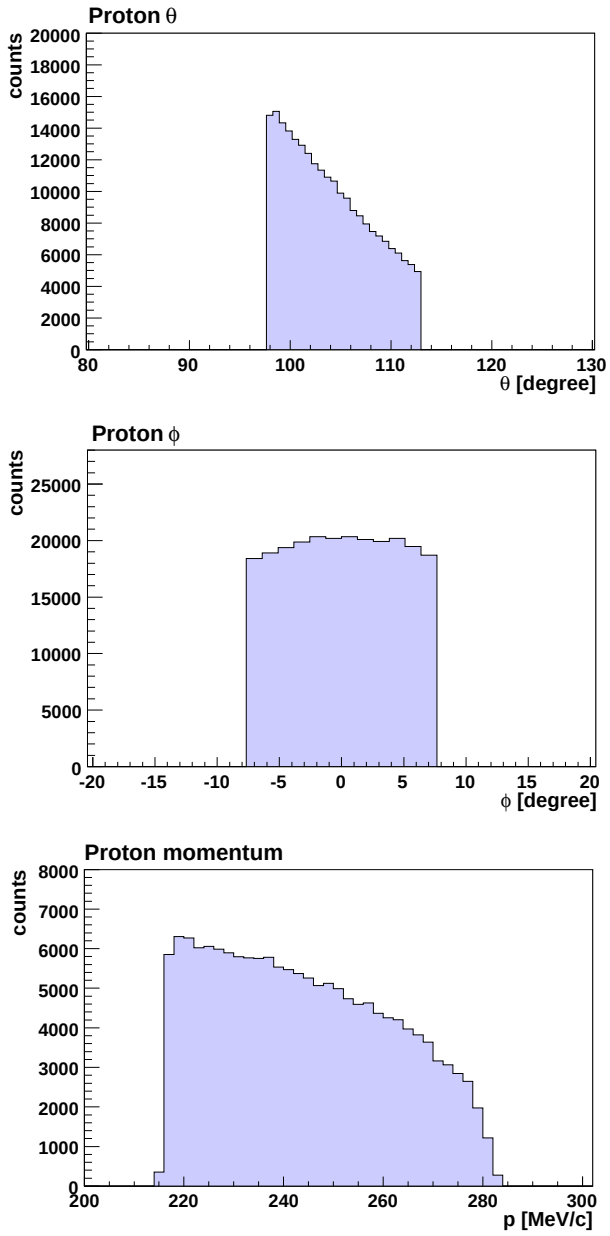

Figure 3.39: Proton angles θ_p (top), ϕ_p (middle) and the proton momentum (bottom) in the laboratory frame.

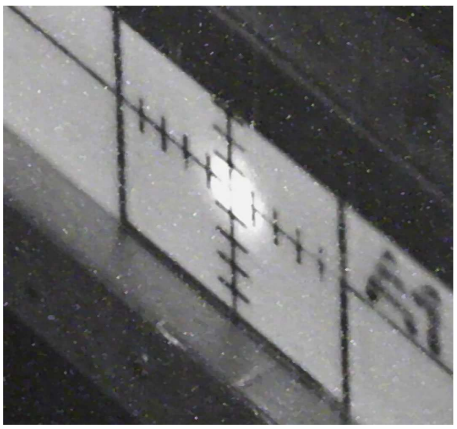

Figure 3.40: Target snapshot from the test beam-time in 2007. The target scale is in millimeters.

The indetermination of the exact vertex position influences mostly the particles of the lowest energy (in our case low-energy protons), because they have the largest energy loss in the target. In order to minimize the energy loss, and in this way the error in the energy measurement, the target is rotated at such angle to make the path of the lowest-energy particles through the target as short as possible.

3.8 Simulation

The simulation of the Silicon Detector is developed as a part of the Monte Carlo-based `Simul++` program (see appendix C.2) that is used for simulation of all detectors of the A1-collaboration.

When the simulation generates an event, it is tested to fall in the momentum and angular acceptances of the detectors. The simulated detector acceptances are somewhat larger than the real acceptances in order to avoid any event loss. The cuts on the real detectors acceptances are applied later.

In the simulation of the Silicon Detector the propagation of a particle is simulated layer by layer:

- geometry is checked to see if the particle track crosses the layer and the pathlength in the layer is calculated according to the incoming angle,
- if the pathlength in a layer is grater than zero, the energy loss is calculated using Bethe-Bloch formula, with steps not larger than 2 μm,
- multiple scattering angle is calculated based on Molière's theory, according to [58, 81], with steps not larger than 2 μm,

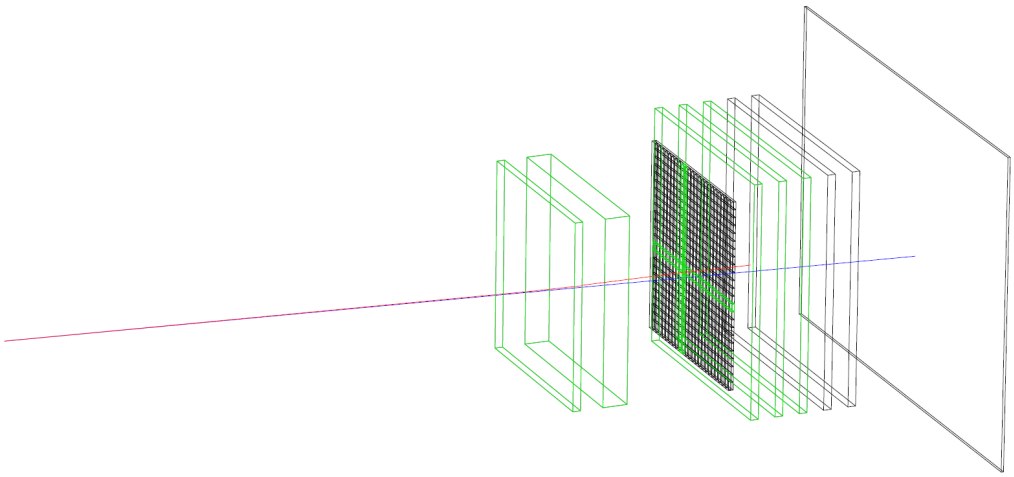

Figure 3.41: Simulation of a proton event in the Silicon Detector. The blue line shows the initial direction of the proton and the red line is direction changed by multiple scattering. The layers which the particle has traversed are shown in green, while the layers not reached by the particle are shown in black.

- if the particle has traversed the layer (as opposed to being absorbed) the energy straggling is simulated. This is done by generating a random energy loss according to [58]. This loss is than added/subtracted to the remaining particle energy.

The above steps are repeated for each successive layer, as long as the particle has some kinetic energy left. This procedure simulates particle energy loss in separate detector layers. The detector energy resolution is simulated by smearing the energy loss in each layer with a Gaussian distribution, with the standard deviation σ obtained from the corresponding experimental spectrum. The energy losses from each layer are summed and particle's initial energy is obtained.

The scattering angles of the generated particle are obtained by performing a geometrical check of the strip detector. This results in the relative position of the vertical and horizontal strip hit by the particle. This position is then transformed to laboratory coordinate system. Finally, the four-momentum of the particle is reconstructed from the simulated values in the same way as it is done from the measured values in the analysis package. An example of a simulated event is shown in the figure 3.41.

Chapter 4

Data Analysis

4.1 Coincidence timing

The time difference between the arrival of particles in different detectors can tell if these particles belong to the same reaction or if they are just random coincidences. Therefore, a good coincidence time resolution is important for distinguishing physical signals from the background. The resolution depends on the experimental apparatus, especially on the way the trigger of each detector is formed. For the spectrometers as for the Silicon Detector, the trigger is provided by plastic scintillators, which produce relatively fast signals ($\sim$1 ns). The optimal coincidence time resolution is achieved after applying corrections for the known hardware artefacts.

4.1.1 Corrections

Spectrometers

The following factors influencing spectrometers' time-resolution are corrected:

- The scintillator planes are segmented. The segments have slightly different cable-lengths and PMT amplifications. These are accounted for by introducing different time offsets in the analysis.
- The time of light propagation through the scintillator bars depends on the position of particle impact. This is precisely known from the drift-chamber information and can be corrected.
- Particles having different velocities and scattering angles will fly different tracks through spectrometers. The flight time can be subtracted after determination of particle's momentum and energy.

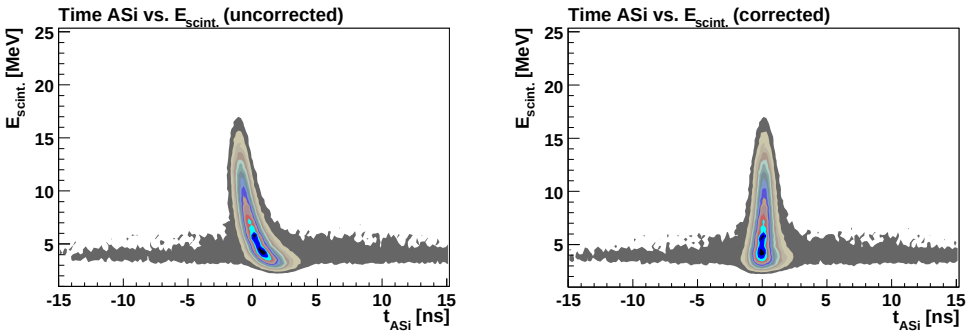

Figure 4.1: Discriminator walk correction for the trigger signal of the Silicon Detector.

Silicon Detector

The Silicon Detector is situated close to the target (8-11 cm), therefore different particle trajectories have a negligible influence on coincidence time. The trigger is determined by the scintillator placed in front of the stack of silicon layers. The scintillator signal is discriminated using a leading-edge discriminator, which produces the output signal relatively fast, but introduces a time-walk. This is a well know effect (see e.g. [58]) caused by the leading-edge discriminator having input signals with different amplitudes. The consequence is a spread of the coincidence time peak. However, this problem is effectively solved by introducing a simple software correction. The correction uses the fact that the coincidence time depends on the signal amplitude, which is proportional to the deposited energy. By making a phenomenological fit to uncorrected $t_{ASi} - E_{scint.}$ plot (figure 4.1 left), one can extract the energy dependence of the coincidence time. The function used for fitting is:

$$t_{fit}(E_{scint.}) = A_1 e^{-E_{scint.}/A_2} + A_3 \tag{4.1}$$

The energy dependence is thus eliminated by subtracting the fitted function from the uncorrected time:

$$t_{ASi} = t_{ASi,uncorr.}(E_{scint.}) - t_{fit}(E_{scint.}) \tag{4.2}$$

which is shown in the figure 4.1 (right).

4.1.2 Resolutions

In a triple-coincidence experiment, three time differences can be measured, although only two are independent. These are the coincidence times between spectrometers A and B (t_{AB}), between the Silicon Detector and the

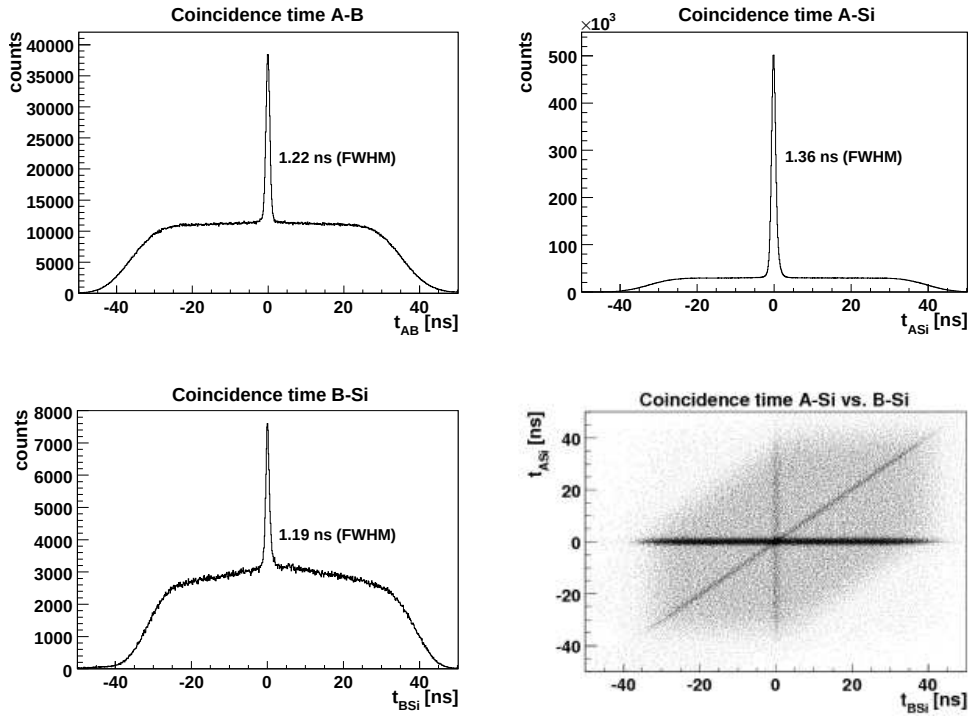

Figure 4.2: Coincidence time spectra for three detector pairs. The two-dimensional histogram (lower right) clearly shows all three types of coincidences.

spectrometer A (t_{ASi}) and between the Silicon Detector and the spectrometer B (t_{BSi}). Examples of (corrected) coincidence time spectra for a triple-coincidence experiment are shown in the figure 4.2, with the time resolutions under 1.5 ns (FWHM) for any detector pair. Figure 4.3 shows t_{ASi} versus t_{BSi}, where double-coincidence "walls" and triple-coincidence peak are clearly distinguishable from the background. The events contributing to the large peak in the middle are the true coincidences of three particles. The ones in the walls correspond to true coincidences of two particles, with a random coincidence with the third particle. The events in the flat region correspond to purely random coincidences. These figures also show that only two coincidence times are independent (orthogonal), while the third one can be calculated from the other two.

The previous discussion can be applied to double-coincidence measurements as well. In this case only the time difference between the particle arrival in the Silicon Detector and one of the spectrometers is measured.

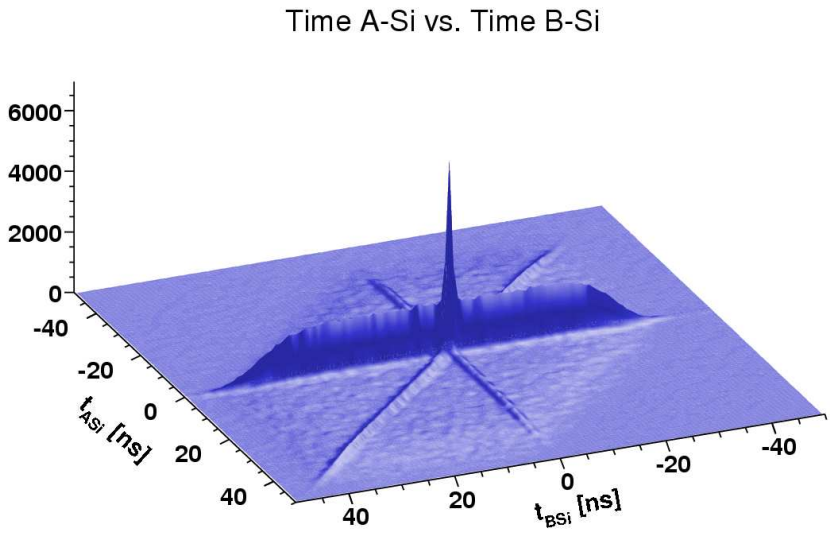

Figure 4.3: A three-dimensional representation of the time differences in a triple-coincidence measurement.

4.1.3 Background subtraction

By making cuts on coincidence time peaks, the true coincidence events can partially be separated from the random ones. With a better time resolution, the true-to-random coincidence ratio is higher and the separation is better. However, a finite contribution of the random coincidences will always be present in the coincidence peak. These events are uniformly distributed in the coincidence time spectrum, so they can be subtracted.

This is relatively simple for a double-coincidence measurements, where only one coincidence time spectrum exist. In that case, a histogram of an observable obtained with a cut on coincidence time peak contains the contribution from true and random coincidences. The histogram of that observable can also be made by making a cut on purely random coincidences. If the latter histogram is subtracted from the former one (applying the correct normalization factors), the resulting histogram should contain the number of events corresponding to the true coincidences only.

Background subtraction for triple-coincidence measurements is not so straight-forward, because in this case three not independent time spectra are involved. A two-dimensional coincidence time histogram is better suited to determine the share of the background in the coincidence peak. By mak-

ing two-dimensional cuts as depicted in figure 4.4 one selects four kinds of background events:

- A-B (true) + Si (accidental), figure 4.4 (middle, left)
- A-Si (true) + B (accidental), figure 4.4 (middle, right)
- B-Si (true) + A (accidental), figure 4.4 (down, left)
- A + B + Si (accidental), figure 4.4 (down, right)

The number of true triple-coincidences is obtained by subtracting these backgrounds from the total triple coincidences according to [37]:

$$H = H_{ABSi} - (aH_{AB} + bH_{BSi} + cH_{ASi} + dH_R) + 3dH_R \tag{4.3}$$

where H is the true-coincidence histogram of desired observable and H_k are histograms of the same observable with the applied cuts k. The normalization factors a, b, c, and d are determined by the ratio of the area of the ABSi-cut to the area taken for the cut k, according to the figure 4.4. The last term in equation 4.3 accounts for the fact that the random background is implicitly present in AB, ASi and BSi-cuts.

4.2 Detector efficiency

4.2.1 Silicon Detector

The efficiency of the Silicon Detector is primarily determined by the scintillator that provides the trigger. In order to measure scintillator's efficiency, the electronics scheme was modified so that the trigger was provided by the first MSX detector instead of the scintillator. The efficiency is obtained by dividing the number of events in the scintillator by the number of events in the first MSX. We obtained $\varepsilon_{scint.} = 0.97 \pm 0.01$ throughout the proton kinetic energy range of 25.2-40.6 MeV. In the border energy range 24.8-25.2 MeV, the scintillator efficiency sharply drops, therefore this border range should not be considered in the cross section calculation.

The efficiencies of the silicon layers BB2 and MSX are $\varepsilon = 0.99 \pm 0.01$. The one-per-cent inefficiency actually comes from the associated electronics. The total efficiency of the Silicon Detector is $\varepsilon_{SD} = 0.96 \pm 0.01$.

4.2.2 Spectrometers

The efficiency of the magnetic spectrometers is considered to be close to unity as well. As stated in [56] the scintillators have an average detection

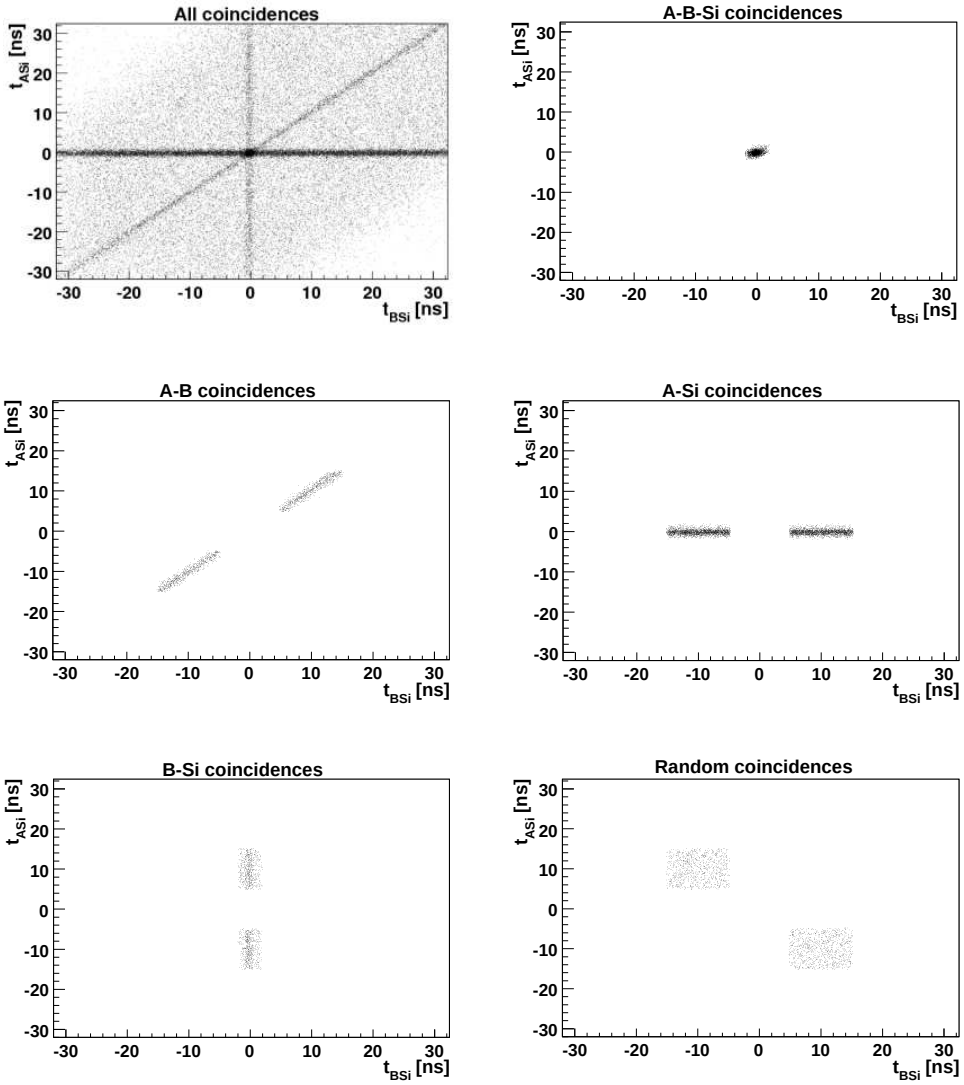

Figure 4.4: Histograms for background subtraction.

efficiency of 0.989, the vertical drift chambers 0.999 and the efficiency of the Čerenkov detector is 1. The spectrometer efficiency was not specially determined for the measurements described in the thesis, therefore the value of $\varepsilon_{Spec.} = 0.99 \pm 0.01$ from [56] is used.

4.3 Luminosity

For a continuous electron beam impinging on a fixed target, the luminosity is defined as:

$$L = jN_T \tag{4.4}$$

where j is the beam current density and N_T is the number of target nuclei. A more practical quantity is the integrated luminosity defined by:

$$\mathcal{L} = \int L dt \tag{4.5}$$

It can be written in terms of measurable quantities:

$$\mathcal{L} = \frac{Q}{e}\rho_T d_T \frac{N_A}{A_T} \tag{4.6}$$

where ρ_T [g/cm^3] and d_T [cm] are target density and length respectively, N_A [mol^{-1}] is the Avogadro constant and A_T [g mol^{-1}] is the molar mass of the target material.

When the target is rotated at an angle θ_T with respect to the beam, the effective target length increases by $1/\cos\theta_T$. For a fixed, solid-state target, the surface density of the target $S_T = \rho_T d_T$ is a well known parameter. In this case the integrated luminosity can be expressed as:

$$\mathcal{L} = \frac{1}{e}\frac{S_T}{\cos\theta_T}\frac{N_A}{A_T}Q \tag{4.7}$$

The total charge Q can be obtained by monitoring the beam current:

$$Q = \int_t I_b dt \tag{4.8}$$

where the integration is performed over time t. The beam current is monitored via Förster probes.

The experimental apparatus is not available for data acquisition all the time during a run. This is mainly because the electronic modules perform processes like analog-to-digital conversion, data transmission and recording,

etc., during which they cannot receive new data. The time that the system is unable to collect data is therefore called dead-time. The rest of the elapsed time is then simply called live-time, t_{live}. The dead-time is precisely measured for each run by means of micro-busy modules and the scalers mentioned in the section 3.6. Practically this means that the integral in the equation 4.8 should run over t_{live}. Thus by monitoring the beam current and the live-time, we can calculate the integrated luminosity. A program called `Lumi++` dedicated to this calculation is shortly described in appendix C.3.

4.4 Cross section

By definition, the total cross section is proportional to the total number of events produced per unit time R_{tot}. The proportionality constant is the luminosity L:

$$R_{tot} = L\,\sigma_{tot} \tag{4.9}$$

This equation can be integrated over live-time. In this case the rate is just substituted by the total number of events, and the luminosity by the integrated luminosity:

$$N_{tot} = \mathcal{L}\,\sigma_{tot} \tag{4.10}$$

Thus by measuring the number of produced events and knowing the luminosity, the total cross section can be extracted.

When detectors cover only a part of the phase-space accessible by the reaction[1], the measured quantity is the differential cross-section. For a simple case when it is constant over the covered phase-space volume V_{ph} we can write:

$$\frac{d\sigma}{d\Omega} = \frac{N}{\varepsilon\,\mathcal{L}\,V_{ph}} \tag{4.11}$$

N being the total number of detected events and ε the detection efficiency.

4.4.1 A(e,e'pp)B reactions

In an unpolarized A(e,e'pp)B scattering, we have four particles in the final state, having 16 kinematical variables in total. Nine of these variables are independent because four are eliminated due to energy and momentum conservation and another three by defining the mass of three out of four outgoing particles - electron and two protons. If the detector resolution is

[1] i.e. detectors have certain angular and momentum acceptance.

good enough it enables measuring the cross-section variation inside the detector acceptance, as a function of a variable x (e.g. $x = p_b$, the missing momentum). The differential cross-section is then expressed as:

$$\frac{d^9\sigma}{d\Omega_e dE' d\Omega_{p_1} dT_{p_1} d\Omega_{p_2} dT_{p_2}}(x) = \frac{N}{\varepsilon\,\mathcal{L} < V_{ph}^9(x) >} \tag{4.12}$$

where N is the background-corrected total number of events, ε is detector efficiency and $\mathcal{L}$ is the dead time-corrected integrated luminosity. E', T_{p_1} and T_{p_2} are kinetic energies of the outgoing electron and two protons, respectively. The phase-space volume covered by detectors $< V_{ph}^9(x) >$ is given by:

$$< V_{ph}^9(x) >= \frac{\mathcal{N}_{BIN}(x)}{\mathcal{N}_{TOT}(x)}\,\Lambda \tag{4.13}$$

where $\mathcal{N}_{BIN}(x)$ is the number of events in a bin of variable x, and $\mathcal{N}_{TOT}(x)$ is the total number of events. The experimental acceptance of detectors Λ is given by:

$$\Lambda = \Delta\Omega_e \Delta E' \Delta\Omega_{p_1} \Delta T_{p_1} \Delta\Omega_{p_2} \Delta T_{p_2} \tag{4.14}$$

If the recoiling nucleus is left in a definite final state, e.g. ground state (GS), another kinematical variable - the final state energy, is fixed. Therefore, the cross-section for the transition to a definite final state becomes eight-fold:

$$\frac{d^8\sigma}{d\Omega_e dE' d\Omega_{p_1} dT_{p_1} d\Omega_{p_2}} = \int\limits_{\Delta E_x} \frac{d^9\sigma}{d\Omega_e dE' d\Omega_{p_1} dT_{p_1} d\Omega_{p_2} dT_{p_2}} \left|\frac{\partial T_{p_2}}{\partial E_x}\right| dE_x \tag{4.15}$$

where the integration is performed over the excitation energy range of the final state in question ΔE_x. The Jacobian $\left|\frac{\partial T_{p_2}}{\partial E_x}\right|$ should be applied to account for the transition from the phase-space variable[2] T_{p_2} to the integration variable E_x.

Another way to express the eight-fold differential cross section for the transition to the ground state of the recoiling nucleus is to write an equation analogous to the equation 4.12:

$$\frac{d^8\sigma}{d\Omega_e dE' d\Omega_{p_1} dT_{p_1} d\Omega_{p_2}}(x) = \frac{N_{GS}}{\varepsilon\,\mathcal{L} < V_{ph}^8(x) >} \tag{4.16}$$

where in this case only the events in the ground state N_{GS} contribute, and the phase-space $< V_{ph}^8(x) >$ is given by:

$$< V_{ph}^8(x) > = \frac{\mathcal{N}_{BIN}(x)}{\mathcal{N}_{TOT}(x)}\,\Lambda, \tag{4.17}$$

$$\Lambda = \Delta\Omega_e \Delta E' \Delta\Omega_{p_1} \Delta T_{p_1} \Delta\Omega_{p_2} \tag{4.18}$$

[2]The selection is arbitrary, any one of the phase-space variables can be taken.

4.5 Phase-space

The phase-space volume $< V_{ph}^{8}(x) >$ covered by detectors cannot be calculated analytically for the measurements described in this work. It is determined by a Monte-Carlo simulation[3] taking into account the angular and momentum acceptances of the detectors involved. The simulation is made for only one excitation energy of the recoiling nucleus, in this case for the ground state of ^{10}Be. The particle energy losses inside the target (described in the subsection 4.5.1) are simulated as well. Finally, the simulated histogram is normalized to the 8-dimensional detection volume $\Lambda = \Delta\Omega_e \Delta E' \Delta\Omega_{p_1} \Delta T_{p_1} \Delta\Omega_{p_2}$. The phase-space simulation is described in more detail in appendix D.

The simulation parameters such as detector resolution, as well as cuts and histogram binning, are selected to exactly match the parameters used in the analysis. This ensures the consistency of the simulated and the experimentally obtained data in the calculation of the cross sections.

4.5.1 Radiative corrections

The incoming, as well as the outgoing electron can suffer (unwanted) energy losses in the target due to internal[4] or external[5] bremsstrahlung or ionization of target atoms. These processes influence the energy determination of the particles in the final state. This is reflected as the high-energy tail in the excitation energy spectrum of the final nucleus. Consequently, the number of particles in the peak belonging to a specific final state will be reduced, which must be taken into account when the cross-section is calculated.

The electron energy losses due to the mentioned processes are included in the phase-space simulation. In this way the radiative corrections are applied to the cross section through the introduction of the normalized phase-space. The figure 4.5 shows a simulated excitation energy E_x in the ^{12}C(e,e'pp)$^{10}Be(GS)$ reaction. The radiative tail to the simulated ^{10}Be ground state is clearly visible.

4.6 Error estimation

The error of the measured cross section has statistical and systematic sources. While the statistical sources depend on the number of detected events, the

[3] The simulation is performed using the `Simul++` program (see appendix C.2).

[4] Emission of a photon in the electromagnetic field of the hit target nucleus.

[5] Emission of a photon in the electromagnetic field of some other nucleus in the target.

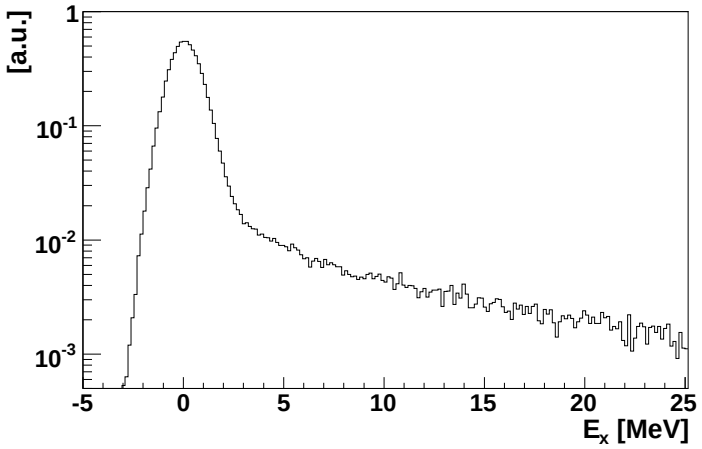

Figure 4.5: Simulated excitation energy E_x in the ^{12}C(e,e'pp)^{10}Be(GS) reaction. The events in the high-energy tail are due to electron energy losses.

systematic uncertainties are inherited from the experimental apparatus.

4.6.1 Statistical errors

The statistical errors are connected with the number of events in a bin. More precisely, they are given as the square root of the total number of counts (signal+background) [82]. According to [37] this can be written as:

$$\Delta T = \sqrt{T + (1 + S)B} \tag{4.19}$$

where T is the number of true coincidences and B is the number of background events in the bin. S is the ratio of the background events in the A-B-Si cut to the background events in the "randoms" cut, as depicted in figure 4.4. From this figure it is clear that $S \ll 1$ and can be neglected. So the uncertainty of the true number of events is equal to the uncertainty of the total number of events:

$$\Delta T = \sqrt{T + B} = \sqrt{N} \tag{4.20}$$

The statistical uncertainty can be made smaller by increasing the bin width and hence the number of events in the bin. This on the other hand means decreasing the resolution of the cross section, so a compromise should be made.

The error connected with the phase-space simulation can be neglected, as it can be made with an arbitrary large number of events.

Source of error	Contribution
Luminosity calculation	5.2 %
Detector efficiency	1.4 %
GS Cut	5.0 %
Total systematic $\sigma_{sys.}$	7.3 %

Table 4.1: The contributions to the systematic error $\sigma_{sys.}$ of the cross section.

4.6.2 Systematic errors

The largest source of the systematic error of the cross section comes from the calculation of the luminosity. The target was rotated with respect to the beam with an angular uncertainty $\sigma_{\theta_T} = 3°$. This enters the equation 4.7 and contributes to the uncertainty of the luminosity with 5.2 %.

Another possible source of error in counting the number of true events can come from the cut on the excitation energy of the final nucleus. For example, a $\pm 2\sigma$ cut on a Gaussian-shaped peak should cover 95% of the events in that state, therefore the uncertainty in the number of events is estimated to 5%.

Finally the detection efficiency of the spectrometers has an uncertainty of 1%, the same as that of the Silicon Detector, which totals to 1.4 %. All contributions to the systematic error to the cross section are summarized in table 4.1.

As it will be shown by the results laid out in chapter 5 the statistical errors of the cross section will dominate over the systematic ones.

Chapter 5

Experiments and results

This chapter presents the results of the experiments performed with the Silicon Detector. The experiments were put through during several beam-times in the period 2004 - 2008. During this time the Detector was being developed, so some of the beam-times had a testing purpose and some were dedicated to physics production. The chronology of these beam-times is given in appendix E.

5.1 Quasi-elastic proton knockout from ^{12}C

The measurement of the quasi-elastic proton knockout reaction $^{12}C(e, e'p)^{11}B$ was performed to test the performance of the Silicon Detector, especially to test its energy resolution in high particle flux environments. The particle flux was varied by changing the beam current and detector angle. In this double-coincidence measurement the Silicon Detector was used to detect the protons, while spectrometer A was detecting the electrons.

In the simple approach of one-photon exchange approximation, the virtual photon interacts with a single proton inside the target nucleus, as if it were free, and knocks it out. This approximation can be justified, because the energy transfer is much higher than the proton separation energy. The reaction momentum is then balanced by the remaining ^{11}B nucleus. The measurement was exclusive, meaning that four-momenta of all the particles involved could be determined. The momentum and the energy of the recoiling nucleus ^{11}B were not measured directly, but they could be inferred from the energy and momentum conservation laws.

The missing momentum and the missing energy are defined as: (with $c \equiv 1$)

$$\vec{p}_m = \vec{q} - \vec{p}_p \quad (5.1)$$

$$E_m = M_{^{12}C} + \omega - E_p \quad (5.2)$$

The missing mass is defined by:

$$m_m = \sqrt{E_m^2 - \vec{p}_m^{\,2}} \quad (5.3)$$

By subtracting the mass of the ^{11}B ground state, we obtain the excitation energy of the recoiling ^{11}B nucleus:

$$E_x = m_m - M_{^{11}B} \quad (5.4)$$

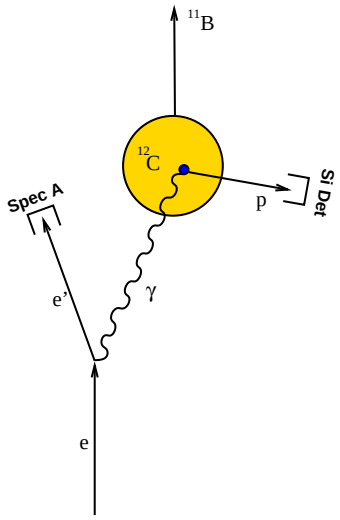

Figure 5.1: A schematic of $^{12}C(e, e'p)^{11}B$ reaction.

Thus by measuring the proton scattering angles and energy, its four-momentum $(E_p, \vec{p}_p)$ can be reconstructed. From the measured energy and angles of the scattered electron, we determine the energy and momentum transfer of the virtual photon $(\omega, \vec{q})$, Then according to equations 5.1 to 5.4, ^{11}B excitation energy spectrum can be reconstructed as well. The main parameter of interest in the measurement is the energy resolution of that spectrum[1] ΔE_x, which is defined as the full-width-at-half-maximum of ^{11}B ground state peak.

5.1.1 Experimental setup

The Silicon Detector was working as described in section 3.2. The distance of the detector from the target was 8.9 cm, resulting in an angular acceptance of 72 msr. The scintillator was used for triggering, with a good electron-proton coincidence time resolution $\Delta t_{ASi} < 1.5$ ns (FWHM). The proton energies were extracted by sampling the preamplifier [83] signals with the 100 MHz flash ADC [84]. These signals were digitally shaped with the variable-shaping-time algorithm (see appendix B.2.2), with the shaping time range $T_S = 0.4 - 1.0\ \mu s$.

We used a fixed graphite target of 43.86 mg/cm^2 surface density. The spectrometer A was in the standard configuration as described in [3].

[1] Also called the missing mass resolution Δm_m.

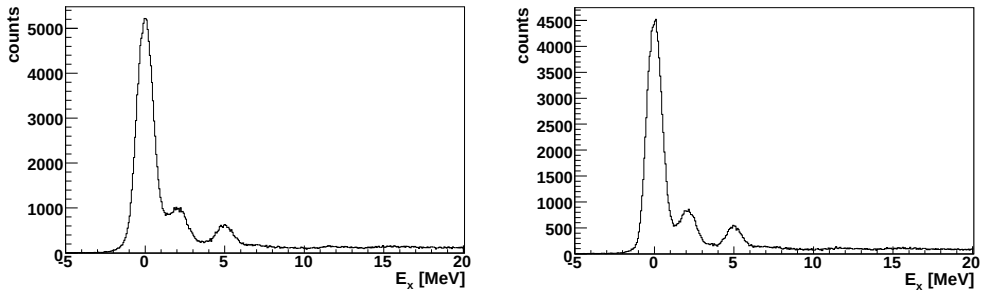

Figure 5.2: The excitation energy spectrum reconstructed with five MSX layers (left) and the last four MSX layers (right). The resolutions are $\Delta E_x =$ 1.23 MeV and $\Delta E_x = 1.10$, respectively.

In this experiment, the proton energy reconstruction is done by using only four of five silicon layers (MSX). The first layer has the poorest energy resolution, because it receives the largest particle flux, leading to the highest signal pile-up σ_{BL} as discussed in section 3.3.1. The exclusion of the protons stopped in the first layer improves the final energy resolution. This is demonstrated in figure 5.2, where the left histogram is obtained using all five layers and the resolution is $\Delta E_x = 1.23$ MeV and the right histogram is obtained using the last four layers and the resolution is $\Delta E_x = 1.10$ MeV. On the other hand this reduces the proton energy acceptance from $\Delta T_p =$ 25.2 - 40.6 MeV to $\Delta T_p =$ 28.6 - 40.6 MeV, but this is not crucial in this experiment, as the counting rates are sufficiently high.

5.1.2 ^{11}B excitation spectrum

The spectra from the measurements at different kinematics are shown in the figures 5.3 to 5.8. They are all obtained with a cut on coincidence time peak $|t_{ASi}| < 1.75$ ns and the background is subtracted. Tables along each spectrum show beam current I_b and energy E_b, spectrometer angle θ_e and central momentum p_{cent}, Silicon Detector angle θ_{SD} and counting rate R_{SD}, energy transfer ω, momentum transfer $|\vec{q}|$ and the energy resolution ΔE_x.

The ^{11}B ground state is visible in all obtained spectra[2]. The energy resolution ranges from ΔE_x=1.1 - 1.4 MeV, depending on the setup. The first excited state is obtained at $E_x = 2.1 \pm 0.7$, which is in a fairly good agreement with [77]. Other excited states are present as well, but they lay too close to be distinguished.

[2]The peaks in the spectra are identified by making gaussian fits, with standard deviation taken as error.

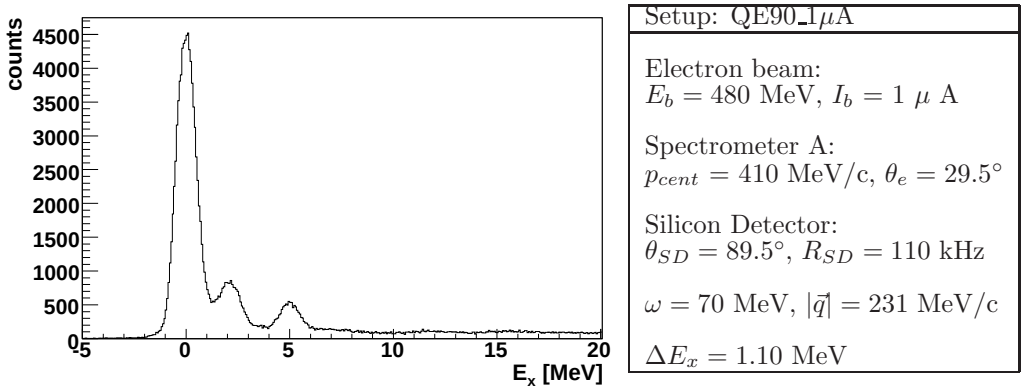

Figure 5.3: Excitation spectrum of ^{11}B in kinematic setup QE90_1μA.

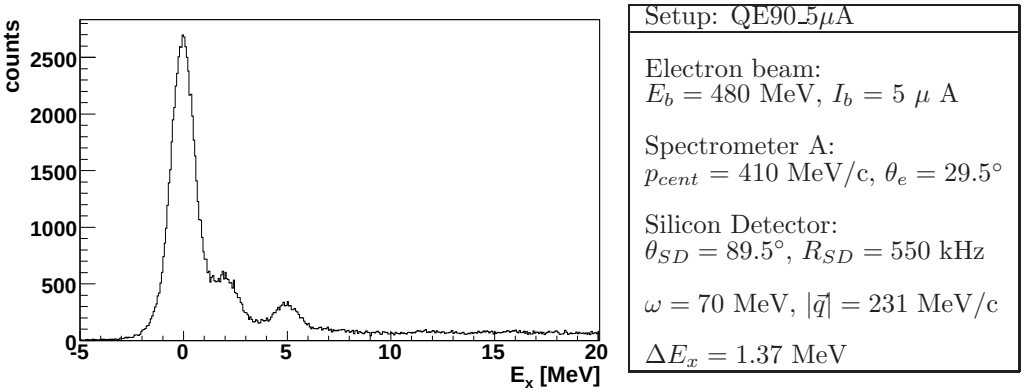

Figure 5.4: Excitation spectrum of ^{11}B in kinematic setup QE90_5μA.

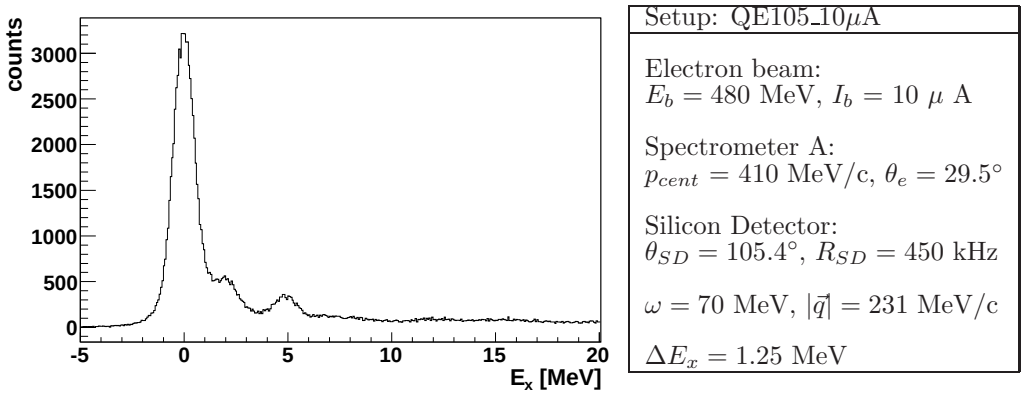

Figure 5.5: Excitation spectrum of ^{11}B in kinematic setup QE105_10μA.

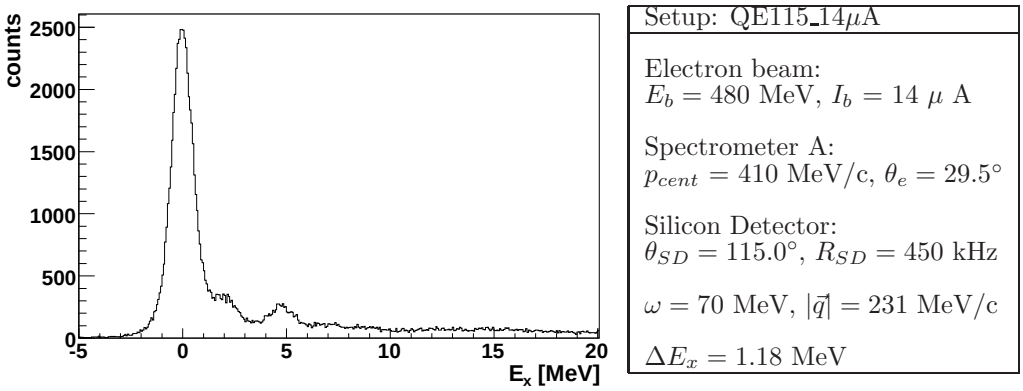

Figure 5.6: Excitation spectrum of ^{11}B in kinematic setup QE115_14μA.

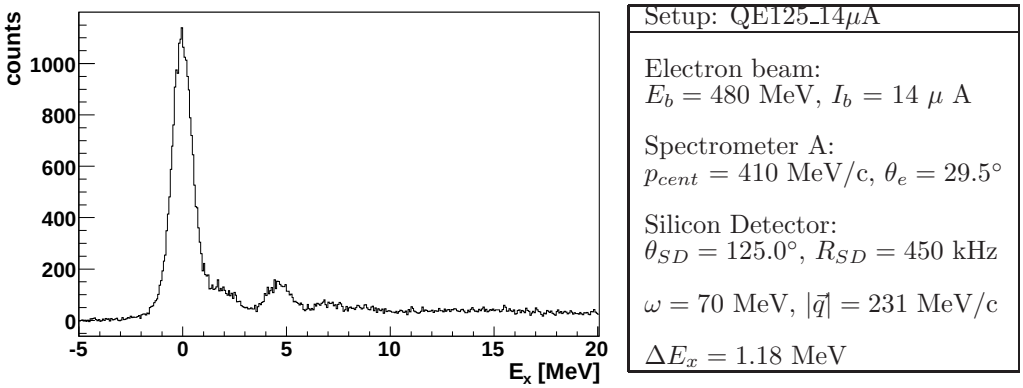

Figure 5.7: Excitation spectrum of ^{11}B in kinematic setup QE125_14μA.

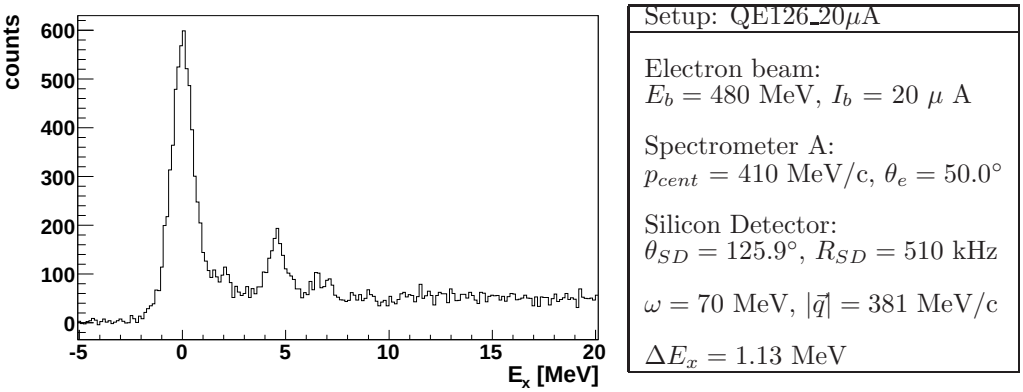

Figure 5.8: Excitation spectrum of ^{11}B in kinematic setup QE126_20μA.

5.2 Investigation of ^{12}C(e,e'pp)^{10}Be reaction

The motive behind the experiment is the investigation of short-range correlation effects in ^{12}C nucleus. The kinematics was selected in a way, that SRC effects are expected to have a large influence on the cross-section. The direct goal of this measurement was to determine the differential cross-section for the $^{12}C(e,e'pp)^{10}Be$ (GS) reaction.

5.2.1 Kinematics

The triple-coincident measurement was performed in super-parallel kinematics, in which one proton is ejected parallel and the other one anti-parallel to momentum transfer. Spectrometer B was used to detect the scattered electron, spectrometer A the forward proton and Silicon Detector the backward proton, which is schematically shown in figure 1.4.

The angle of the spectrometer B was chosen to be as small as possible in order to increase the virtual photon flux and its central momentum was optimized to accept the electrons scattered in the "dip" region. The Silicon Detector was positioned at 153° and the spectrometer A at 28° with respect to the beam. The details of the kinematical setups are summarized in table 5.1.

The choice of kinematics was discussed in detail in section 1.2.3. To recapitulate, the super-parallel kinematics with energy transfer ω=163 MeV and momentum transfer $|\vec{q}|$=198 MeV/c was chosen according to calculations [34] (see figure 1.6), which indicate that SRC should have a significant effect on the cross-section. At the same time the "background" contributions, like meson exchange currents and isobar configurations (Δ states) are expected to be minimal, as well as nucleon-nucleon final state interaction. Measuring in the "dip" region should further suppress Δ excitation.

Setup no.	E_b [MeV]	I_b [μA]	θ_e [°]	E' [MeV/c]	θ_{p_1} [°]	p_{p_1} [MeV/c]	θ_{p_2} [°]	p_{p_2} [MeV/c]	Time [h]
1	480	15	16.5	315.9	28.0	420.0	153.0	248.0	5
2	480	25	16.5	315.9	28.0	420.0	153.0	248.0	121
3	480	30	16.5	315.9	28.0	420.0	153.0	248.0	4

Table 5.1: The kinematic setups for investigation of $^{12}C(e,e'pp)^{10}Be$ reaction. The angles and momenta refer to detectors' central values.

5.2.2 Experimental setup

In this experiment, the Silicon Detector was in the standard configuration, as described in section 3.2. The distance of the detector from the target was 8.9 cm and the angular acceptance was 72 msr. The proton kinetic energy acceptance of the Silicon Detector was ΔT_p = 25.2 - 40.6 MeV. The spectrometers A and B were working as described in [3]. Coincidence time resolution between any of the detectors was $\Delta t < 1.5$ ns (FWHM).

The energies of protons detected in the Silicon Detector, were extracted by sampling the preamplifier [83] signals with the 100 MHz flash ADC [84]. These signals were digitally shaped with the variable-shaping-time algorithm (see appendix B.2.2) using the shaping time range $T_S = 0.4 - 1.0\ \mu s$. The introduction of the flash ADC and the digital shaping, instead of the analog signal processing, proved to be of crucial importance because it enabled achieving a better energy resolution while maintaining relatively high counting rate in the Silicon Detector. It is important to keep the energy resolution sufficient for separation of the ground state in ^{10}Be excitation energy spectrum. Maximizing the counting rate is critical for obtaining enough statistics in triple-coincidence measurements, because the expected triple-coincidence rates are relatively low (< 100 per day) and the available beam-time is usually limited.

The graphite target (43.86 mg/cm^2) was rotated 45° counter-clockwise to minimize the energy loss of the low-energy protons detected by the Silicon Detector at backward angles. The measurement was performed in 2008 during 1 week of beam-time. We used the beam currents up to $I_b = 30\ \mu A$, where that limit was set by the maximum acceptable counting rate in the Silicon Detector, which was ∼500 kHz at this current and detector angle.

5.2.3 ^{10}Be excitation spectrum

By applying the cuts on three coincidence times, the events that correspond to coincident electron and two protons are selected. The applied cuts are: $|t_{AB}| < 1.75$ ns, $|t_{ASi}| < 1.75$ ns and $|t_{BSi}| < 1.75$ ns. The background is subtracted according to procedure described in section 4.1.3. The excitation energy of the recoiling nucleus, in this case ^{10}Be is defined according to equation 1.13 and the obtained spectrum is presented in the figure 5.9.

The positions of the peaks in ^{10}Be excitation spectrum are identified by making gaussian fits, taking standard deviations of the gaussians as errors. The results are presented in table 5.2. The energy resolution is $\Delta E_x = 1.7$ MeV (FWHM), sufficient to separate the ground state from the first excited state at $E_x = 3.4$ MeV.

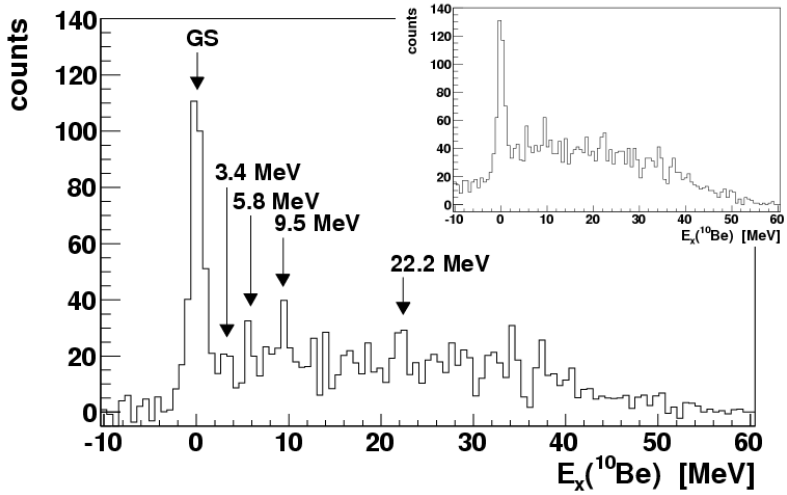

Figure 5.9: Excitation spectrum of ^{10}Be. The data is from all runs with the cut on three coincidence times. The small histogram in the upper right corner shows the spectrum before background subtraction.

The figure 5.9 shows a dominant ground state of ^{10}Be. Calculations for $^{16}O(e,e'pp)^{14}C$ reaction in super-parallel kinematics [20] predict a dominant ground state transition for low missing momenta $p_b \approx 0$, which was confirmed in experiment [37]. Because the ground state of ^{14}C has $J^\pi = 0^+$, one can expect that it is mostly populated by knockout of $^1S_0$ proton pairs having angular momentum L=0. As the ground state of ^{10}Be is also a 0^+ state, the dominance of $^1S_0$ proton pairs is expected here as well. The distance between the nucleons is the smallest in the $^1S_0$ configuration, therefore such configuration is preferred for the study of short-range correlations.

E_x measured [MeV]	Previous work [MeV]	J^π
0 ± 0.7		0^+
3.4 ± 0.8	3.37 [77]; 3.31 [85]	2^+
5.8 ± 0.8	5.96 [77]; 5.91 [85]	2^+
9.5 ± 0.9	9.56 [77]; 9.58 [85]	2^+
22.2 ± 1.0	22.40 [77]	

Table 5.2: The identified peaks in the ^{10}Be excitation spectrum. Comparison with previous work is made when available.

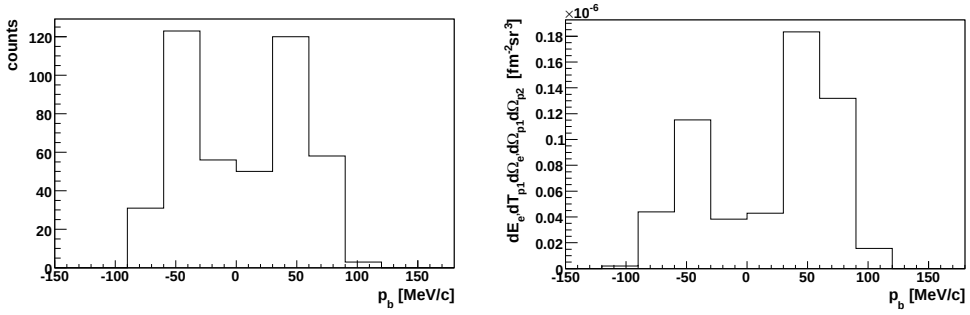

Figure 5.10: Missing momentum distribution for ^{10}Be in the ground state. The measured, background-uncorrected spectrum is in the left figure, while the simulated phase-space is shown in the right.

5.2.4 Differential cross section

The differential cross section of $^{12}C(e,e'pp)^{10}Be$ reaction, for the transition to the ^{10}Be ground state (GS) has been extracted as a function of the reaction missing momentum $|\vec{p}_b\,|$. In the super-parallel kinematics this momentum is either parallel or anti-parallel to the momentum transfer $\vec{q}$, so we define p_b to acquire positive values when parallel and negative values when anti-parallel to $\vec{q}$. The events in ^{10}Be ground state are selected by a cut in the excitation energy spectrum $|E_x| < 1.7$ MeV.

The data taking time was 131 hours, with an average dead time of 11.8%. The integral, dead time-corrected luminosity was $\mathcal{L}_{eff} = 198629$ pb^{-1}. The overall efficiency of the detector system is obtained by multiplying the efficiencies of two spectrometers and the Silicon Detector, so one obtains $\varepsilon = 0.99 \times 0.99 \times 0.96 = 0.94$. The experimental volume Λ was calculated according to equation 4.18 with detector acceptances given in table 5.3.

Figure 5.10 (left) shows the measured number of events N in p_b spectrum with the cut on three coincidence times, detector acceptances and ^{10}Be ground state, while figure 5.10 (right) shows the simulated phase-space for ground state transition, normalized to detection volume Λ. The bin width in both histograms is 30 MeV/c.

Finally, the differential cross section is obtained according to relation

Spectrometer B: e^-	Spectrometer A: p_1	Silicon Detector: p_2
$\Delta\Omega'_e$=0.0056 sr	$\Delta\Omega_{p_1}$=0.028 sr	$\Delta\Omega_{p_2}$=0.0718 sr
$\Delta E'_e$=47.0 MeV	ΔE_{p_1}=40.6 MeV	ΔE_{p_2}=15.4 MeV
(340.0-293.0 MeV)	(114.2 - 72.0 MeV)	(40.6 - 25.2 MeV)

Table 5.3: The acceptances of the detectors used for cross section calculation.

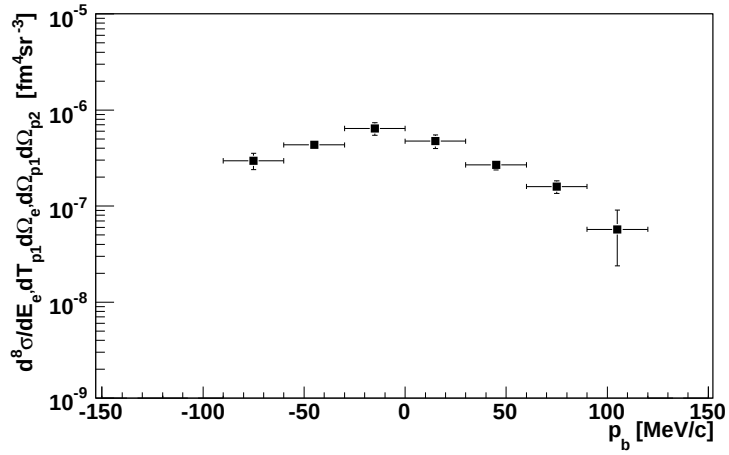

Figure 5.11: The differential cross section of the $^{12}C(e,e'pp)^{10}Be(GS)$ reaction. The bin width is 30 MeV/c.

p_b (central) [MeV/c]	$d^8\sigma/d\Omega$ $[10^{-7}\ fm^4 sr^{-3}]$
-75.0	3.0 ± 0.6
-45.0	4.3 ± 0.5
-15.0	6.4 ± 1.0
15.0	4.7 ± 0.8
45.0	2.7 ± 0.3
75.0	1.6 ± 0.2
105.0	0.6 ± 0.3

Table 5.4: The differential cross section of the $^{12}C(e,e'pp)^{10}Be(GS)$ reaction. The values of missing momentum refer to bin centers. To express the cross section in [fb MeV^{-2}sr^{-3}], the values should be multiplied by $10^{13}/(197.33)^2$.

4.16. In short, this means dividing the measured number of events in the ground state (left histogram in the figure 5.10), by the simulated phase-space (right histogram in the figure 5.10), by the efficiency and by the integrated luminosity. The results are plotted in figure 5.11 and its values are given in table 5.4.

The measured cross section lays within one order of magnitude of the values obtained by the simple calculations [34] shown in the figure 1.6. The shape of the cross section suggests it has the maximum at $p_b \approx 0$. This would be expected for ^{16}O nucleus, as the cross section is dominated by knockout of $^1S_0$ proton pairs [20]. Calculations for ^{12}C that take into account the sophisticated parametrization (SF-B) of the correlations and nucleon-nucleon FSI, would be more suitable for comparison with the experimental data.

5.3 Investigation of ^{12}C(e,e'pπ^-)^{11}C reaction

The triple-coincident $^{12}C(e,e'p\pi^-)^{11}C$ reaction was investigated during two beam-times in the years 2005 and 2006. The experiment was motivated by the preceding investigation of the same reaction [53], which showed evidence of possible narrow Δ states, that were later explained in the schematic model [54].

5.3.1 Kinematics

The choice of kinematics was governed by the ideas explained in section 1.3. This means that proton and pion detectors were positioned at such angles and central momenta, to favor the production of possible bound states and to suppress the quasi-free deltas as schematically shown in the figure 1.9. The precise kinematical settings were determined by the Monte-Carlo simulation program `Simul++` (see appendix C.2). The results of the simulation are shown in the figure 1.10 and the chosen setups are laid out in table 5.5. The spectrometer A was used to detect electrons, the Silicon Detector for protons and the spectrometer C detected negative pions. The electron spectrometer and the Silicon Detector were positioned on the left side with respect to the beam, while spectrometer C was on the right side.

The graphite target of 43.86 mg/cm^2 surface density was used, rotated $\sim$45° clockwise with respect to the beam to minimize the energy loss of the low energy protons detected by the Silicon Detector at backward angles. We used beam currents up to $I_b = 13\ \mu A$, as we were limited by the maximum acceptable counting rate in Silicon Detector's electronics.

Setup no.	E_b [MeV]	I_b [μA]	θ_e [°]	E' [MeV/c]	θ_p [°]	p_p [MeV/c]	θ_π [°]	p_π [MeV/c]	Time [h]
1	855	5	23.0	540.0	-120.0	230.0	65.0	220.0	22
2	855	8	23.0	540.0	-120.0	230.0	70.0	230.0	56
3	855	8	23.0	540.0	-120.0	230.0	70.0	220.0	42
4	855	8	23.0	530.0	-120.0	230.0	70.0	220.0	66
5	855	5	23.0	530.0	-100.0	230.0	50.0	230.0	33
6	855	13	22.0	530.0	-100.0	240.0	47.6	230.0	88

Table 5.5: The kinematic setups for investigation of $^{12}C(e,e'p\pi^-)^{11}C$ reaction. Setup 1-5 were measured during 2005 beam-time, while setup no. 6 was measured in 2006. The angles and momenta refer to detectors' central values. The negative central angles of the Silicon Detector imply that it was positioned at the side of the electron arm.

5.3.2 Beam-time 2005

Experimental setup

During the measurement the Silicon Detector was set-up to accept protons in the kinetic energy range ΔT_p = 21.2 - 35.8 MeV. The distance of the detector from the target was 8 cm, resulting in an angular acceptance of 88 msr.

The energy of the protons detected by the Silicon Detector was reconstructed with analog shaping amplifiers [83] with $T_S = 1.0\ \mu s$ shaping time. This was a limiting factor in the measurement, because the relatively long shaping time caused signal pile-up. This lead to a poor proton energy resolution, already at beam currents such as $I_b = 8\ \mu A$ resulting in a modest energy resolution of the ^{11}C excitation spectrum (see below). More importantly, the statistic obtained at these beam currents was low, with an average rate of 3 triple-coincident events per day for ^{11}C in the ground state.

Silicon Detector trigger signal was obtained from the first silicon layer MSX[3], which resulted in the electron-proton coincidence time resolution of $t_{ASi} = 6.5\ ns$ (FWHM). This was another limiting factor, as it lead to an unfavorable signal-to-background ratio, especially at higher beam currents.

^{11}C excitation spectrum

By applying the cuts on electron-pion, electron-proton and proton-pion coincidence times, the events that correspond to coincident electron, proton and the pion are selected. The applied cuts are: $|t_{AC}| < 2.0$ ns, $|t_{ASi}| < 12.0$ ns and $|t_{CSi}| < 12.0$ ns. The background is subtracted according to procedure described in section 4.1.3. The excitation energy of the recoiling nucleus, in this case ^{11}C, is defined in equation 1.20 and the obtained spectrum is presented in the figure 5.12. The spectrum energy resolution is ΔE_x = 2.7 MeV (FWHM).

5.3.3 Beam-time 2006

Experimental setup

The Silicon Detector energy acceptance for protons was ΔT_p = 24.0 - 39.0 MeV. The distance of the detector from the target was 8 cm and the angular acceptance was 88 msr.

The timing was improved by introduction of the scintillator that was used for triggering (see section 3.2). This resulted in much better electron-proton

[3]The scintillator was not built in at that time.

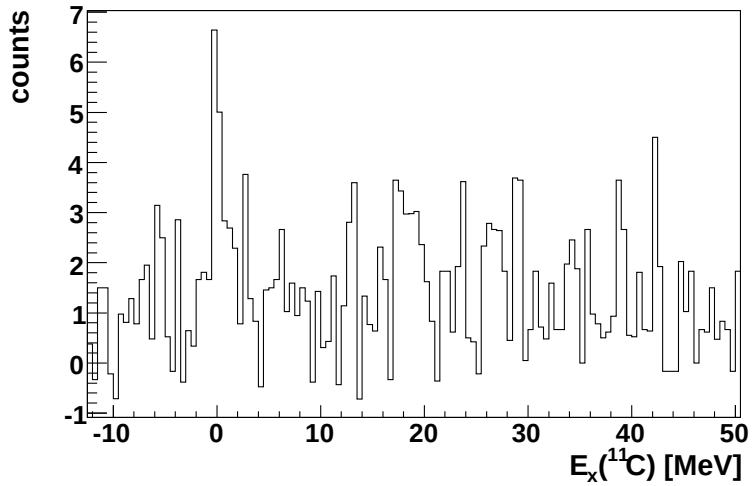

Figure 5.12: Excitation spectrum of ^{11}C measured at $\omega = 334$ MeV and $|\vec{q}\,| = 422$ MeV/c. The energy resolution is $\Delta E_x = 2.7$ MeV (FWHM). The data is obtained from the setups 1-5 (see table 5.5).

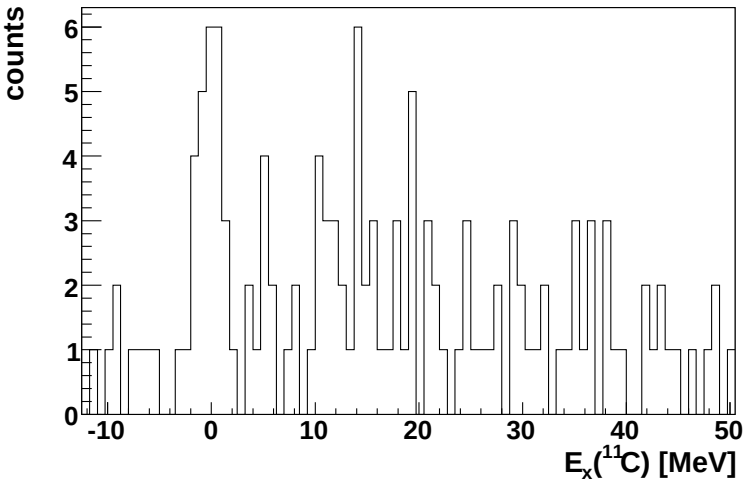

Figure 5.13: Excitation spectrum of ^{11}C measured at $\omega = 338$ MeV and $|\vec{q}\,| = 416$ MeV/c. The energy resolution is $\Delta E_x = 2.9$ MeV (FWHM). The data is obtained from setup 6 (see table 5.5).

and pion-proton coincidence time resolutions $t_{ASi} = 2.0\ ns$ (FWHM) and $t_{CSi} = 2.0\ ns$ (FWHM), respectively.

In order to suppress the pile-up in Silicon Detector's electronics at high counting rates, the proton energy was reconstructed with analog shaping amplifiers [83], but this time with $T_S = 0.25\ \mu s$ shaping time (as opposed to $T_S = 1.0\ \mu s$ in 2005 measurement). The shorter shaping time helped reducing the signal pile-up at high counting rates, therefore measurements with higher beam currents $I_b = 13\ \mu A$ could be performed, keeping comparable energy resolution as in the 2005 measurement. However, relatively low acceptable beam currents[4] were again a limiting factor, because the average triple-coincidence rate of 5 ground state events per day was still too low to gain enough statistics during the available beam-time.

^{11}C excitation spectrum

The excitation energy spectrum of ^{11}C, defined according to equation 1.20 is shown in the figure 5.13. The spectrum was obtained by applying cuts on electron-pion, electron-proton and proton-pion coincidence times. The cuts are: $|t_{AC}| < 2.0$ ns, $|t_{ASi}| < 2.0$ ns and $|t_{CSi}| < 2.0$ ns. The spectrum energy resolution is $\Delta E_x = 2.9$ MeV (FWHM).

5.3.4 Search for narrow Δ

According to the discussion in section 1.3.1 the evidence for possible narrow Δ states could appear in $\hat{\omega}$-spectrum[5], when applying the cut on triple-coincidences and the cut on the ground state of ^{11}C. In short, the triple-coincidence cut should select the events corresponding to an electron, a proton and a pion in the final state, while relatively narrow detector acceptances suppress possible rescattering due to FSI. The cut on the ^{11}C ground state should suppress the energy transfer in the final state.

The cut on the excitation energies $|E_x| < 1.1$ MeV is made, although it is not possible to completely isolate the ^{11}C ground state due to the poor energy resolution. The $\hat{\omega}$-spectrum resulting from all the available data collected in 2005 and 2006 measurements is shown in figure 5.14. Unfortunately, the statistics is insufficient to draw any conclusions about the structure of that spectrum.

[4] The maximum acceptable beam current was $\sim$13 μA, which is low compared to 100 μA that could be delivered by MAMI accelerator.

[5] $\hat{\omega} = W - M_{^{12}C}$, see equation 1.21.

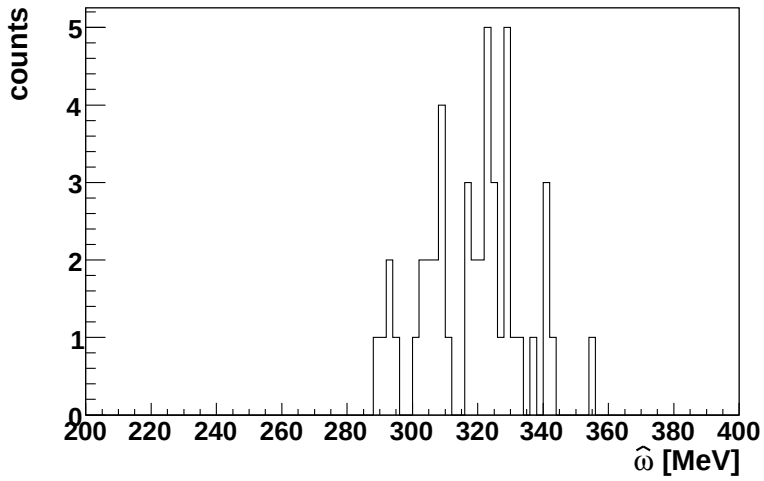

Figure 5.14: $\hat{\omega}$ spectrum with cuts on triple-coincidences and ^{11}C ground state. Data from all 2005 and 2006 runs.

Chapter 6

Conclusion

A new detector system for charged particles, the Silicon Detector, has been developed in the framework of this thesis. It is a telescope consisting of seven layers of silicon diodes and a plastic scintillator. The silicon layers are used for energy deposition measurement and measurement of the scattering angles, while the scintillator provides the trigger. The Silicon Detector has a relatively large solid angle, up to 88 msr, and is therefore of particular interest for measurements where large angular acceptances are required.

Measurements of two triple-coincidence reactions, $^{12}C(e, e'p\pi^-)^{11}C$ and $^{12}C(e, e'pp)^{10}Be$ were carried within the A1-collaboration at MAMI. The Silicon Detector was used for the first time for determination of proton energy and scattering angles in an exclusive measurement in the electron scattering environment.

The investigation of $^{12}C(e, e'p\pi^-)^{11}C$ reaction was carried out in 2005 and 2006, with the intention to obtain evidence of possible narrow Δ states in nuclei. In this triple-coincidence measurement, the Silicon Detector was used for proton detection, while the scattered electron and pion were detected by magnetic spectrometers. The measurements were made with beam currents up to 13 μA at Silicon Detector angles 100° and 120° with respect to the beam. This configuration lead to high counting rates in the Silicon Detector and consequently to pile-up in the analog shaping electronics, that was used at that time. The spectrum of ^{11}C excitation energy was reconstructed, but the achieved resolution of $\Delta E_x > 2$ MeV (FWHM) was insufficient to separate the ground state. Furthermore, the statistics obtained was limited, so the results were alltogether inconclusive.

In the second experiment, the exclusive $^{12}C(e, e'pp)^{10}Be$ reaction was examined. The motive behind the experiment was the investigation of proton-proton short-range correlations in ^{12}C nuclei. This was the first measurement of this reaction in super-parallel kinematics undertaken at MAMI. The Sili-

con Detector was used for proton detection, while the scattered electron and the other proton were detected by the magnetic spectrometers. In this measurement the classic analog shapers for processing of Silicon Detector signals, were substituted by signals samplers (100 MHz flash ADC) and the signals were digitally processed by newly developed algorithms based on trapezoidal shaping. This enabled measurements with higher counting rates, keeping the required energy resolution. The beam currents up to 30 μA were used with the Silicon Detector at 150°. The spectrum of ^{10}Be excitation energy was reconstructed with resolution $\Delta E_x = 1.7$ MeV (FWHM), sufficient to separate the beryllium ground state. This allowed the extraction of the differential cross section for the ground state transition. Preliminary theoretical calculations based on the simple parametrization of correlations yield the cross section within an order of magnitude of the measured values. It would be valuable to compare the experimental results with (not yet existing) calculations involving more complete parametrization of correlations and final state interaction. Such comparison could tell to which extent is the physics description contained in the theoretical models correct, and in that way improve our understanding of nuclear properties.

The Silicon Detector has been used for detection of low energy protons in triple-coincidence experiments. Due to its simple construction and flexible design it could easily be adjusted to be used in other experiments, where its energy and angular resolution is satisfying. These could be for example, experiments where detection of heavier charged particles is required, especially at low momenta which cannot be reached by the magnetic spectrometers.

Appendix A

Silicon Detector - Technical Data

A.1 Detector components

A.1.1 Double-sided strip detector

The double-sided silicon strip detector (BB2) produced by Micron Semiconductor Ltd. [86] is shown in the figure A.1. The wafer is made of n-type silicon and it is 300 μm thick. The detector has twenty four strips in both vertical and horizontal direction. The strips are 1 mm wide with 1000 μm pitch, so the total active area of the detector is 24 mm by 24 mm.

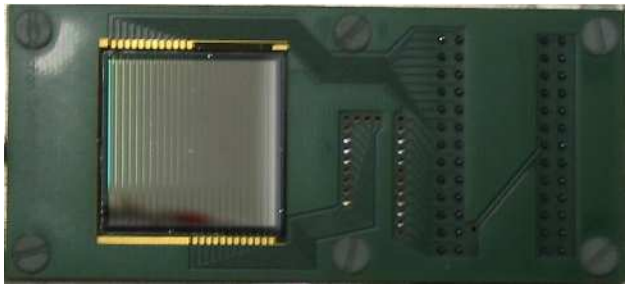

Figure A.1: Double-sided silicon strip detector BB2. Manufactured by Micron Semiconductors Ltd.

Full depletion	30 V
Operating plateau	FD + 30 V
Strip leakage current	50-200 nA
Total leakage current	1-3 μA
Total alpha resolution	55 keV (^{241}Am)

Table A.1: The operational characteristics of an unirradiated BB2 detector, specified by Micron Semiconductor Ltd.

Operational characteristics

The operational characteristics for an unirradiated detector, specified by the manufacturer, are given in table A.1. The guard ring was left floating during detector operation. After 30 days of beam-time the total leakage current increased to 3.8 μA, which is equivalent to 22 $\mu A/cm^3$ when normalized to detector volume.

A.1.2 Single area detectors

The single area detectors (MSX), also produced by Micron Semiconductor Ltd. [86], are ion-implanted structures (fig. A.2). The bulk is made of n-type silicon and the junction is formed with a thin overdoped p^+ layer. The ohmic contact is realized with a thin metal layer on the other side of the detector. The ion-implantation technology offers a good stability and thin entrance and exit windows, in this case 0.5 μm and 0.7 μm respectively[1]. The wafer is 1 mm thick and it is fixed in a PCB plate, with soldering contacts for cables. The active area of 30 mm by 30 mm is surrounded by a guard ring. Very thin coaxial cables (0.7 mm outer diameter) are used in order to ensure close packing of detector layers. The guard ring was left floating during the measurements.

Operational characteristics

The operational characteristics for unirradiated detectors, specified by the manufacturer, are given in the table A.2. The specification of the full depletion voltage varied from 110 V to 160 V for different detectors.

The characteristics of these detectors were extensively tested in the framework of the thesis, which is described in section 3.4. The test results showed that the full depletion voltage for unirradiated detectors is $U_{FD} = 180$

[1]These values are specified by the manufacturer. The window thicknesses measured in the framework of this thesis are slightly larger (1 μm) (see section 3.4.3).

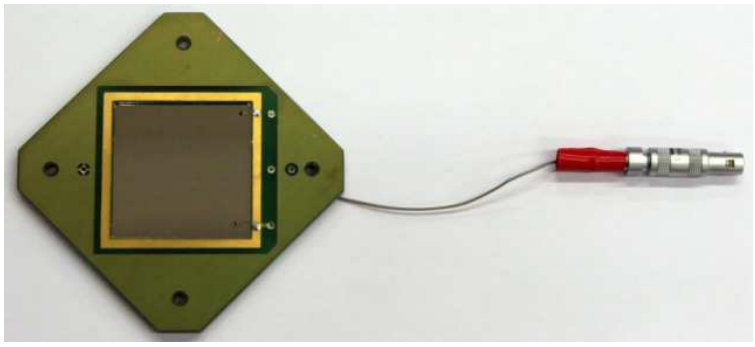

Figure A.2: The single area silicon detector, produced by Micron Semiconductor Ltd., model MSX09.

Full depletion	110-160 V
Leakage current	150 nA
Alpha resolution	27 keV (^{241}Am)

Table A.2: The operational characteristics of a new MSX detector as specified by Micron Semiconductor Ltd.

V, which is more than specified by the manufacturer. Moreover, during the experiments the detectors were operated with $20 - 60$ % overdepletion ($U_{bias} \simeq 220 - 290$ V), which brings the benefits of more efficient charge collection and faster signal rise times[2]. The measured energy resolution was 28 keV (FWHM), which agrees with the value in the table A.2.

After 30 days of beam-time the total leakage current increased to 13.4 μA, which is equivalent to 14.9 $\mu A/cm^3$ when normalized to detector volume. During this time the energy resolution decreased to 120 keV (FWHM).

A.1.3 Veto detector

A silicon strip detector produced by Micron Semiconductor Ltd. [86], model MSI, is used as a veto for passing particles (figure A.3). The detector is totally depleted ion-implanted structure made of n-type silicon of 300 μm thickness. The active area of the detector is 60 mm by 40 mm and it is encircled by a guard ring structure. Although this is a strip detector it was used in a single-area mode, with all the strips signals read out together, as there was no need for angular separation at the back of the telescope.

[2] On the other hand, it increases the leakage current and the risk of detector breakdown.

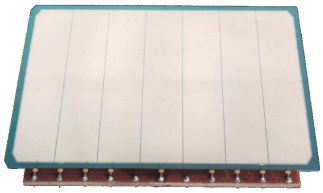

Full depletion	30 V
Operating plateau	FD + 30 V
Total leakage current	1 μA
Total alpha resolution	55 keV (^{241}Am)

Figure A.3: The operational characteristics of the veto detector specified by Micron Semiconductor Ltd.

Operational characteristics

The operational characteristics for an unirradiated detector given by the manufacturer are shown in figure A.3 (right). During the experiments the detector was operated at $U_{bias} \simeq 60$ V. After 30 days of beam-time the total leakage current increased to 4.4 μA, which is equivalent to 6.1 $\mu A/cm^3$ when normalized to detector volume. The guard was floating during the measurements.

A.1.4 Scintillator

A plastic scintillator is used for timing and triggering. The scintillator is 3 mm thick and 24 mm by 24 mm in area. It is connected by a plexiglas fish-tail lightguide to a photomultiplier tube. A special, house-made voltage divider, designed for in-vacuum operation, was used.

A.2 Detector Electronics

A.2.1 Strip detector electronics

Preamplifiers

The preamplifiers for the double-sided strip detector (BB2) were designed by Rutherford Appleton Laboratory and the University of Edinburgh (figure A.4). The preamplifers for each detector channel come in the form of small PCB plates which are plugged into a common motherboard. The motherboard also hosts input and output connectors, powersupply connector and a guard ring connector. It is enclosed in aluminum housing with external cooling fans. There are two preamplifier types, one for positive an the other for negative input (p and n type of detector, respectively), both giving an

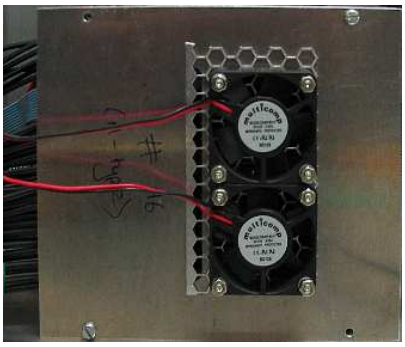

Edinburgh/RAL Preamplifier (RAL108)[1]	
Sensitivity:	10mV/MeV (37nV/e^-) into 100Ω
Noise[2]:	∼2.2keV FWHM (∼255e^- rms.)
Noise slope[2]:	∼72eV/pF FWHM (∼8e^-/pF rms.)
Input capacitance:	0–300pF
Dynamic range:	0–200MeV (±2V into 100Ω)
t_r (10%–90%):	∼5ns (0pF), ∼40ns (100pF)
τ_d (100%–37%):	(50±4)μs
Integral non-linearity:	<0.1%
Output impedance:	100Ω
Power supply[3]:	+13V(14mA), −13V(4.3mA)
Power output:	∼230mW
Circuit:	1.3cm × 3.3cm thick-film hybrid SIL

Figure A.4: RAL108 preamplifier box and its specifications.

inverted output signal[3]. A 26-pin input socket is soldered on the motherboard. 24 pins are dedicated to signal input from the detector strips, one is connected to the guard ring and one is connected to the motherboard and grounded. The signals from the detector are transferred by coaxial cables (50 Ω), which have shown the smallest susceptibility to noise.

Three 34-pin output sockets on the motherboard give non-differential signals, with 100 Ω impedance. The output signals can be obtained either separately for each channel, or as sums of neighboring pairs. The guard ring of the detector can be biased via special connector on the motherboard (in which case the appropriate jumpers should also be switched). A 10-pin socket on the motherboard is provided for preamplifier powersupply (+15V, +15V, -15V), detector bias voltage and test input. An interconnection board, which translates BNC signals to the flat cable compatible with this socket, is available.

Amplifiers

Shaping amplifiers manufactured by Emeteron (model ELA 1006) with 100 ns shaping time constant are used for signal amplification. They are single width NIM units with four channels each. The inputs are single-ended and terminated with 50 Ω. The coarse gain, as well as the signal polarity, can be adjusted by switching appropriate jumpers on the board. The shaping time can also be changed by inserting appropriate modules into the motherboard. Fine gain is adjustable via front panel screw.

[3]The bias voltage is connected only through the p-type preamplifier and is thus negative.

ADC

A charge-integrating ADC (CAEN, model 1885N) is used for signal conversion. This is a single width Fastbus module with 96 input channels. The inputs are quasi-differential with 50 Ω impedance. The complete connection scheme is described in the section 3.6.

A.2.2 Single area detector electronics

The initial electronic setup for energy measurement consisted of charge-sensitive preamplifiers, shaping amplifiers (0.25 or 1.00 μs shaping time) and a peak-sensing ADC. Test measurements showed this to be unsuitable for maintaining good energy resolution at high counting rates. Therefore, a new approach for energy measurement was developed by using the charge-sensitive preamplifiers in conjunction with a flash ADC, which has shown a superior performance. Both setups are described in the following subsections. They can be used simultaneously and independently which is usefull for comparison and debugging, but the initial approach could be abandoned eventually.

Preamplifier

The Mesytec's preamplifier/amplifier box MSI-8 [83] used for the signals of the single area detectors (MSX), contains eight separate preamplifier modules [87]. The modules have charge sensitive preamplifiers accepting both positive and negative charges. They have single-ended inputs (Lemo, 50 Ω) for detector signals and differential outputs (twisted pair, 100 Ω). The output signals have ∼80 ns rise time, decay time constant of 10 μs and range from -1.5 V to +1.5 V. The preamplifier outputs are also internally connected to shaper modules (see A.2.2). The preamplifier supports bias voltages up to 400 V (per channel) which are supplied over a 5 MΩ filter resistor.

Shaping Amplifier

The MSI-8 unit contains eight separate shaping amplifier modules [88], giving positive Gaussian-shaped pulses with amplitude range from 0 V to 8 V. The amplification can be independently adjusted for each channel. The shaping time can also be selected either by switching a jumper on the module (0.25 μs/0.5 μs) or by exchanging the module (1.0 μs) itself. The output sockets are single-ended (Lemo, 50 Ω).

Peak Sensing ADC

A peak sensing ADC (CAEN, model V785N) [89], is used for measuring signal amplitudes. This is a VME module with 12-bit conversion. It has 16 channels accepting positive Gaussian signals with amplitude range from 0 V to 8 V. The input connectors are single-ended (Lemo, 50Ω). This module is selected to match the output signals from the shaping amplifiers described in A.2.2).

Flash ADC

Flash ADC (CAEN, model V1724) [84] is used to sample the preamplifier signals. This 100 MHz digitizer is a VME module, it has eight input channels and 14-bit resolution. The input connectors are single-ended (MCX, 50 Ω) and the input range is from 0 V to 2.25 V. The digitized signals are recorded and used for energy reconstruction, in parallel with the shaping amplifier and the peak-sensing ADC data.

A.2.3 Cables and connectors

Special attention has been paid to cables and signal transmission, especially between the detectors and the preamplifiers. The strip detector has two 26-pin connectors, one for the horizontal strips and the other for the vertical strips. Coaxial cables (RG 174/U, 50 Ω) are used for transmitting the signals, as they have shown the best performance regarding the noise.

Ultra thin coaxial cables of 0.7 mm outer diameter (50 Ω, by Junkosha) are soldered to the MSX detectors. Lemo connectors are mounted on the other end of the cables and the signals are transmitted by standard 50 Ω connections. The total length of the cables from the detector to the preamplifier is not more than 50 cm. The ultra thin cables ensure close packaging of the detector layers. The flash ADC input signals (50 Ω) are fed from preamplifier's differential output (100 Ω), so a special 100 Ω to 50 Ω adapter is used to match the impedances.

The detector is placed inside the vacuum scattering chamber and the electronics is placed outside. Therefore, vacuum feedthroughs are used for signal transmission. A multipin connector (XAVAC, manufactured by Positronic) is used for strip detector signals and BNC feedthroughs for the other detector layers[4].

[4]The feedthroughs are galvanically separated from the chamber walls by a kapton foil to avoid ground loops.

A.2.4 HV supply

Two Mesytec's MHV-4 modules [90] are used for silicon detectors' bias voltage supply. These are NIM modules with 4 independent channels each, giving maximum 400 V and 20 μA per channel. They can be controlled manually or remotely over RS232 serial interface.

A.3 Mechanical Components

A.3.1 Housing

The detector telescope is enclosed in an aluminum housing of 10 mm thickness (fig. 3.9). An opening for particle entrance of 30 mm by 30 mm is left in the front. The scintillator is mounted on top of this opening and the aluminum plate (Al) is fixed on the housing in front of the scintillator. The housing also ensures detector alignment by long alignment screws, as well as mechanical support for the cables.

A.3.2 Supporting construction

The mechanical supporting construction, also made of aluminum, is designed to hold the detector inside the vacuum scattering chamber. The vertical detector position is fixed to match the exact target height. The distance of the detector from the target can be changed (not during beam-time) from 80 mm to 110 mm in 10 mm steps. The rotation of the detector around the target is possible via DC motor (UR 80 CC-40) and a servo potentiometer is used for angle read-out.

Appendix B

Digital signal processing

In the framework of this thesis, the term digital signal processing refers to sampling of the preamplifier (see A.2.2) signals, storing them, and processing them via special algorithms to extract the deposited energy. The sampling is done by a flash analog-to-digital converter (flash ADC). The sampled data is inserted into the Silicon Detector data stream, which is included in data stream of all detectors. This is done by means of the acquisition software `Aqua++` (see C.1). The raw data is processed online and/or offline on a linux-run personal computer.

B.1 Oscillograms

A flash ADC works like a digital oscilloscope. This means it samples the signals with a certain frequency and records the sampled points in the form of an oscillogram. An example of such an oscillogram is shown in the figure B.1. It was recorded by CAEN N1728 flash ADC [79] with 100 MHz sampling frequency, which means that the signal is sampled every 10 ns.

The width of the sampling window is selected according to the application. Usually it is sufficient to record 10 samples before the signal, the rising edge of the signal and the first part of the signal tail. The samples before the signal are needed for base-line correction. The tail samples are needed for proper amplitude reconstruction, thus the number of recorded tail samples should cover the time of the complete charge collection in the detector.

The oscillogram in the figure B.1 is obtained in the measurement of $^{12}C(e, e'p)^{11}B$ reaction, where the Silicon Detector detected protons. The Silicon Detector was positioned at 90° to the beam and the beam current was $I_b = 8\ \mu A$. It is interesting to note what the actual preamplifier signal looks like. The signals corresponding to one particle are the sharp negative

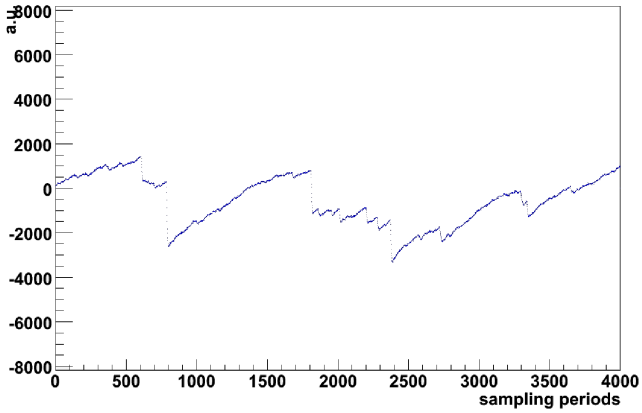

Figure B.1: Digitized preamplifier signal obtained in the electron scattering environment.

amplitudes with the exponential decaying tail. The signal base-line strongly fluctuates and signal pile-up is common due to the high particle flux. These are the main difficulties in the extraction of the real signal amplitude which corresponds to particle's energy deposition.

B.2 Trapezoid algorithm

The preamplifier signals such as the one shown in the figure B.1 are convolution of two time-dependant factors: the rising detector signal and the exponentially falling preamplifier tail. The former is the physical signal and we want to measure its amplitude, as it is proportional to the deposited energy. The latter is a non-physical signal coming from relaxation of the collected charge over the bias resistor. In order to extract the amplitude (energy) we want to perform deconvolution of these two signals.

An established method of amplitude extraction is the trapezoidal shaping [72–74]. It provides the desired deconvolution of the non-physical contribution from the physical one. Practically this means converting original preamplifier signals to trapezoid signals with amplitudes equal to real detector amplitudes not disturbed by the signal decay through preamplifier's bias resistor. Within this work, the method was extended with features such as variable shaping time, base-line correction and pile-up control.

Let $smpl(n)$ be the signal samples obtained with a flash ADC, with n from 1 to N (the total number of samples in an oscillogram). The trapezoid

signal $trapezoid(n)$ is then obtained by the following set of equations [73]:

$$d(n) = smpl(n) - smpl(n-RT) - smpl(n-L) - smpl(n-RT-L) \quad \text{(B.1)}$$
$$p(n) = p(n-1) + d(n) \quad \text{(B.2)}$$
$$r(n) = p(n) + Md(n) \quad \text{(B.3)}$$
$$trapezoid(n) = trapezoid(n-1) + r(n) \quad \text{(B.4)}$$

where RT is the rise-time of the trapezoid, L is its total width and M is the decay constant[1] given by:

$$M = \frac{1}{e^{1/\tau} - 1} \quad \text{(B.5)}$$

τ being the decay constant of the preamplifier signal. It can be determined by monitoring sampled preamplifier signals when the base-line oscillations and the pile-up are absent (e.g. with a weak alpha-source). The reconstructed oscillograms, along with the original signals, are shown in the figure B.2. Full code is given in B.2.4.

B.2.1 Energy reconstruction

The trapezoids have a rising edge and a flat top, as shown in the figure B.2. The magnitude of the flat top (i.e. height of the trapezoid signal) should be proportional to the deposited energy. In real physical measurements the flat top is neither flat nor constant due to base-line oscillations. In order to extract the energy with the most precision, the trapezoid magnitude is calculated by averaging over a number of samples on the flat top. The optimal number of points taken for the average and their position on the flat top are determined empirically. The results are further improved if some type of base-line correction is applied. We average the trapezoid base-line samples just before the trapezoid rising edge and later subtract this value from the value of the averaged flat top magnitude.

B.2.2 Variable shaping time

The rise-times of the detector signals depend on the trajectory of the particles inside the detector. For MSX detectors it was demonstrated that the rise-times are much longer for the particles reaching farther into the detector (see figure 3.13). Practically this means that signal rise-time grows with particle's energy, as long as the particle is absorbed in that layer. In order to collect all the charges created inside a semiconductor detector and properly reconstruct

[1] All the constants are expressed in the number of samples.

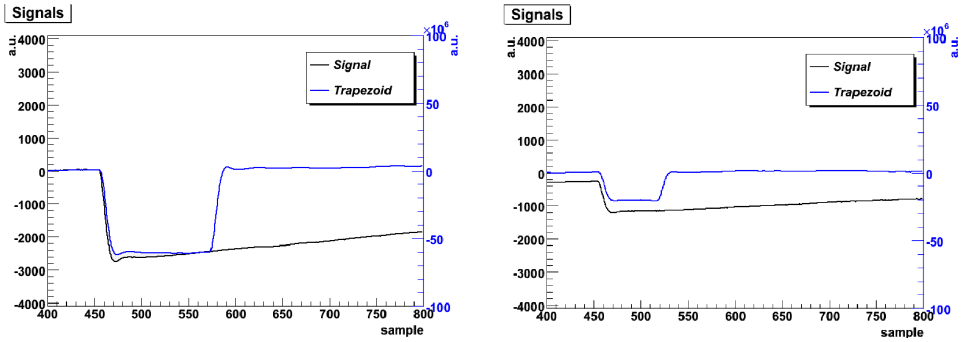

Figure B.2: Digitized preamplifier signal with the reconstructed trapezoids. The left pictire shows the longer trapezoidal shaping applied for larger signals, while the shorter shaping is applied for smaller signals on in the right picture.

the energy, shaping time should be at least as long as the signal rise-time. Therefore longer shaping times are favored for the complete charge collection. On the other hand, longer the shaping time, higher the probability for signal pile-up, therefore shorter shaping times are favored to avoid the pile-up.

A compromise solution is found, by applying different shaping times depending on signal amplitudes. In such method, shorter shaping times are used for signals of lower amplitudes, as these signals are faster. Longer shaping times are used for signals with larger amplitudes, as these are much slower. We set the shaping time proportional to the signal amplitude, varying in the range 400 ns - 1000 ns. This method shows better results concerning energy resolution, than the conventional method with fixed shaping times.

B.2.3 Pile-up control

The pile-up control feature is built into the code in order to further improve the energy resolution. In this case the pile-up refers to pile-up of the trapezoid signal, not the original sampled signal. There are three possibilities:

1. no pile-up reject
2. complete pile-up reject
3. pile-up avoid

In the first case the pile-up is never rejected and all the events are taken into account. In the second case the events with the pile-up are rejected. In the third case if the pile-up is detected, the signal shaping time is shortened just

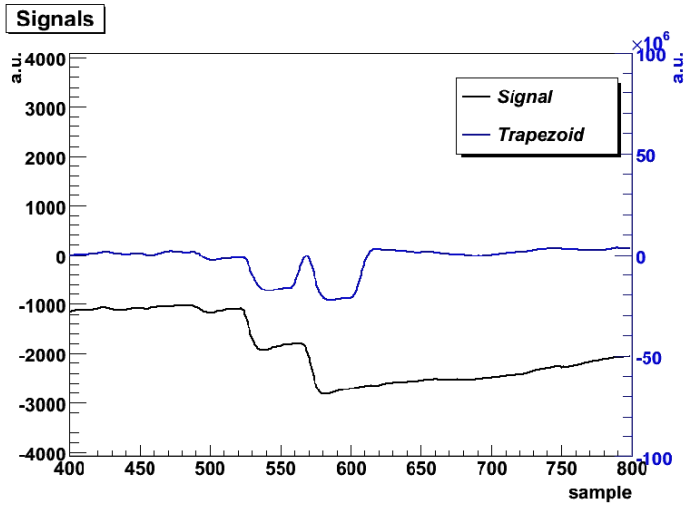

Figure B.3: An example of avoiding the pile-up by shortening signal shaping time.

enough to avoid it (see figure B.3). This possibility also takes into account all events.

B.2.4 C++ code

In this section the C++ code developed in the framework of this thesis is laid out. The code first construct the trapezoid signal (`trapezoid[k][n]`) from the sampled preamplifier signal (`smpl[k][n]`). Then the pile-up control is applied depending on the selected mode. In the end the trapezoid magnitude (`E_ch[k]`) is extracted. The loop is repeated for each event. The code is a part of the Cola++ software package [80].

```
//Oscillogram loop
for (int n=0; n<fADC_samples*2; n++){

  for (int k=0; k<fADC_channels; k++){

    //Fill in the dummy samples for trapezoid calculation
    if (n<fADC_samples) smpl[k][n] = baseline_s[k];

    //Get the real samples
    else smpl[k][n] = *samples_ch[k][n-fADC_samples];
```

```
    // --- Trapezoid calculation ---
    if (n-L[k]-RT<0) d[k] = 0;
    else d[k] = smpl[k][n] - smpl[k][n-RT] \
    - smpl[k][n-L[k]] + smpl[k][n-L[k]-RT];
    pprime[k] += d[k];
    s[k] += pprime[k] + d[k]*M;

    // --- Trapezoid signal ---
    trapezoid[k][n]=s[k];

    // --- Pile-up control or reject ---
    if (pileup_ctrl != 0){
      if (n >= Sstart+Estart+4 && n < Sstart+Estart+Lmax){
        //Set the threshold for each channel
        threshold[k] = (trapezoid[k][n] \
                      - trapezoid[k][n-2]) < pileup_thr;
if (pileup_ctrl == 1){
          //Wait at least Estart samples before next trigger
          if (threshold[k] == \
                  true && n > trigger_mark[k]+Estart+4){
            trigger_mark[k]=n; //Mark the trigger sample
            // --- Pile-up control ---
            if (trigger_mark[k] < Sstart+Estart+Epts[k])
              Epts[k]-=(Sstart+Estart+Epts[k]-trigger_mark[k]);
          }
        }
        if (pileup_ctrl == 2 && k==0){
          //Wait at least Estart samples before next trigger
          if (threshold[0] == \
                  true && n > trigger_mark[0]+Estart+4){
            trigger_mark[0]=n; //Mark the trigger sample
            // --- Pile-up reject ---
            if (trigger_mark[0] < Sstart+Estart+Epts[0])
              return 0;
          }
        }
      }
    }

    // --- Trapezoid base line calculation ---
```

```
    if (n >= Sstart-BL_position-BL_points \
          && n < Sstart-BL_position)
      baseline_t[k] += trapezoid[k][n];

    // --- Trapezoid energy calculation ---
    if (n >= Sstart+Estart && n < Sstart+Estart+Epts[k])
      Etmp[k] += trapezoid[k][n];
    if (n == (Sstart+Lmax)){
      Etmp[k] *= 1.0/Epts[k];
      Etmp[k] -= 1.0*baseline_t[k]/(BL_points);
      E_ch[k] = (Etmp[k]*16383/M/RT/1e4);
    }
  }
}
```

Appendix C

Software

C.1 Data acquisition

A software package `Aqua++` developed by A1-collaboration at MAMI, is used for data acquisition of all detectors [80]. This software runs on linux based VME front-end computers, where one front-end computer is dedicated to each A1-detector[1] and is used to read out its electronics (CAMAC, FASTBUS, VME). The data is sent via fast ethernet to the event-builder running on a Linux based PC. The event-builder merges data from different detectors according to the information from the special event-builder modules that label the events of each detector. The event-builder fills a run database and collects all status information from slow control which is then available for offline analysis. Maximum event-building rate is currently 2.5 kHz, mostly limited by module conversion times and the readout of the relatively slow CAMAC bus. The code is written in `C++`.

When the acquisition program is started, it checks if the data busses of the required detectors are present and reachable. This is performed only once. At the start of each run all the modules are initialized, configured and their memories are erased. The modules are then read out for each event until the acquisition is stopped. This loop is common for all the detectors included in the experiment.

The part of the code concerning the Silicon Detector data acquisition is contained in *AquaSilicon* class. This class defines how different module functions are executed (initialization, configuration, read-out, etc.) and it contains some data operations, that are simple enough to be carried out on the frontends. In particular, the flash ADC module (CAEN V1724) operations are defined in the *AquaV1724* class. The module is configured with the

[1] e.g. spectrometer, Silicon Detector, Neutron Detector, etc.

parameters given in the class header file *AquaV1724.h*. The parameters that ought to be adjusted according to experimental configuration are: number of enabled channels, trigger source, number of samples to be read out and number of pre/post trigger samples.

The flash ADC module (CAEN V1724) is the first module of that type (signal sampler) used within the `Aqua++`. Therefore a simple stand-alone application *FADCtest* for testing purposes was additionally developed. Beside the standard module operations it incorporates firmware check/read/write functions, which are used for firmware update[2].

C.2 Data analysis and simulation

Data analysis, online and offline, is made with `Cola++` software package, developed by A1-collaboration at MAMI. The basic concept of `Cola++` is to use four-vectors reconstructed from raw detector data that are delivered by the data acquisition program `Aqua++` (see C.1). These fourvectors are then used to derive scalars that are filled into histograms. The software also enables defining one- or two-dimensional cuts either with reconstructed quantities or raw data. The analysis is performed on event-by-event basis.

The simulation program `Simul++` is a part of the `Cola++` software package. It is used for simulation of all detectors of the A1-collaboration. The simulation is based on a Monte Carlo event generator. `Simul++` can be used for the simulation of single-arm experiments, as well as for the simulation of double- and triple-coincidence experiments.

C.3 Luminosity calculation

`Lumi++` program, which is also a part of the "Cola" package [80] is used for calculation of the integrated luminosity and dead-time for each run. The live-time for each detector and event type (single, double or triple, see section 2.4) is evaluated from the run-time and real-time information given by the micro busy modules. The luminosity is calculated automatically taking into account the beam current, the target material, the target thickness, the target angle and finally the system live-time. Finally, the integrated luminosity of separate runs is summed by a simple script called LumiSum, to give the total integrated luminosity.

[2]The `Aqua++` code is developed and tested with the module firmware version 1.7_0.8.

Appendix D

Phase-space simulation

The 8-dimensional phase-space volume $< V_{ph}^{8}(x) >$ of the $^{12}C(e,e'pp)^{10}Be(GS)$ reaction is generated using `Simul++`. The following procedure is applied on event-by-event basis:

1. The momenta of two protons p_{p_1} and p_{p_2} are generated within the given detector momentum acceptances, using the Monte-Carlo generator.

2. Scattering angles of all three particles (θ_e, ϕ_e), $(\theta_{p_1}, \phi_{p_1})$ and $(\theta_{p_2}, \phi_{p_3})$ are generated within the given detector angular acceptances, using Monte Carlo generator.

3. For the fixed initial electron energy E_0 and the ground state of ^{10}Be nucleus $E_x = 0$, the energy of the scattered electron E' is calculated following the laws of momentum and energy conservation.

4. Jacobian $\left|\frac{\partial E'}{\partial p_{p_2}}\right|$ is calculated.

5. Simulated variable[1] x is weighted as:

$$< V_{ph}^{8}(x) > \sim \Delta\Omega_e \Delta\Omega_{p_1} \Delta\Omega_{p_2} \Delta p_{p_1} \Delta p_{p_2} \left|\frac{\partial E'}{\partial p_{p_2}}\right| \frac{E_{p_1}}{p_{p_1}} \tag{D.1}$$

   The Jacobian $\left|\frac{\partial E'}{\partial p_{p_2}}\right|$ removes the dependence of the phase-space on momentum of the second proton p_{p_2} and the factor $\frac{E_{p_1}}{p_{p_1}}$ changes the momentum dependence to the energy dependence for the first proton. This yields:

$$< V_{ph}^{8}(x) > \sim \Delta\Omega_e \Delta\Omega_{p_1} \Delta\Omega_{p_2} \Delta E_{p_1} \Delta E' \tag{D.2}$$

[1] In our case $x = p_b$, the momentum of the recoiling nucleus.

6. The simulated histogram is normalized by dividing it by the sum of contents of all bins and multiplying it with the detection volume $\Lambda = \Delta\Omega_e \Delta\Omega_{p_1} \Delta\Omega_{p_2} \Delta E_{p_1} \Delta E$. Finally the simulated phase-space volume is:

$$< V_{ph}^{8}(x) >= \Delta\Omega_e \Delta\Omega_{p_1} \Delta\Omega_{p_2} \Delta E_{p_1} \Delta E' \tag{D.3}$$

Appendix E

Chronology

- 2001 - 2002. Development and testing of a Silicon Detector prototype in the framework of the diploma thesis.
- 2003 - Start of development of the silicon detector system. Design studies, laboratory tests.
- 2004 - Three short test beam-times:
  - 1^{st} test - only the strip detector BB2 and one MSX layer tested.
  - 2^{nd} test - the telescope of BB2 and five single area detectors and veto put into operation,
  - 3^{rd} test - test of various electronic modules and timing performance.
- 2005:
  - Short test beam-time for detector calibration. Thin MSX detector (300 μm) used for triggering.
  - The first measurement of ^{12}C(e,e'pπ^-)^{11}C reaction with the Silicon Detector.
- 2006 - The second measurement of ^{12}C(e,e'pπ^-)^{11}C reaction with the Silicon Detector. The scintillator implemented for triggering.
- 2007 - Short beam-time to test the performance of the first flash ADC.
- 2008 - The measurement of ^{12}C(e,e'pp)^{10}Be reaction. New flash ADC, with oscillogram recording, put into operation.

Bibliography

[1] K.-H. Kaiser *et al.*, Nucl. Inst. and Meth. A **593**, 159 (2008).

[2] A. Jankowiak, Eur. Phys. J. A, s01 **28**, 149 (2006).

[3] K. I. Blomqvist *et al.*, Nucl. Inst. and Meth. A **403**, 263 (1998).

[4] P. K. A. de Witt Huberts, J. Phys. G **16**, 507 (1990).

[5] L. Lapikas, Nucl. Phys. A **553**, 297 (1993).

[6] J. J. Kelly, Adv. Nucl. Phys. **23**, 75 (1996).

[7] O. Benhar *et al.*, Nucl. Phys. A **505**, 267 (1989).

[8] C. Giusti and F. D. Pacati, Nucl. Phys. A **535**, 573 (1991).

[9] C. Giusti *et al.*, Nucl. Phys. A **546**, 607 (1992).

[10] H. Müther and W. H. Dickhoff, Phys. Rev. C **49** (1994).

[11] J. Ryckebusch *et al.*, Phys. Rev. C **61**, 021603 (2000).

[12] H. Müther and A. Polls, Prog. Part. Nucl. Phys. **45**, 243 (2000).

[13] C. Giusti, Eur. Phys. J. A **17**, 419 (2003).

[14] C. Barbieri and W. H. Dickhoff, Prog. Part. Nucl. Phys. **52**, 337 (2004).

[15] A. Rios, A. Polls, and W. H. Dickhoff, Phys. Rev. C **79**, 064308 (2009).

[16] R. B. Wiringa, V. G. J. Stoks, and R. Schiavilla, Phys. Rev. C **51**, 38 (1995).

[17] R. Machleidt *et al.*, Phys. Rep. **149** (1987).

[18] R. Machleidt *et al.*, Phys. Rev. C **53** (1996).

[19] V. G. J. Stoks *et al.*, Phys. Rev. C **49** (1994).

[20] C. Giusti *et al.*, Phys. Rev. C **57**, 1691 (1998).

[21] K. Gottfried, Nucl. Phys. **5**, 557 (1958).

[22] K. Gottfried, Ann. Phys. (N.Y.) **21**, 29 (1963).

[23] K. Gottfried, Ann. Phys. (N.Y.) **21**, 47 (1963).

[24] S. Boffi *et al.*, *Electromagnetic Response of Atomic Nuclei* (Clarendon Press, Oxford, 1996).

[25] C. Giusti and F. D. Pacati, Nucl. Phys. A **641**, 297 (1998).

[26] C. Giusti *et al.*, Phys. Rev. C **60**, 054608 (1999).

[27] P. Wilhelm, J. A. Niskanen, and H. Arenhövel, Nucl. Phys. A **597**, 613 (1996).

[28] C. J. G. Onderwater *et al.*, Phys. Rev. Lett. **78**, 4893 (1997).

[29] D. Middleton, First study of the (e,e'pn) reaction. Ph.D. thesis, The University of Glasgow (2003).

[30] M. Schwamb *et al.*, Eur. Phys. J. A **17**, 7 (2003).

[31] M. Schwamb *et al.*, Eur. Phys. J. A **20**, 233 (2004).

[32] C. Giusti, F. Pacati, and M. Schwamb, arXiv:0801.2304v1 (2008).

[33] K. I. Blomqvist *et al.*, Phys. Lett. B **421**, 71 (1998).

[34] C. Giusti. private communication.

[35] A. Zondervan *et al.*, Nucl. Phys. A **587**, 697 (1995).

[36] L. J. H. M. Kester *et al.*, Phys. Rev. Lett. **74**, 1712 (1995).

[37] M. Kahrau, Untersuchung von Nukleon-Nukleon Korrelationen mit Hilfe der Reaktion $^{16}O(e,e'pp)^{14}C$ in super-parallerer Kinematik. Ph.D. thesis, Universität Mainz (1999).

[38] G. Rosner, Prog. Part. Nucl. Phys. **44**, 99 (2000).

[39] R. Shneor *et al.*, Phys. Rev. Lett. **99**, 072501 (2007).

[40] R. Subedi *et al.*, Science **320**, 1476 (2008).

[41] R. Bertini *et al.*, Phys. Lett. B **90**, 375 (1980).

[42] R. Bertini *et al.*, Phys. Lett. B **136**, 29 (1984).

[43] H. Piekarz *et al.*, Phys. Lett. B **110**, 428 (1982).

[44] R. Sawafta *et al.*, Nucl. Phys. A **585**, 103c (1995).

[45] T. Yamazaki *et al.*, Phys. Rev. Lett. **54**, 102 (1985).

[46] T. Nagae *et al.*, Nucl. Phys. A **631**, 363c (1998).

[47] B. Povh *et al.*, proposal to the SIN/PSI Program Advisory Committee (1985). Unpublished.

[48] W. Brückner *et al.*, Nucl. Phys. A **469**, 617 (1987).

[49] T. Ishikawa *et al.*, Phys. Lett. B **608**, 215 (2005).

[50] M. Kotulla *et al.*, Phys. Rev. Lett. **100**, 192302 (2008).

[51] M. L. Benabderrahmane *et al.*, Phys. Rev. Lett. **102**, 182501 (2009).

[52] R. Nasseripour *et al.*, Phys. Rev. Lett. **99**, 262302 (2007).

[53] P. Bartsch *et al.*, Eur. Phys. J. A **4**, 209 (1999).

[54] T. Walcher, Phys. Rev. C **62**, 064605 (2001).

[55] D. Bosnar and M. Makek, Fizika B **13**, 507 (2004).

[56] R. Böhm, Messung des wirkungsquerschnitts der reaktion d(e,e'p)n für fehlende impulse bis 950 mev/c und trennung der longitudinalen und transversalen reaktionsanteile für fehlende impulse bis 350 mev/c. Ph.D. thesis, Johannes Gutenberg Universität, Mainz (2001).

[57] P. Merle, Entwicklung des programmierbaren koinzidenztriggersystems und messung von A_Y^0 in der reaktion ${}^3\vec{H}e(e,e'n)$. Ph.D. thesis, Johannes Gutenberg Universität, Mainz (2002).

[58] W. R. Leo, *Techniques for Nuclear and Particle Physics Experiments*, 2nd edn. (Springer Verlag, 1994).

[59] Jacoboni *et al.*, Solid State Electron. **20**, 77 (1977).

[60] G. F. Knoll, *Radiation Detection and Measurement*, 3rd edn. (John Wiley and Sons, 1999).

[61] E. Gatti and P. F. Manfredi, Riv. Nuovo Cimento **42** (1986).

[62] V. Augelli and others, (ROSE Collaboration), CERN/LHCC **97-39** (1997).

[63] A. Chilingarov *et al.*, Nucl. Inst. and Meth. A **360**, 432 (1995).

[64] G. Lindstrom, Nucl. Instr. and Meth. A **512**, 30 (2003).

[65] D. Zontar, Study of Radiation Damage in Silicon Detectors for High Luminosity Experiments at LHC. Ph.D. thesis, University of Ljubljana (1998).

[66] G. Lindstrom, M. Moll, and E. Fretwurst, Nucl. Instr. and Meth. A **426**, 1 (1999).

[67] M. Moll, E. Fretwurst, and G. Lindstrom, Nucl. Instr. and Meth. A **426**, 87 (1999).

[68] D. Bechevet *et al.*, Nucl. Instr. and Meth. A **479**, 487 (2002).

[69] R. Wunstorf, Systematische Untersuchungen zur Strahlenresistenz von Silizium-Detektoren für die Verwendung in Hochenergiephysik-Experimenten. Ph.D. thesis, University of Hamburg (1992).

[70] M. Moll, Radiation damage in silicon particle detectors. Ph.D. thesis, University of Hamburg (1999).

[71] S. Sze, *Physics of Semiconductor Devices*, 2nd edn. (John Wiley, New York, 1984).

[72] V. Jordanov and G. Knoll, Nucl. Inst. and Meth. A **345**, 337 (1994).

[73] V. Jordanov *et al.*, Nucl. Inst. and Meth. A **353**, 261 (1994).

[74] M. Lauer, Digital signal processing for segmented hpge detectors preprocessing algorithms and pulse shape analysis. Ph.D. thesis, University of Heidelberg (2004).

[75] H. A. Bethe, Phys. Rev. **89**, 1256 (1953).

[76] Canberra, http://www.canberra.com/pdf/Products/MCA_pdf/C10142-MultiportII-SS.pdf, *Multiport II MCA*.

[77] *NuDat 2.4*. http://www.nndc.bnl.gov/nudat2/.

[78] *ASTAR, Stopping power and range tables for helium ions.* http://physics.nist.gov/PhysRefData/Star/Text/ASTAR.html.

[79] CAEN, http://www.caen.it/nuclear/, *N1728 - 4 channel 100 MHZ FLASH ADC.*

[80] M. O. Distler, H. Merkel, and M. Weis, Proceedings of the 12th IEEE Real Time Congress on Nuclear and Plasma Sciences, Valencia (2001).

[81] *GEANT 3.16 Manual (PHYS320/325).*

[82] P. R. Bevington and D. K. Robinson, *Data Reduction and Error Analysis for the Physical Sciences*, 3rd edn. (McGraw-Hill, 2003).

[83] Mesytec, http://www.mesytec.com/datasheets/MSI-8.pdf, *MSI-8 - 8 channel preamplifier + shaper + timing filter amplifier.*

[84] CAEN, http://www.caen.it/nuclear/, *V1724 - 8 channel 14-bit 100 MS/s digitizer.*

[85] N. I. Ashwood *et al.*, Phys. Rev. C **68**, 017603 (2003).

[86] Micron Semiconductors Ltd. http://www.micronsemiconductor.co.uk.

[87] Mesytec, http://www.mesytec.com/datasheets/MMPR1.pdf, *MMPR1 - Preamplifier module with bias network and differential output.*

[88] Mesytec, http://www.mesytec.com/datasheets/MMSH1.pdf, *MMSH1 - Shaper + timing filter amplifier.*

[89] CAEN, http://www.caen.it/nuclear/, *V785N - Techical information manual.*

[90] Mesytec, http://www.mesytec.com/datasheets/MHV-4.pdf, *MMHV-4 - 4 channel, 400 V detector bias supply.*